Exploring the relative importance of wind for exchange processes around a tidal inlet system: the case of Ameland Inlet

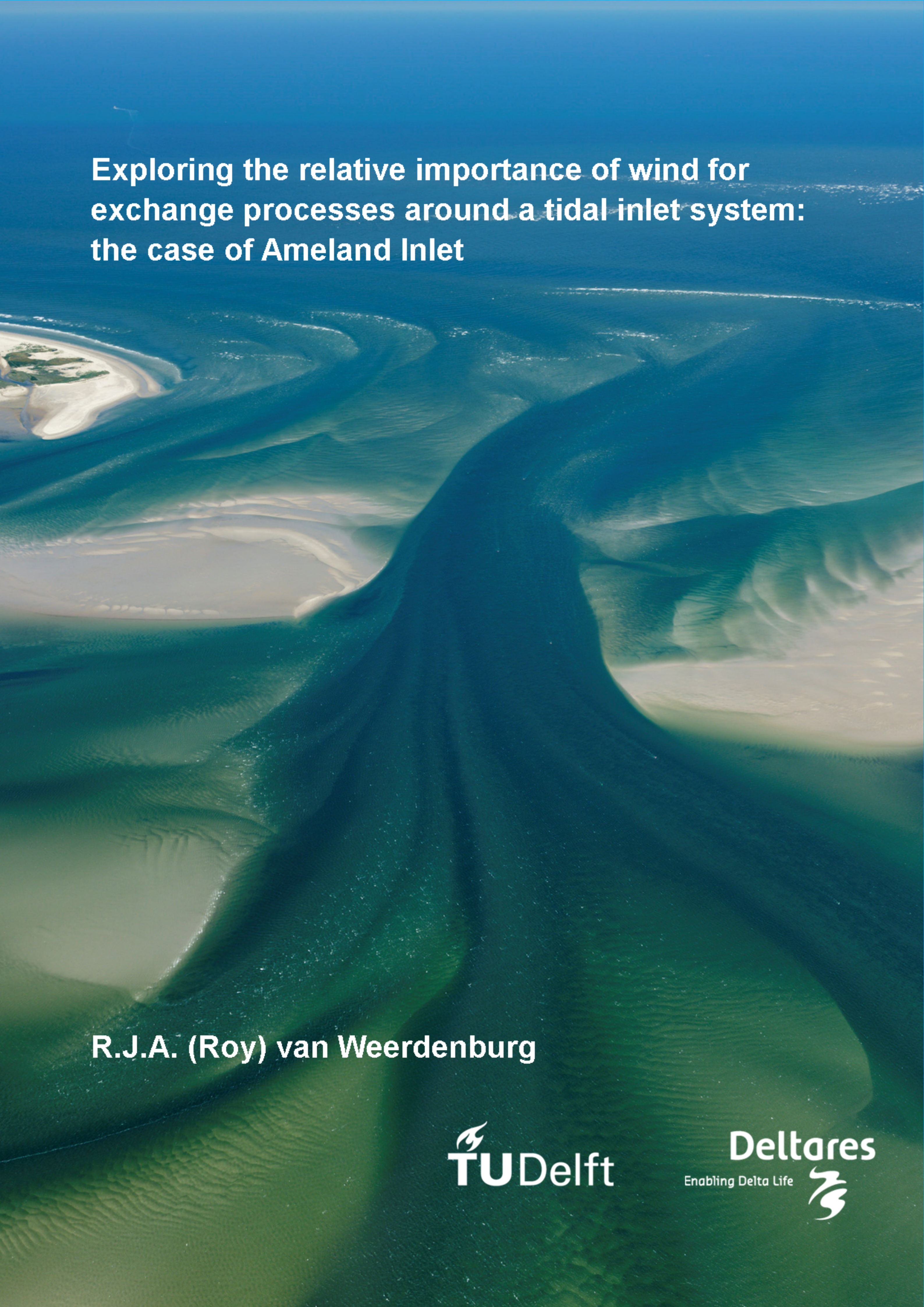

R.J.A. (Roy) van Weerdenburg

TU Delft

Deltares
Enabling Delta Life

Exploring the relative importance of wind for exchange processes around a tidal inlet system: the case of Ameland Inlet

by

R.J.A. (Roy) van Weerdenburg

in partial fulfillment of the requirements for the degree of

Master of Science
in Civil Engineering

at the Delft University of Technology (TU Delft),
to be defended publicly on Monday January 28, 2019 at 15:00 .

Student number:	4292847	
Thesis committee:	Prof. dr. ir. Z.B. Wang,	Delft University of Technology & Deltares
	dr. ir. B.C. van Prooijen,	Delft University of Technology
	ir. P.K. Tonnon,	Deltares
	dr. M.F.S. Tissier,	Delft University of Technology
	ir. S.G. Pearson,	Delft University of Technology & Deltares

Cover: Aerial photo of Ameland Inlet, taken from the Wadden Sea side
© Marco van Middelkoop / Aerophoto-Schiphol

Enabling Delta Life

Abstract

Considering scenarios of sea level rise and coastal management, the current and future sediment budget of the Wadden Sea and adjacent coasts is of interest for both coastal safety and for the maintenance of values of this unique environment. In addition, nourishments on the ebb-tidal deltas of the Wadden Sea are foreseen to compensate for future sediment supply to tidal basins. These developments require us to improve our understanding and predictive capabilities of tidal inlet systems. One of the aims of the research programmes Kustgenese 2.0 and SEAWAD is to investigate the physical mechanisms that determine the pathways of sediment through a tidal inlet system. The current study contributes to this aim by investigating how wind forcing affects the exchange of water and sediment between the North Sea and the Wadden Sea through Ameland Inlet, which is the tidal inlet between the Dutch Wadden islands Terschelling and Ameland.

This study combines field observation with Delft3D numerical modelling results. In fall 2017, field data was collected during an extensive 40 days measurement campaign around Ameland Inlet. Water depths and flow velocity profiles were measured at the ebb-tidal delta, in Ameland Inlet's main channel (i.e. Borndiep), and at the watersheds of Terschelling and Ameland. The field campaign covers both calm conditions and two storms. As part of the Kustgenese 2.0 project, a coupled 2DH Delft3D-SWAN numerical model of Ameland Inlet system is developed by Nederhoff et al. (2019). Results from this model are used to unravel the contribution of different forcing mechanisms (i.e. waves, wind, surge and tides), and to increase the temporal and spatial extent of the results that were obtained by the analysis of field observations.

A traditional harmonic analysis on 40 days records of depth averaged flow velocities did not provide satisfying results regarding tidal asymmetries at the ebb-tidal delta and in the tidal inlet. It appears that meteorological forcing conditions are affecting the hydrodynamics too strongly to consider the harmonic constituents as stationary. The disturbances of the harmonic flow signal are induced by wave- and wind effects. The wind-induced residual current was found as large as the ebb-current during one of the two storms in the field campaign. In general, the residual current at the ebb-tidal delta of Ameland Inlet is northeast directed. In addition, wave-induced residual currents during strong winds from the west-northwest are mostly directed onshore, hence adjusting the direction of the residual discharge per tidal period. High wind shear stresses aligned with the prevailing wind direction (i.e. west-southwest) amplify the residual discharge towards the northeast. The temporal variation in the residual current at the ebb-tidal delta is largely governed by the local wind shear stresses. The combination of a strong residual current with highly energetic wave conditions makes a few events largely contribute to the cumulative sediment transport at the ebb-tidal delta.

Field observations at the watersheds provide evidence for wind-driven residual flows over the watersheds. A quantification of the volumes of water flowing over the watersheds per tidal period, which is based on modelling results, reveals that the inflow per tidal period over the Terschelling watershed can exceed the mean tidal prism through Ameland Inlet. The residual discharge per tidal period over the Ameland watershed can be estimated as 25-30% of the residual discharge over the Terschelling watershed. Only during highly energetic meteorological conditions (i.e. tide-averaged wind speeds exceeding 8 m/s), the hydrodynamics lead to a significant residual sand transport over the watersheds. Residual flows over the watersheds lead to a residual outflow through Ameland Inlet during mild and strong winds from the west-southwest. During calm wind conditions, Ameland Inlet experiences a residual inflow. The magnitude of these residual flows implies that Ameland Inlet is bordered, but certainly not closed by the watersheds. The residual flow structure in Ameland Inlet shows both parts that are flood-dominant and parts that are ebb-dominant.

The extent of shallow parts is found to be of large importance for the development of wind-driven residual currents, which eventually affect the flow conditions in deeper parts of the system. In addition, the orientation of the system in relation to the prevailing wind direction for strong winds are believed to make wind forcing as important as observed around Ameland Inlet.

Preface

This thesis concludes my masters in Hydraulic Engineering at the Faculty of Civil Engineering and Geosciences at the Delft University of Technology. Over the last eight months I have been working on it at Deltares in Delft, in close collaboration with my supervisors at both the Delft University of Technology and at Deltares. I am really grateful for the opportunity to work on this project in this environment, and it ended up being a very enjoyable and gratifying experience. Here, I would like to thank the ones who I owe one.

I would like to thank Professor Wang for chairing the graduation committee and for supervising the project. Your feedback and advice during our meetings helped me to stay critical towards my work and the results. Thank you Bram for initiating this graduation project and for your help and ideas on how to interpret results and subsequently on how to visualise them; I liked your creativity there. I think we eventually found the best way to visualise the dependence of two vectors in one catchy figure. Thank you Stuart for working together on the Ameland case and your close involvement in my part of the project. I hope we will work together again on future projects. Thank you Pieter-Koen, for your help and feedback throughout the project, and above all for providing the opportunity to work on this project at Deltares. Thank you Marion for your guidance in the project and for your feedback on every single version of the report.

Generally, I would like to thank all five members of the graduation committee for your enthusiasm and your curiosity, since it made the project more inspiring to work on.

I would like to thank my temporary colleagues and fellow students at Deltares. I enjoyed working together on our projects and having extensive and sometimes even fruitful chats and discussions near the coffee machine and during lunch. Also, a big thank you to Pieter-Koen, Kees, Reinier and Jebbe for letting me use the Delft3D model you developed. Thank you to Floris for guiding me through a unique bunch of field data and for providing some background on the post-processing. Thank you Tolga for providing critical feedback on earlier versions of the thesis.

I am grateful to Marieke for your support and enthusiasm and to my family, friends and housemates for being around. Enjoy reading!

Roy van Weerdenburg
Delft, January 2019

Contents

Abstract **i**

Preface **ii**

1 Introduction **1**
1.1 Context 1
1.2 Barotropic forcing mechanisms of tidal inlet systems 1
1.2.1 Tidal asymmetries 2
1.2.2 Meteorological forcing 2
1.2.3 Episodic storm events 4
1.3 Research objectives 4
1.4 Thesis outline 5

2 Materials and methods **6**
2.1 Study area. 6
2.2 Field measurements 7
2.3 Post-processing 10
2.4 Data analysis 10
2.4.1 Harmonic analysis 11
2.4.2 Continuous wavelet transforms 12
2.4.3 Wind-generated waves. 12
2.5 Numerical model setup 13

3 Tidal motion **15**
3.1 Harmonic analysis 15
3.2 Flow reversal and asymmetry 18
3.3 Continuous wavelet transforms. 20
3.4 Tidal disturbances in model simulations 22

4 Non-tidal physical processes **25**
4.1 Waves and wind. 25
4.2 Water level set-up 26
4.3 Residual discharge 28
4.3.1 Field observations 29
4.3.2 Responsible forcing mechanisms 31
4.4 Sediment transport model 33

5 Watersheds **38**
5.1 Field observations 38
5.2 Numerical modelling 41
5.2.1 Quantitative analysis. 41
5.2.2 Responsible forcing mechanisms 43
5.2.3 Conveyance at shallow areas 43
5.3 Sediment transport capacity 46

6 System behaviour **50**
6.1 Exchange flow through Ameland Inlet 50
6.1.1 Residual discharge 50
6.1.2 Flow structure in Ameland Inlet 52
6.2 Variations in space and time 54

7 Discussion **58**

8 Concluding remarks **61**

Bibliography **63**

A Tidal analysis at multiple locations **67**

B Sensitivity to model resolution in the inlet **70**

1
Introduction

1.1. Context

Tidal inlets and barrier islands are found along many coasts in the world. In fact, these inlets are openings in the coastline that allow for exchange processes between the open-sea and the tidal basins. Hence, tidal inlets participate dynamically in the coastal tract (Cowell et al., 2003). The intensity of exchange processes and the capacity of tidal basins to store large quantities of sediment make the interaction with tidal basins an essential part regarding the sediment budget of coastal systems. This sediment budget is crucial for flood safety and healthy ecosystems. The mechanisms behind exchange processes with tidal basins have therefore been the topic of many studies (e.g. Dronkers, 1986; Friedrichs and Aubrey, 1988; Li, 2013; Ridderinkhof et al., 2014; Van de Kreeke and Robaczewska, 1993; Wang et al., 1999). The nonlinear interaction between multiple forcing mechanisms (e.g. tides, waves, wind and density differences) and a highly varied bathymetry around tidal inlets make the sediment pathways in tidal inlet systems still hard to predict (e.g. Elias et al., 2006).

The Wadden Sea is a multiple tidal inlet system that spans a distance of nearly 500 km from the northwestern part of the Netherlands to the North Sea coast of Denmark. It is the world's largest coherent system of intertidal flats and was declared a World Heritage site by UNESCO in 2009. The Dutch part of the Wadden Sea extends from the Texel Inlet (the westernmost inlet of the Wadden Sea) to the Ems-Dollar estuary in the east (see Figure 1.1). Recent large-scale morphological changes show a net sediment transport into the Dutch part of the Wadden Sea. This has been, and still is, an important sediment sink of the Dutch coastal system (Wang et al., 2012). Elias et al. (2012) report a net sediment import into the Dutch Wadden Sea of nearly 600 million m^3 in the period from 1935 until 2005. Causes of the sedimentation rate are relative sea-level rise and the effects of large-scale interventions, such as the closure of the Zuiderzee and the Lauwerszee in the early 20^{th} century (Wang et al., 2012).

Most of the sediments necessary for the infilling of the tidal basins in the Dutch Wadden Sea have been supplied by the ebb-tidal deltas (Elias et al., 2012). To compensate for future sediment supply to tidal basins, nourishments are foreseen on the ebb-tidal deltas of the Wadden Sea. The research programmes Kustgenese 2.0 and SEAWAD have the objectives to obtain insight into the sediment demand of the Wadden Sea and into the physical mechanisms that determine the pathways of sediment through a tidal inlet system. Studies are partly based on a large-scale field campaign around Ameland Inlet (see Figure 1.1). The current study aims to contribute to the objectives of Kustgenese 2.0 and SEAWAD by investigating the contribution of wind-driven currents and storm events to residual flows and sediment transport.

1.2. Barotropic forcing mechanisms of tidal inlet systems

A tidal inlet system is generally formed by the combination of tidal basin, inlet and ebb-tidal delta. In multiple-inlet systems the back-barrier basins of multiple inlets are connected. Hayes (1979) discusses a classification of the entrance area of tidal inlet systems based on the relative contribution of tides and waves for the morphological development of the system. This classification, shown in Figure 1.2, is still widely used. In general, the Dutch Wadden Sea coast can be classified as a mixed energy environment (e.g. Elias et al., 2006; Wang et al., 2012). According to Sha (1989), the inlets in the Wadden Sea with small tidal prisms (i.e. those in the east) are more wave-dominated, while inlets with larger tidal prisms (i.e. those in the west) are more tide-dominated. In the coming sections the barotropic forcing mechanisms are discussed, together with relevant findings and examples from other studies.

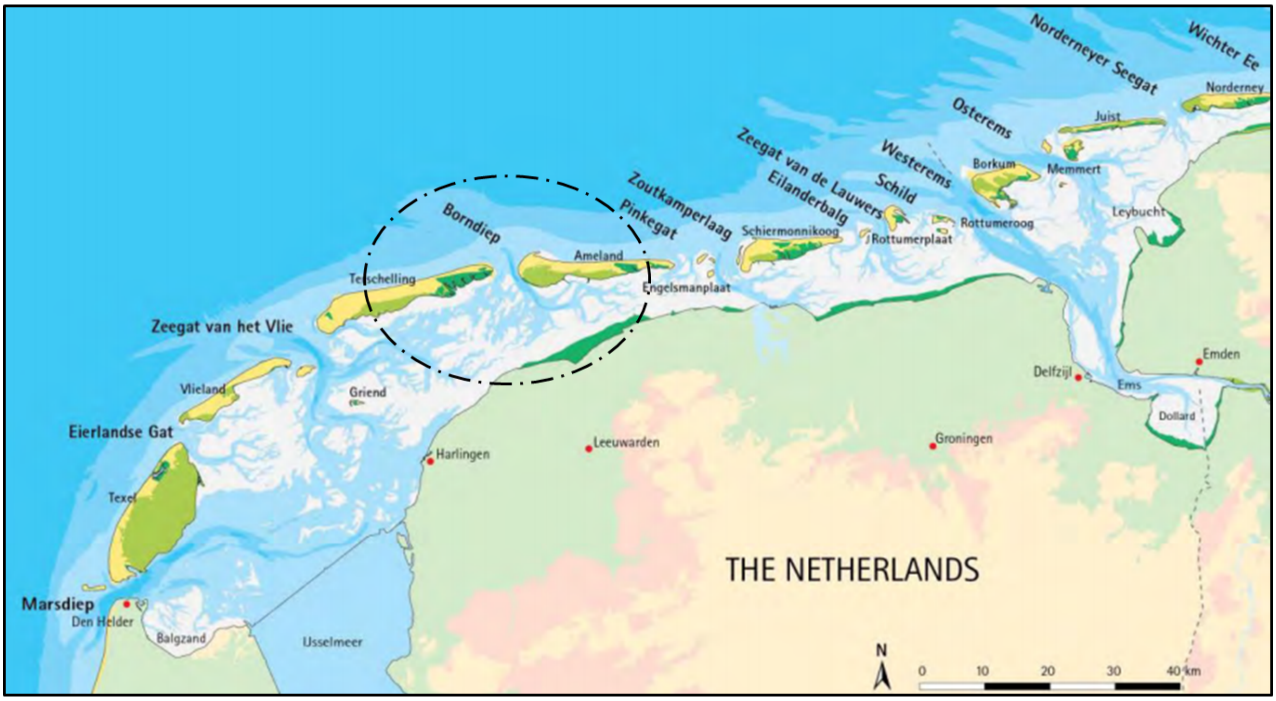

Figure 1.1: Map of the Dutch Wadden Sea and the western part of the German Wadden Sea. The Ems-Dollard estuary marks the beginning of the German Wadden Sea towards the east. The dashed oval indicates Ameland Inlet system. Borndiep is the deepest channel in Ameland Inlet. Intertidal areas are indicated in white. Courtesy: Wadden Sea Secretariat.

1.2.1. Tidal asymmetries

Many studies have investigated the contribution of the pure tidal motion to the residual sediment exchange between different parts of a tidal inlet system (e.g. Chu et al., 2015; Dronkers, 1986; Friedrichs and Aubrey, 1988; Van de Kreeke and Robaczewska, 1993). This is the case if the flow signal is asymmetric, such that the sediment transport capacities of the ebb- and flood flow are different. The tide is considered flood-dominant (ebb-dominant) if it induces a residual sediment transport in the direction of flood (ebb). It was found that the shallow water overtides M_4 and M_6 are most important for the long-term averaged net sediment transport. The development of these overtides is caused by non-linear distortion of the tidal current in response to frictional interactions with the seabed. The M_4 and M_6 constituents are therefore expected to increase in amplitude for an increase in the ratio of the tidal amplitude over the water depth (Chu et al., 2015; Friedrichs and Aubrey, 1988). This ratio varies in space as well as in time, for example with the spring-neap cycle.

In addition, there are more complex mechanisms observed that affect the tidal motion around a tidal inlet system with a highly varied bathymetry. The asymmetry between the M_2 constituents and the overtides, expressed by a phase angle, are found to be larger at neap tides than at spring tides in an inlet in the East Frisian Wadden Sea (Valle-Levinson et al., 2018). At this location, changes in the phase angle developed earlier over the shallow depths than in the channel. Furthermore, storm surge was found to affect the water depth and thus the development of overtides along the west coast of Britain (Jones and Davies, 2008). Seasonal variabilities in the M_2 and M_4 tidal constituents in response to the thermal structure of the North Sea have also been reported (Gräwe et al., 2014). These variations are expected to be of significant importance for sediment transport, also because tidal currents were found more sensitive to nonstationary variations than water levels (Godin, 1983; Guo et al., 2015).

1.2.2. Meteorological forcing

Next to tidal currents, waves are included in the hydrodynamic classification of tidal inlet systems (see Figure 1.2). High bed shear stresses due to near-bed wave orbital velocities in combination with a residual current are of large importance for sediment transport and thus the morphodynamic development of tidal inlet systems. In shallow water, a residual current may be driven by wind shear stresses or by interactions between waves and the seabed, which generates a wave-induced current. For example at Texel Inlet, which is the largest inlet in the Dutch Wadden Sea,

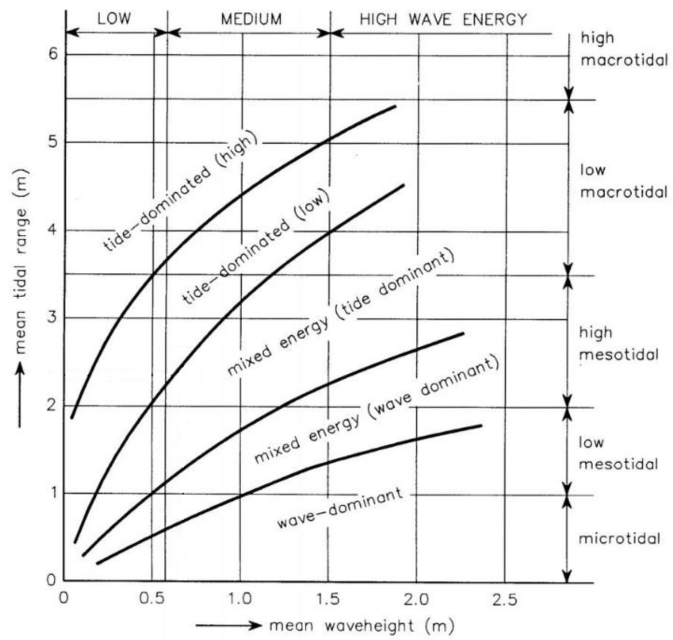

Figure 1.2: Hydrodynamical classification of tidal inlet systems based on the mean tidal range and the mean wave height. Each of the five classes develops its own specific morphologic features. Modified from Hayes (1979).

sediment transport patterns are driven especially by the interaction of tides with non-tidal mechanisms (i.e. winds and waves) (Elias et al., 2006). Landward directed wind- and wave-driven flows enforce the flood-dominance of the tidal signal, and wave effects (e.g. enhanced bed shear stresses and stirring of sediment) increase the flood transport capacities. The wave-driven contribution to exchange processes can vary strongly between different parts of a tidal inlet system. At ebb-tidal deltas the sediment transport can even be primarily driven by waves (e.g. Chen et al., 2015). Large wave-induced currents can also temporarily change the dominant direction of flow asymmetries compared to fair weather conditions (e.g. Bertin et al., 2009).

Various studies on tidal inlet systems have investigated the wind-induced residual flows and the results give different insights in the contribution of wind to a residual transport. Wind forcing can be strong enough to dominate the residual tidal transport, as in the Indian River lagoon on the Atlantic coast of central Florida (Smith, 1990). At the Bay of Guaymas, in the Gulf of California (Mexico), wind forcing induces a complex flow through the tidal inlet: flows over shallow shoals are driven in the same direction as the wind, and a compensatory flow was measured in the deeper channels (Valle-Levinson et al., 2001). In an inlet in the eastern part of the Wadden Sea, the main wind direction was, next to the wind speed, found of high relevance for the exchange flow regime and thus for the long-term sediment dynamics (Purkiani et al., 2016). Duran-Matute et al. (2016) found that the residual volume transport through inlets in the Western Dutch Wadden Sea is much more sensitive to wind from two inherent preferential directions than from any other direction.

In multiple-inlet systems, the exchange processes between back-barrier basins increase the scale and the complexity of the residual flows through the inlet system. In the lower Arcachon Lagoon, in the southwest of France, wind forcing was found to modify the residual circulation in two connected passes (Salles et al., 2015). Depending on the wind direction, the flow in one of the passes was reinforced, while the flow in the other pass weakened simultaneously. Based on the analysis of hydrodynamic data obtained from a ship-based survey in a three-inlet system in central Georgia (USA), Li (2013) states that tide-induced residual currents in this system are small compared to wind-induced flows, and that winds can significantly influence the circulation patterns in a multiple-inlet system. Li (2013) also investigates wind-induced circulations in a multiple-inlet system by using simplified numerical model experiments; it is found that the current over shallow parts tends to follow the wind direction. A return flow is induced in the deeper parts of the system, causing a subtidal circulation flow.

In the Dutch part of the Wadden Sea, a net wind-driven flow over the tidal watersheds is expected to contribute to a residual flow through the inlets. Based on a numerical modelling study, Duran-Matute et al. (2016) found that the variability in the residual flow through inlets strongly depends on the wind forcing. During certain (strong) wind conditions, watersheds can no longer be considered as a closed barrier between two basins. For example during storms from the west, the Ameland basin is expected to experience a significant inflow over the Terschelling watershed, and the watershed can thus no longer be considered as a barrier between the western and eastern Dutch Wadden Sea. Whether the residual flow over the Terschelling watershed contributes significantly to the flow through the next inlet or to the flow over the next watershed is yet to be investigated.

1.2.3. Episodic storm events

Next to generally observed conditions, storms and other episodic events can have an important contribution to the long-term residual sediment transport. This has especially been observed offshore of the tidal inlet, i.e. at the ebb-tidal delta and along adjacent coastlines. Sudden shifts of the Wadden Sea ebb-tidal deltas into the downdrift direction are believed to be induced by storms in the past; especially the combination of high-energy waves and a littoral drift has increased ebb-tidal delta asymmetries suddenly (Sha and De Boer, 1991). The storm induced transport patterns in the tidal basins of the Wadden Sea are less explored (Wang et al., 2012), although it was found based on field observations that transport of fine suspended matter during high-energy events in the German Wadden Sea is mainly controlled by the interference of wind, waves and tidal phase (Bartholomä et al., 2009).

Away from the Wadden Sea, Jaffe et al. (1997) found that infrequent storms could produce one to two orders of magnitude more transport than daily conditions in Cat Island Pass, Louisiana. At this location particularly the bypassing sediment was transported by wind-driven coastal currents. Miner et al. (2009) emphasize the importance of occasional weather events for the morphodynamic development of tidal inlet systems and thus for long-term coastal evolution in general, based on bathymetric surveys conducted in the Mississippi River delta just before and after hurricanes. Miner et al. (2009) also hypothesize that these events may cause the ebb-tidal delta to be an important sediment source for coastal accretion. On Dauphin Island, Alabama, large-scale sediment redistribution and reopening of inlet channels were found consequences of storm surge floods (Nummedal et al., 1980).

1.3. Research objectives

In general, the sediment transport fluxes in a tidal inlet system are the result of interactions between hydrodynamic processes and a complex morphology. To improve our understanding of the sediment exchange between a tidal basin, the ebb-tidal delta and the adjacent coasts, it is essential to analyse the forcing mechanisms of sediment exchange at different locations in the system. The present study aims to quantify the contribution of wind-driven currents and episodic storm events to the exchange processes in a tidal inlet system. The Ameland Inlet system in the Dutch Wadden Sea serves as a case study. The first objective is to unravel the hydrodynamic processes behind sediment exchange around a tidal inlet system, distinguishing calm weather conditions and storm events. The second objective is to quantify the contribution of wind forcing and storm events to residual flows and sediment transport at different morphological parts of the tidal inlet system (e.g. the tidal inlet, the tidal basin, the ebb-tidal delta's channels and shallow parts of the ebb-tidal delta).

The research question of this study is formulated as follows:

> ***What is the contribution of wind forcing and storm events to residual flow and sediment transport in Ameland Inlet system?***

An answer to the research question should consider the relative contribution of different forcing mechanisms and their interactions at different locations in the tidal inlet system. In order to reach the objective of this study and to find answers to the research question, use is made of field data obtained during an extensive field campaign around Ameland Inlet and of numerical modelling simulations using a Delft3D-model (Lesser et al., 2004). The field campaign was carried out during a 40-days period in fall 2017. High-resolution time series of water levels and flow velocities are analysed to investigate the flow characteristics in relation to the measured meteorological forcing (i.e. wind conditions). The field data of this field campaign were, together with field data obtained during earlier campaigns, used to develop, calibrate and validate a 2DH Delft3D-model with online wave coupling by Nederhoff et al. (2019). This numerical model is used in this study to unravel the effect of different physical processes and to extend the results from field observations in space and time.

1.4. Thesis outline

This thesis is structured by topic. Hence, results from field observations and from numerical modelling are discussed side by side in several different chapters. First, Chapter 2 discusses background on the methodology of this study. It includes a general introduction to the study area and a description of the field campaign, background on the post-processing and the analysis of field data, and an introduction to the Delft3D-FLOW & SWAN numerical simulation model. In later chapters one will be referred back to this chapter several times for explanations of the methodology.

Chapter 3 discusses the tidal motion around Ameland Inlet, mainly based on field observations. By using different methods, the characteristics of the tidal signal in time series of the water level and of depth-averaged flow velocities are investigated. In the end of this chapter, the origin of disturbances is discussed based on modelling results. This continuous in Chapter 4, in which field observations are considered in relation to the meteorological conditions (i.e. wind and waves). A minor part of Chapter 4 is based on modelling results, which aims to unravel the contribution of different forcing mechanisms to residual flows.

Chapter 5 discusses the exchange with neighbouring basins by looking into the flow and sediment transport over the watersheds of Terschelling and Ameland. Field observations of the water depth and of flow velocities at the watersheds are discussed, and results are extended in space and in time by using modelling results. In addition, the modelling results are used to investigate the capacity of the hydrodynamics to transport sand particles over the watersheds to the neighbouring tidal basins.

The last chapter with new results is Chapter 6. It investigates the consequences of what was discussed before for the residuals through Ameland Inlet. In addition, the flow structure in Ameland Inlet is explained. The second part of Chapter 6 considers spatial and temporal variations in the governing processes. It is then discussed how representative measurements at observation points during the field campaign are for the entire system and for an extended period of time. This thesis ends with a discussion of the results in Chapter 7 and concluding remarks and recommendations for future research in Chapter 8.

2
Materials and methods

This chapter discusses background on the methodology of this study. It starts with a general introduction into the study area and a detailed description of the measurements that were carried out during the Kustgenese 2.0/SEAWAD field campaign in fall 2017. Subsequently, the post-processing and data analysis methodology are discussed; these explain how the results in the coming chapters follow from the field observations. In the end of this chapter the coupled Delft3D-FLOW & SWAN numerical simulation model is introduced.

2.1. Study area

The Wadden Sea spans a distance of nearly 500 km along the coasts of the Netherlands, Germany and Denmark. 33 tidal inlets connect the Wadden Sea to the North Sea; these inlets are separated by barrier islands. Ameland Inlet is the tidal inlet between the Dutch Wadden islands Terschelling and Ameland. The Ameland Inlet system is formed by the inlet itself, the ebb-tidal delta and the tidal basin behind the barrier islands. The tidal basin of Ameland Inlet system is bounded by the mainland coast and the tidal watersheds behind Terschelling (Terschellinger Wad) and Ameland (Pinke Wad). The two tidal watersheds are located eastward of the centres of Terschelling and Ameland, respectively. Ameland basin has a length of roughly 30 km and covers an area of 270 km^2. Around 60% of Ameland basin consists of intertidal shoals. Due to the underlying Pleistocene morphology, the Wadden Sea is funnel-shaped near Ameland Inlet (Elias, 2017b). This implies it becomes smaller towards the east of Ameland basin, as is shown in Figure 1.1.

Ameland Inlet system is believed to behave most naturally of the inlet systems in the Dutch Wadden Sea, because it is least affected by anthropogenic measures. A map of Ameland Inlet system is shown in Figure 2.2, indicating its bathymetry in June 2017. The largest channel in the inlet is called Borndiep; the depth of this channel exceeds 25 m at the deepest section. Several more shallow channels exist just east of the tip of Terschelling; this shallow area is called Boschplaat. The largest channels in the ebb-tidal delta are called Westgat and Akkepollegat. The channels in the tidal inlet and in the ebb-tidal delta are often characterised by their cyclic behaviour, as is illustrated in Figure 2.1 (Israël and Dunsbergen, 1999). Due to the tidal flow and the littoral drift, the channels migrate generally from west to east. Channels decrease in importance when they approach the tip of Ameland, whereas new channels develop west of the inlet. The observed cycle, based on the analysis of 200 years of historic data (1798-1999), spans between 50

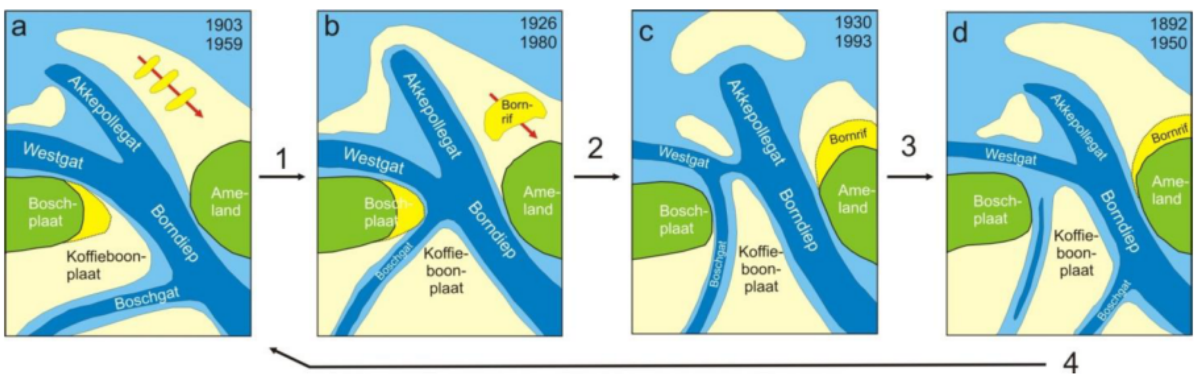

Figure 2.1: Schematic representation of the cyclic morphodynamic behaviour of Ameland Inlet system. One cycle spans approximately 50-60 years, as indicated by the years in the top right corners. Courtesy: Israël and Dunsbergen (1999).

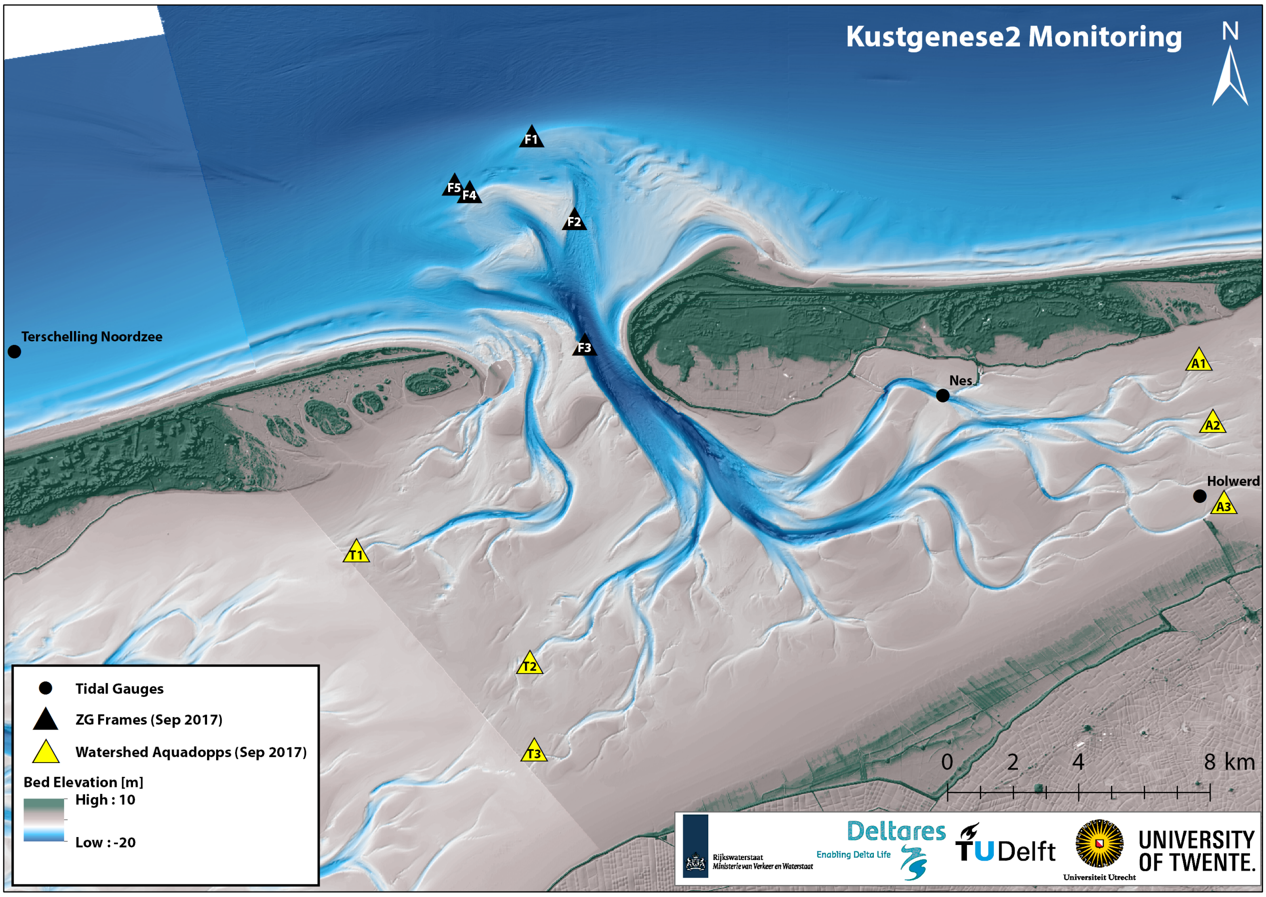

Figure 2.2: Map of Ameland Inlet system indicating the locations where measurement instruments were employed during the Kustgenese 2.0/SEAWAD field campaign in fall 2017. The bed elevation is measured in June 2017 and relative to mean sea level. Courtesy: S.G. Pearson.

and 60 years. More recent work by Elias (2017a), however, indicates that the current morphodynamic development of the Boschplaat does not follow this cyclic concept, possibly because of an increasing depth of the ebb-tidal delta and the resulting increase in wave energy at Boschplaat.

The most recent historical measurements of the tidal prism through Ameland Inlet (which date from 2001) indicate that the ebb-discharge (418 to 454 million m^3) exceeds the flood discharge (407 to 416 million m^3), leading to a net residual outflow. Duran-Matute et al. (2014) estimated the tidal prism through Ameland Inlet at 383 million m^3. The same modelling study concluded that the residual flow is driven by wind and the variability in extreme events. The relatively large residual flows across the watershed behind Terschelling during winds from the west-southwest (Duran-Matute et al., 2016) are expected to contribute to the residual outflow through Ameland Inlet (Elias, 2017b).

2.2. Field measurements

In fall 2017, the extensive 40-days Kustgenese 2.0/SEAWAD field campaign was carried out in and around Ameland Inlet. The measurement period includes calm conditions and two European windstorms, which were named Sebastian (peak at September 13th, 2017) and Xavier (peak at October 5th, 2017).

Measurement frames were deployed at the seabed at four locations at the ebb-tidal delta and at one location in the tidal inlet from August 31st until October 7th. The locations of the frames are shown in Figure 2.2. Frame 1 was located on the northern offshore edge of the ebb-tidal delta, where the mean water depth is 6.8 m. Frame 3 was located in the main channel of the tidal inlet (mean water depth = 16.3 m). Frame 4 and Frame 5 were located on the northwestern part of the ebb-tidal delta, where the mean water depth is respectively 8.7 and 6.8 m. Frame 2 was located in one of the ebb-tidal delta's channels. Unfortunately, Frame 2 was buried with sediment during the field campaign, such that the frame could not easily be retrieved. The data obtained by this frame was not available for analysis at the moment the present study was carried out. Table 2.1 lists the positions of the measurement frames in EPSG:28992 (RD) coordinates.

	Frame 1: ETD-N	Frame 3: Inlet	Frame 4: ETD-NW2	Frame 5: ETD-NW1
EPSG:28992 X-coordinate [m]	167169	168783	165276	164817
EPSG:28992 Y-coordinate [m]	612748	606398	611043	611279

Table 2.1: Locations of the four measurement frames where field data was collected for this study during a 40-days field campaign in fall 2017. The locations are given in the Dutch national coordinate system (Rijksdriehoeksstelsel (RD)), commonly referred to as EPSG:28992.

Every measurement frame was equipped with multiple instruments. The analyses in this study use flow velocities that were measured by upward-looking acoustic Doppler current profilers (ADCPs, type RDI Workhorse Monitor, manufacturer Teledyne Marine) and records of the local water depth that were obtained by the pressure sensors of Aquadopp HR-Profilers (manufacturer Nortek). Flow velocities measured by the Aquadopp HR-Profilers are, like the data obtained by other frame-mounted instruments, used for different purposes than the ones of this study. ADCPs measured three-dimensional flow velocities in bursts of half an hour at a resolution of $f = 1.2$ Hz. These bursts were alternated by half an hour without recordings. Depending on the local water depth, the height of bins varied between 0.25 m and 1.0 m for the different instruments. The pressure sensors of Aquadopp HR-Profilers measured in bursts of half an hour; 29 minutes of continuous measurements at a resolution of $f = 4$ Hz were alternated by a gap of 1 minute.

About halfway the measurement campaign, either at September 18th or at September 19th, each of the measurement frames was lifted to the water surface for maintenance. After this was finished successfully, the frames were relocated at a slightly different location than before maintenance. Due to the highly varying bathymetry the depth at the new location was different. This induces a discontinuity in water level time series. In order to perform a harmonic analysis based on a 40-days record, the water level record is corrected for the discontinuity by assuming that the mean water level over the last two M_2 tidal periods before maintenance is equal to the mean water level over the first two M_2 tidal periods after maintenance. The water level signal is not corrected in other analyses than the harmonic analysis.

In addition to the measurement frames, three Aquadopp HR-Profilers were employed at each of the watersheds of Terschelling and Ameland from September 2nd until October 2nd. Figure 2.2 shows the locations of the instruments on the map. The Aquadopp HR-Profilers at the watersheds measured the pressure and the flow velocities at a resolution of $\Delta t = 1$ min. Flow velocities were measured in three directions by an upward directed acoustic beam in maximum 45 bins of 0.1 m (ENU-coordinates). The blanking distance of these instruments is 0.1 m. Instrument AmID2-T2 did not measure a velocity signal after September 14th, most likely because the instrument was covered with sediment. This instrument still measured the pressure after September 14th, although the weight of sediment on top of the pressure head makes the recorded signal unreliable. Table 2.2 lists the positions of the instruments at the watersheds (EPSG:28992 (RD) coordinates) and the height of the pressure head above the seabed, which is measured just after installation.

	AmID1-T1	AmID2-T2	AmID3-T3	AmID4-A1	AmID5-A2	AmID6-A3
EPSG:28992 X-coordinate [m]	161816	167106	167234	187515	187935	188278
EPSG:28992 Y-coordinate [m]	600066	596668	594001	605915	604025	601540
$d_{\text{pressure head}}$ [m]	0.11	0.05	0.18	0.10	0.10	0.12

Table 2.2: Locations of the Aquadopp HR-Profilers at the watersheds during the field campaign in fall 2017. The locations are given in RD-coordinates (EPSG:28992). $d_{\text{pressure head}}$ is the height of the Aquadopp's pressure head above the seabed, as measured just after installation.

Permanent measurement stations at Nes and at Holwerd record the water level in the Wadden Sea near Ameland Inlet. Station Terschelling Noordzee records the water level just north of Terschelling. The locations of these stations are indicated in Figure 2.2. Wind conditions (wind speed and direction) and air pressure fluctuations were measured at a permanent meteorological station of KNMI (Royal Netherlands Meteorological Institute) at Hoorn, Terschelling. This station is located approximately 15 km west of Ameland Inlet. Both the water level stations and the KNMI station provide an observational record at a resolution of $\Delta t = 10$ min.

Figure 2.3 shows the wind field for 2017 and for the duration of the measurement campaign in wind roses. These wind conditions are measured at KNMI station Hoorn Terschelling. In general, winds around Ameland Inlet are predominantly coming from the west-southwest. Particularly the stronger winds ($w_{sp} > 16$ m/s) were coming from the southwestern quadrant in 2017. Wind speeds exceeding 16 m/s were measured during 0.6% of time in 2017. In addition, Figure 2.4 shows the wind speed and direction for the duration of the measurement campaign. Two periods of strong winds are observed, which were induced by European windstorms Sebastian (peak at September 13th) and Xavier (peak at October 5th). Sebastian induced wind speeds over 20 m/s from the west-southwest and Xavier induced wind speeds up to 20 m/s from the northwest. During the measurement campaign, strong winds were occurring more frequently than year-averaged; stormy winds ($w_{sp} > 16$ m/s) were measured during 2.1% of time. Wind speeds exceeding 20 m/s were only measured during the field campaign for winds from the west-southwest ($245° \leq \phi \leq 265°$). Next to from the west-southwest, strong winds from the south and from the northwest were measured. Winds from the east did not exceed 8 m/s during the measurement campaign.

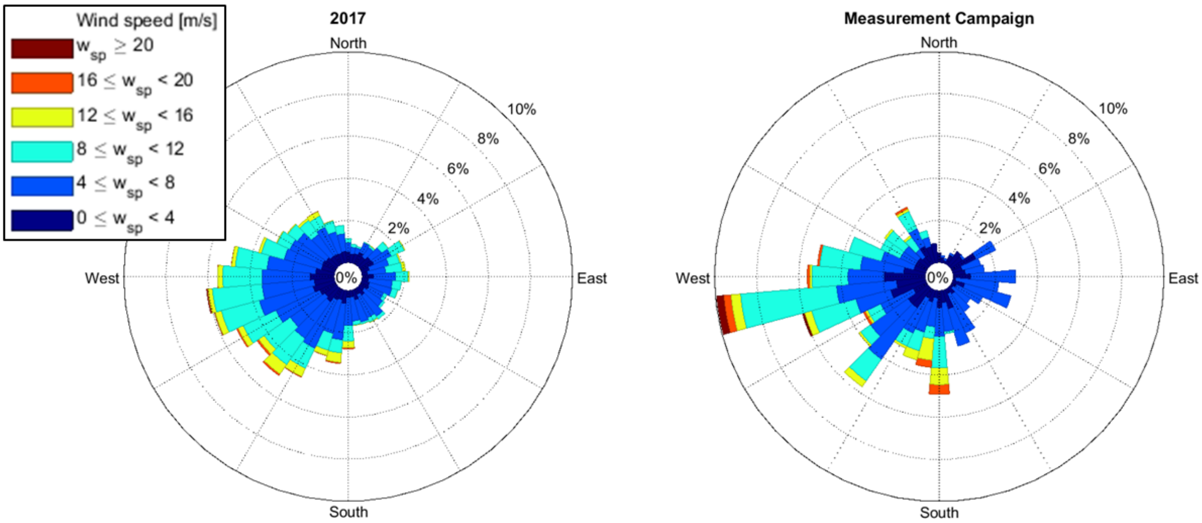

Figure 2.3: Wind roses for 2017 and for the duration of the measurement campaign in fall 2017 (August 31st - October 6th). Winds are measured at KNMI station Hoorn Terschelling, located approximately 15 km west of Ameland Inlet.

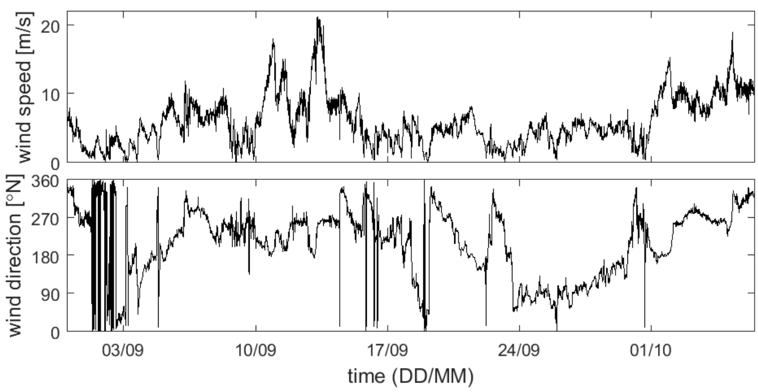

Figure 2.4: Time series of wind speed (top) and wind direction (bottom), as measured during the field campaign at KNMI station Hoorn Terschelling. Peaks at September 13th and at October 5th were induced by the passing of European windstorms Sebastian and Xavier.

2.3. Post-processing

After the recorded pressure signals (p_{measured}) were corrected for atmospheric pressure fluctuations ($p_{\text{atmospheric}}$), the water depth above the pressure sensor was determined according to linear wave theory:

$$p_{\text{measured}} - p_{\text{atmospheric}} = \rho g z + \rho g a \frac{\cosh k(d+z)}{\cosh kd} \cos(\omega t - kx), \tag{2.1}$$

where z < 0 below still-water level (i.e. z = -d at the bottom) and a, k and ω are respectively the amplitude, the wave number and the radian frequency of a linear wave. The first term on the right of Equation 2.1 is the hydrostatic pressure term and the second term is the pressure fluctuation induced by linear waves. In practise, measured waves are irregular and a pressure response function, $K(\omega)$, is applied in the frequency domain after applying a fast Fourier transform (FFT) to the time series (Lee and Wang, 1985):

$$K(\omega) = \frac{\cosh k(d+z)}{\cosh kd} \tag{2.2}$$

An inverse Fourier transform algorithm is subsequently applied to construct time series of the water depth. At the watersheds, the pressure is measured at a resolution of Δt = 1 min. This resolution is too low to capture surface waves, hence time series of the water depth are computed by assuming hydrostatic pressure conditions.

The height above the seabed of a velocity signal measured in the n^{th} bin from the seabed is determined as:

$$z_{\text{u}}(n) = z_{\text{instrument}} + z_{\text{blanking}} + (n - 1/2)\Delta z, \tag{2.3}$$

where $z_{\text{instrument}}$ is the height of the instrument above the seabed, z_{blanking} is the blanking distance of the instrument, and Δz is the height of bins. The ADCPs and Aquadopp profilers also receive a flow velocity signal for cells that are above the water surface. Data in these cells is removed by using the height of the water column above the instrument, which is computed from the internal pressure sensor.

Measured velocities along the different beams of the instrument are first transformed into XYZ velocities by using the instrument's transformation matrix. Then, the heading, pitch and roll (HPR) of instruments are used to transform XYZ velocities into ENU velocities. The heading took account for the compass heading of the instrument, compass deviations caused by nearby metal or batteries influencing the magnetic field around the instrument, and for the deviation between the magnetic north and the true north.

The quality of measured velocity signals is checked based on the correlation between the signals of the different beams and the signal-to-noise ratio (SNR). A low correlation between the signals obtained along different beams indicates an unreliable velocity record and thus low-quality data. Low SNR values means the magnitude of measured velocities is in the same order as the instrument noise, which implies that the recorded signal is much affected by instrument noise. Low-quality data is removed using threshold values for correlation and SNR based on Elgar et al. (2005), resulting in NaN values (Not a Number) in time series. The occasional NaN values are eventually replaced by a velocity value using linear interpolation.

Aliasing of the Doppler signal can lead to spikes in the velocity signal. These spikes are removed using a 3D phase space method, in which an ellipsoid in three-dimensional phase space is constructed based on the velocity signal and the first and second order derivatives (Goring and Nikora, 2002; Mori et al., 2007). Points lying outside the ellipse are designated as spikes and removed from the record.

2.4. Data analysis

The depth-integrated transport in east- and northward direction at a certain time t is defined per unit width as:

$$\mathbf{q}(\mathbf{t}) = \int_d \mathbf{u}(t,z)\,dz, \tag{2.4}$$

where d is the instantaneous water depth and $\mathbf{u}(t,z)$ is the velocity vector as a function of time and of the height above the seabed. The vectors $\mathbf{q}$ and $\mathbf{u}$ have an east-west and a north-south component. Since $\mathbf{q}$ is defined as a discharge per unit width, its unit in Equation 2.4 is m^2/s. In practice, the velocity profile was measured by an ADCP or Aquadopp profiler in bins of height Δz. Eq. 2.4 then discretises to:

$$\mathbf{q}(\mathbf{t}) = \sum_{i=1}^{n} \mathbf{u_i}(t, z_i) * \Delta z, \tag{2.5}$$

where n is the number of bins that are completely below the water surface. If the acoustic beam of the ADCP did not reach the water level at a certain time step, the near-surface velocities are assumed to be equal to the mean of the velocities in the upper five bins with available data. The ADCP instruments mounted on the measurement frames were located 2.3 m above the seabed and the blanking distance is 0.5 m. The first bin from the bottom thus has its centre 2.8 m + 1/2 Δz above the seabed and no velocity data points are available below the first bin. In determining the depth-integrated transport, the near-bottom velocities are estimated as the mean of zero and the velocity value in the first bin from the bottom. At the two watersheds, the water depth varies roughly between 0 at low water and 2 m at high water. Because of the relatively small water depth in relation to the number and the height of bins, the near-surface velocities at the watersheds are assumed equal to the velocity that was measured in the highest bin that is completely below the water surface.

2.4.1. Harmonic analysis

A harmonic tidal signal will be derived from the data by a harmonic analysis, which is implemented in the UTide method (introduced by Codiga (2011)). The iteratively reweighted least squares (IRLS) minimization method is preferred above the ordinary least squares (OLS) minimization method to limit the influence of high-amplitude outliers on the overall solution of the harmonic analysis. Cauchy's weighting function is applied to the normalised residual r in the IRLS algorithm:

$$\omega_{\text{cauchy}} = \frac{1}{1+r^2}, \tag{2.6}$$

where ω_{cauchy} is the weighting factor appointed to a measured value in the IRLS minimization method and r is the normalised residual (i.e. the normalised difference between the measured value and the harmonic signal of the previous iteration). Per iteration the weighting factors are determined based on the normalised residual, which yields the vector ω. The model $\mathbf{h} = \mathbf{Ax}$ is then solved by:

$$\mathbf{x} = (\mathbf{A^T}\omega\mathbf{A})^{-1}\mathbf{A^T}\omega\mathbf{h}, \tag{2.7}$$

where $\mathbf{h}$ lists the observed values, matrix $\mathbf{A}$ includes the known harmonic characteristics (i.e. frequencies) of the tidal constituents that are included in the analysis, and $\mathbf{x}$ defines the harmonic fit (i.e. amplitude and phase angle) to the observed values during a certain iteration. In the OLS minimization method measured values all have the same weight and Equation 2.7 simplifies to:

$$\mathbf{x} = (\mathbf{A^T}\mathbf{A})^{-1}\mathbf{A^T}\mathbf{h} \tag{2.8}$$

The computation of the 95% confidence intervals uses Monte Carlo uncertainty propagation and is based on the assumption that the errors follow a coloured residual spectra. A more in-depth description of the harmonic analysis can be found in e.g. Leffler and Jay (2008) and Codiga (2011).

In this study, a tidal period is defined as the period of the dominant M_2 harmonic (T_{M_2} = 12.42 hrs). A tidal period starts at slack tide going from ebb to flood (i.e. upward zero crossing of the harmonic transport signal). The directions of ebb tide and flood tide follow from harmonic analysis as the current ellipse orientation angle of the M_2 harmonic. At the ebb-tidal delta of Ameland Inlet flood tide is directed towards the south-east. The residual discharge per tidal period is then defined per unit width as:

$$\mathbf{q_T} = \int_T \int_d \mathbf{u}(t,z)\, dz\, dt, \tag{2.9}$$

where T is the harmonic M_2 tidal period. The vector $\mathbf{q_T}$ has both an east-west and a north-south component. Since the velocity profile is measured in bins of height Δz at every time step Δt, Equation 2.9 is discretised to:

$$\mathbf{q_T} = \sum_{j=1}^{m} \sum_{i=1}^{n} \mathbf{u_i}(t_j, z_i) * \Delta z * \Delta t, \tag{2.10}$$

where n is the number of bins below the water level and m is the number of time steps in tidal period T.

At the watersheds, no velocity signal was measured during some low water conditions, either because the observation point is dry during low water or because the water depth did not exceed the blanking distance of the instruments. M_2 tidal periods are thus separated by a gap in the record. This separation is used in the analysis of the data, which implies that at the watersheds a tidal period is defined as an M_2 period that starts at low water.

2.4.2. Continuous wavelet transforms

Wavelets are used in this study to investigate the degree of nonstationarity in time series of water levels and depth-averaged flow velocities. Both general introductions to wavelet analysis (e.g. Kaiser, 2011) and applications of continuous wavelet transforms (CWT) for the analysis of tides (e.g. Flinchem and Jay, 2000; Guo et al., 2015; Jay and Flinchem, 1997) are available in literature. Here, the basic principles of the CWT-analysis are discussed.

The CWT-analysis transforms one-dimensional input data into a two-dimensional output in time and frequency, which allows one to determine both the dominant frequency mode and the variations of this mode over time (Guo et al., 2015; Jay and Flinchem, 1997). The CWT-analysis starts with the selection of a prototype function which has finite variance, is localised in time near the origin, and has zero mean. The wavelet analysis procedure is to adapt the frequency and the amplitude of the prototype function, in order to represent the original signal in terms of multiple wavelets. The energy of a wavelet with a certain frequency in the composed signal indicates the occurrence of oscillations with that frequency in the original signal.

In this study the analytical Morlet wavelet is applied as prototype function:

$$\psi(\gamma) = \pi^{-\frac{1}{4}} e^{i\omega_o\gamma} e^{\frac{1}{2}\gamma^2}, \tag{2.11}$$

where ω_o is the dimensionless frequency and γ is the dimensionless time. The Morlet wavelet is presented graphically in Figure 2.5.

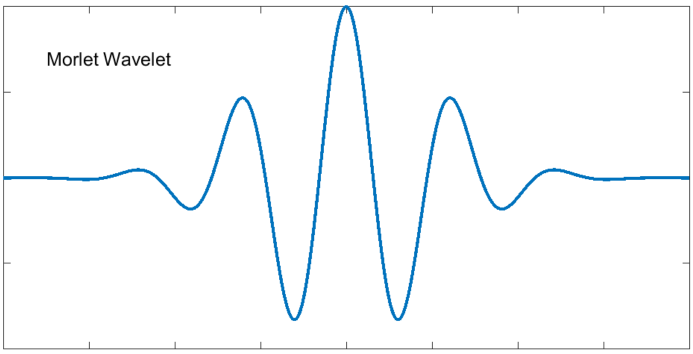

Figure 2.5: Graphical presentation of the Morlet wavelet, which is used as prototype function for continuous wavelet transforms.

2.4.3. Wind-generated waves

The wave characteristics are derived from the short-term fluctuations of the water level and the horizontal velocities. The significant wave height over a certain period is defined as:

$$H_{m_0} = 4\sqrt{m_0}, \tag{2.12}$$

where m_0 (in m^2) is the variance of the measured water surface elevation after the linear trend per burst has been subtracted. The energy-weighted mean wave direction over a certain time ($\overline{\theta}$) is defined as the orientation of the dominant principal axis of the ($\hat{u}$, $\hat{v}$) co-variance matrix:

$$\overline{\theta} = \frac{1}{2}\tan^{-1}\left(\frac{2\,\langle \hat{u}\hat{v}\rangle}{|\langle \hat{u}^2\rangle - \langle \hat{v}^2\rangle|}\right), \tag{2.13}$$

where $\hat{u}$ and $\hat{v}$ are measured eastward and northward velocities, band-passed between 0.05 and 0.25 Hz (Henderson et al., 2006; Herbers et al., 1999). The direction of waves is defined as the direction where waves are coming from, relative to the north (°N).

2.5. Numerical model setup

As part of the Kustgenese 2.0 research programme, a depth-averaged hydrodynamic-wave model has been developed, calibrated and validated by Nederhoff et al. (2019). The coupled Delft3D-FLOW (Lesser et al., 2004) & SWAN (Booij et al., 1999) model is intended to simulate hydrodynamics and sediment transport at the lower shoreface near the islands Terschelling and Ameland and around Ameland Inlet. One is referred to Nederhoff et al. (2019) for a detailed discussion of the setup, calibration and validation of the model. Here, the model is introduced with respect to its application in this study, which is to unravel the observed hydrodynamics during the field campaign in fall 2017 and, in addition, to extend the analyses in space and time (i.e to the duration of one full year (2017)).

The model domain covers the central part of the Dutch Wadden Sea, the tidal inlets of Terschelling, Ameland and Schiermonnikoog, and the lower shoreface north of Terschelling and Ameland (see Figure 2.6). The SWAN domain is larger than the Delft3D-FLOW domain to prevent boundary issues. The SWAN grid is a factor 2 coarser than the Delft3D-FLOW grid to reduce the computational demand. A second, nested, SWAN model covers Ameland Inlet at the same resolution as the Delft3D-FLOW grid. The model applies a bathymetry that is mainly based on the Vaklodingen dataset of 2017, supplemented with data from earlier years for parts that were not surveyed in 2017.

The Delft3D-FLOW model is forced by a zero-gradient Neumann boundary in the surfzone and at the watersheds behind Vlieland and Schiermonnikoog, and by water level boundary conditions at deeper water boundaries. The water level boundary conditions are derived from the DSCMv6ZUNOv4 tide-surge model for the northwest European shelf (Zijl et al., 2013), which includes tide-generating forces and ERA-interim meteorological forcing. The boundary conditions contain 56 tidal constituents and a non-tidal residual (NTR). The latter is generally considered as surge. The SWAN wave model is forced at the offshore boundaries by measured wave spectra at Schiermonnikoog-Noord (RDx = 206610 m, RDy = 617304 m, depth = 22 m) and Eierlandse Gat (RDx = 106601 m, RDy = 616004 m, depth = 19 m). The locations of these wave buoys are indicated in Figure 2.6.

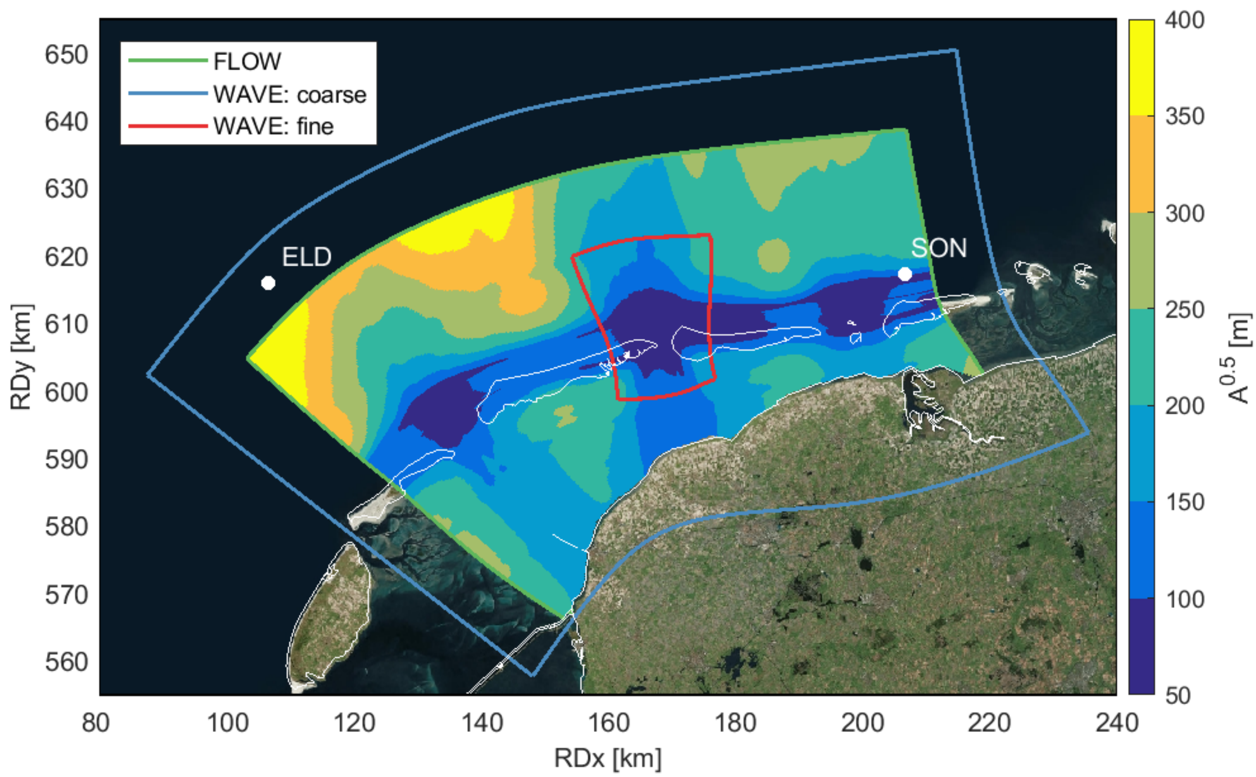

Figure 2.6: Numerical model domains and the resolution of the Delft3D-FLOW grid, which is indicated as the square root of the area of the grid cells. The SWAN grid (blue line) has a larger spatial extent to avoid boundary issues within the DELFT3D-FLOW domain. Ameland Inlet is covered by a second, nested, SWAN domain (red line) with the same resolution as the Delft3D-FLOW domain. White dots indicate the locations of wave buoys at Schiermonnikoog-Noord (SON) and Eierlandse Gat (ELD). Coordinates are given in the Dutch national coordinate system (Rijksdriehoeksstelsel (RD)), commonly referred to as EPSG:28992. Modified from Nederhoff et al. (2019).

The meteorological forcing is based on the HIRLAM model, which is a high resolution local atmospheric reanalysis model run by KNMI (Royal Netherlands Meteorological Institute). The HIRLAM model has a resolution of 3 to 16 km and output is available every hour. This output data is used as meteorological forcing (i.e. wind conditions and atmospheric pressure fluctuations) for the coupled Delft3D-FLOW & SWAN model. The main advantage of using a meteorological reanalysis model in comparison to field observations is the inclusion of the spatial variability in the atmospheric pressure and the wind field, which yields a better fit to field observations of flows (Nederhoff et al., 2019). The wind speed contributes to a shear stress in the momentum equations according to the formulation of Vatvani et al. (2012), using a drag coefficient that approximates the parametrization following Makin (2005).

The bed roughness is determined based on the Van Rijn roughness predictor (Van Rijn, 2007a), using coefficient of 0.5, 0.5 and 0 for the effects of ripples, mega-ripples and dunes, respectively. During average flow conditions, this yields a spatially varying Manning coefficient of 0.014 $s/m^{1/3}$ in the basin to 0.028 $s/m^{1/3}$ offshore and in the tidal inlets (Nederhoff et al., 2019). Sediment transport computations are based on the Van Rijn transport formulations for bed-load transport and suspended transport (Van Rijn, 2007ab). The sediment composition is simplified to one uniform sediment fraction: D = 200 μm. This particle size is based on the median grain size (D_{50}) in sediment samples that were taken in the inlet and at the ebb-tidal delta.

Hydrodynamic conditions and sediment transport around Ameland Inlet are simulated in this study for a full year (2017), using four different combinations of forcing mechanisms. These combinations are used to unravel the contribution of different mechanisms to residual flows and sediment transport. In each of the four simulations different processes are enabled, either in the model or at the boundary conditions:

- **A:** Tide + Surge + Wind + Waves
- **B:** Tide + Surge + Wind
- **C:** Tide + Surge
- **D:** Tide

Wave-driven processes are excluded by disabling the coupling with SWAN. Wind-induced shear-stresses in the Delft3D-FLOW domain are excluded by turning off the wind module. The exclusion of surge in simulation **D** changes the water level boundary conditions by removing the non-tidal residual in the output of the DSCMv6ZUNOv4 model. The water level boundary conditions then only contain the harmonic time series.

3
Tidal motion
Nonstationarity during a 40-days field campaign

This chapter aims to describe the tidal motion near Ameland Inlet as observed during the 40-days field campaign. Firstly, the characteristics of both the vertical tide (i.e. water levels) and the horizontal tide (i.e. depth-averaged flow velocities) are investigated using harmonic analysis (HA), in which the tidal harmonics are considered stationary. Secondly, the tidal motion is discussed based on the relative duration of ebb and flood and the peak flow velocities in ebb- and flood-direction. Subsequently, in Section 3.3, the time series of water levels and depth-averaged flow velocities are analysed using continuous wavelet transforms (CWT). The origin of tidal disturbances is qualitatively investigated using model simulations in Section 3.4.

The tidal motion is considered at the three frame locations at the ebb-tidal delta and at the frame location in the tidal inlet (see Figure 2.2). Qualitatively, the results for the three locations at the ebb-tidal delta are similar. Some of the results are therefore presented for only one instead of three observation points at the ebb-tidal delta (i.e. Frame 1: ETD-N). Tables and figures regarding the other two locations at the ebb-tidal delta (i.e. Frame 4: ETD-NW2 and Frame 5: ETD-NW1) are included in Appendix A.

The tidal motion near Ameland Inlet is induced by the combined effect of a northward propagating tidal wave from the North Sea and an eastward propagating tidal wave that rotates anti-clockwise around an amphidromic point in the north (Elias, 2017b). As a first introduction into the harmonic signal, Figure 3.1 shows time series of the water depth and depth-averaged flow velocities in east- and northward direction as measured at Frame 1: ETD-N and at Frame 3: Inlet. The coming sections will elaborate on these signals.

3.1. Harmonic analysis

Based on a record at station Terschelling Noordzee, the twelve tidal constituents that have most energy in the water level variation near Ameland Inlet were found to be M_2, S_2, N_2, O_1, M_4, K_1, L_2, K_2, MU_2, MS_4, SSA and M_6 (Elias, 2017b). Here, the tidal motion is investigated based on a record of 40 days. Therefore, not all twelve constituents can be resolved: The record is too short to resolve the SSA constituent (T_{SSA} = 0.5 years) and to separate the L_2 constituent from the S_2 constituent (Rayleigh criterion, Δf = 0.005 day^{-1}). Hence, SSA and L_2 are left out of the analysis and only the remaining ten tidal constituents are investigated in the harmonic analysis in this section.

First, a harmonic analysis is applied to the time series of water levels using the IRLS minimization method (see Section 2.4). Table 3.1 lists the characteristics of the ten tidal constituents in the harmonic signal at Frames 1 and 3. The most interesting observations are the following:

- 80% and 62% of the variance in the time series of water levels is caused by these ten tidal constituents at respectively Frames 1 and 3. This suggests that the non-tidal water level variations have a larger contribution in the water level variance at the observation point in the tidal inlet than at the ebb-tidal delta.
- With an amplitude of 0.85 m, the M_2 component is clearly the most dominant contributor to the harmonic water level signal (E > 80%). At both locations the ratio between the diurnal and the semi-diurnal tidal components, which is often identified by (K_1 + O_1) / (M_2 + S_2), is much smaller than 0.25. The tide is therefore classified as semi-diurnal.
- According to this analysis, the S_2 component causes a significant spring-neap variation with an amplitude of around 0.4 m. This cycle has a period of 14.8 days (Δf = 0.068 days^{-1}). The S_2 component is appointed a larger

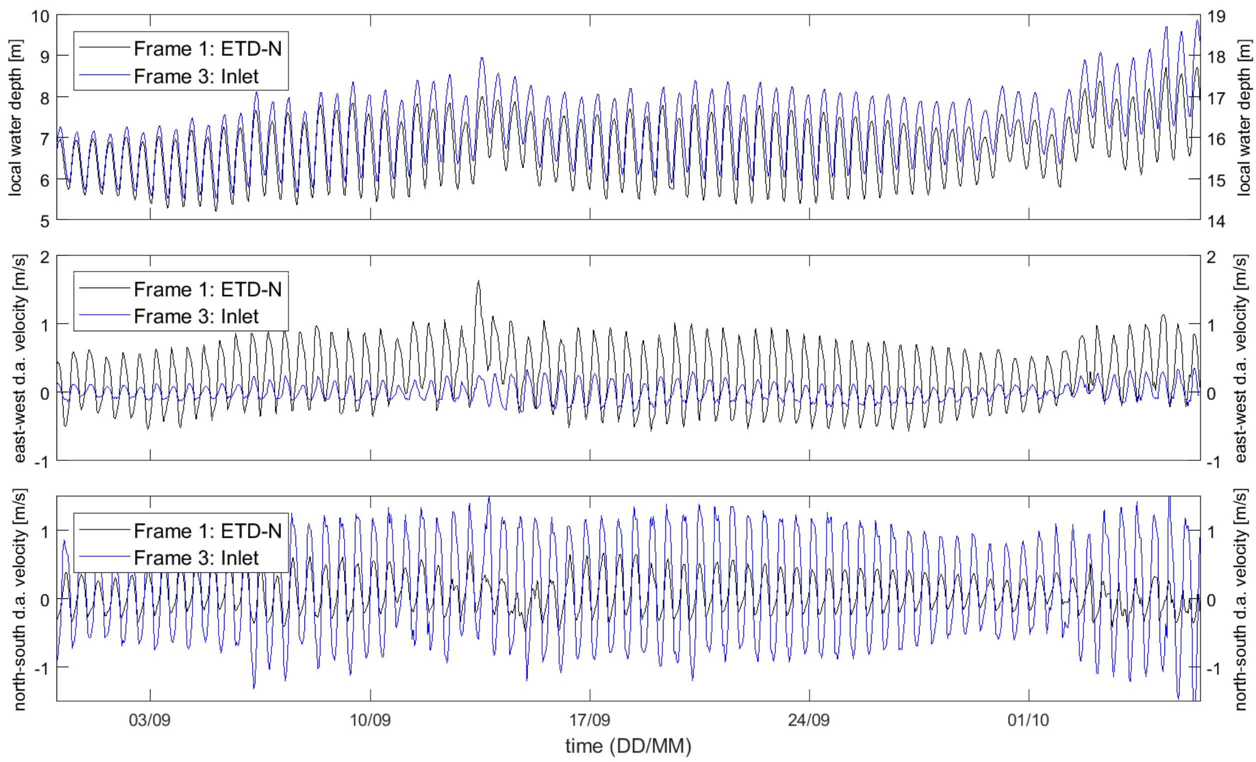

Figure 3.1: Measured time series of the local water depth (top) and of depth-averaged velocities in eastward (middle) and in northward direction (bottom) for observation points at the ebb-tidal delta (Frame 1: ETD-N (d = 6.8 m); black lines, left axis) and in the tidal inlet (Frame 3: Inlet (d = 16.3 m); blue lines, right axis).

amplitude here than based on a long-term record of the water level at station Terschelling Noordzee (Elias, 2017b), where A_{S_2} = 0.24 m. Since it is not expected that the S_2 component is significantly amplified over the ebb-tidal delta - and the difference between the amplitudes found here and found by Elias (2017b) is thus not something physical - it is expected that parts of the non-tidal energy and energy of other tidal constituents have been appointed to the S_2 component in the harmonic analysis. One of these constituents is the L_2 component, which has an amplitude of approximately 0.07 m, according to Elias (2017b).

- The M_2 tidal wave arrives first at Frames 4 and 5 and subsequently at Frame 1 and at Frame 3. It takes the tidal wave roughly 20 minutes to propagate from Frames 4 and 5 to the inlet (details of the harmonic analysis at Frames 4 and 5 are included in Appendix A).
- The shallow water constituents M_4 and M_6 have relatively little energy in the water level signal (i.e. $A_{M_4} \approx 6$ cm and $A_{M_6} \approx 3$ cm). The development of these two shallow water constituents would be most important for a possible asymmetry in the tidal current.
- Taking into consideration the 95% confidence intervals, it is hard to investigate differences in the amplitudes of the constituents at the different locations. There is a difference between the amplitude of K_2 at the different locations for which no physical explanation was found.

In general, the harmonic analysis on the water level time series provides a first introduction into the constituents that generate the water level variation at the different locations. However, relatively large 95%confidence intervals around the outcomes regarding harmonic constituents that contain relatively little energy indicate a poor fit of the harmonic signals to the 40-days water level records. It is expected that this is induced by the limited duration of the record in combination with nonstationary disturbances in the recorded signal.

Table 3.2 lists the characteristics of the same ten tidal constituents in the time series of depth-averaged flow velocities. The definition of parameters in Table 3.2 is explained in Figure 3.2. Because the IRLS minimization method did not converge after 2500 iterations, the harmonic analysis is based on the OLS minimization method (see Section 2.4). The orientation of the tidal ellipse is given as the orientation of the ellipse's major axis ($0° \leq \theta \leq 180°$).

	Frame 1: ETD-N (d = 6.8 m)		
	A [m]	ϕ [°]	E [%]
M_2	0.85 ± 0.01	247 ± 1	79.4
S_2*	0.36 ± 0.01	295 ± 2	13.9
K_2	0.14 ± 0.01	51 ± 6	2.1
MU_2	0.11 ± 0.01	346 ± 7	1.2
N_2	0.10 ± 0.01	225 ± 7	1.1
O_1	0.08 ± 0.01	214 ± 9	0.8
K_1	0.07 ± 0.02	22 ± 9	0.6
M_4	0.07 ± 0.01	343 ± 11	0.5
MS_4	0.06 ± 0.01	56 ± 13	0.4
M_6	0.03 ± 0.01	101 ± 25	0.1

	Frame 3: Inlet (d = 16.3 m)		
	A [m]	ϕ [°]	E [%]
M_2	0.86 ± 0.01	256 ± 1	75.5
S_2*	0.40 ± 0.01	305 ± 2	16.6
K_2	0.19 ± 0.01	74 ± 4	3.6
MU_2	0.12 ± 0.01	352 ± 7	1.5
N_2	0.09 ± 0.01	228 ± 9	0.9
O_1	0.10 ± 0.02	218 ± 10	1.0
K_1	0.05 ± 0.01	47 ± 15	0.3
M_4	0.05 ± 0.01	346 ± 11	0.3
MS_4	0.05 ± 0.01	65 ± 11	0.3
M_6	0.03 ± 0.02	112 ± 22	0.1

Table 3.1: Amplitude (A) and phase angle (ϕ) of ten tidal constituents in the time series of the water level at two different locations. Energy (E) is the energy percentage of the tidal constituents in the harmonic signal. The amplitudes and the phase angles are listed together with the 95% confidence interval of results. Phase angles are corrected to Greenwich time (GMT).
* based on the Rayleigh criterion, the results for S_2 are biased by energy of at least the L_2 constituent.

Table 3.2 shows that only the M_2 component has been resolved within acceptable limits of accuracy: The confidence interval around the amplitude does not exceed 10% of the magnitude and the phase angle is given within a confidence interval of maximum 3°. Other observations are the following:

- The M_2 tidal current reaches a depth averaged velocity of around 1 m/s at the observation point in the inlet's channel. At the three locations at the ebb-tidal delta, the tidal currents are of similar magnitude, although the amplitude of the tidal current is slightly larger at the two more shallow locations (Frame 1 and Frame 5 in relation to Frame 4).
- The phase angles between the vertical and the horizontal M_2 tide are approximately 55° and 70° at Frame 1 and at Frame 3, respectively. These phase differences indicate that the semi-diurnal tidal wave is both partially progressive and standing. At the inlet, the tidal wave has more of a standing character.
- In the tidal inlet, the tidal current is obviously aligned with the orientation of the channel (θ_{M2} = 99°). At the northwestern part of the ebb-tidal delta, the depth-averaged M_2 ellipses are orientated more or less in the east-west direction (i.e. θ_{M2} = 167° for Frame 4 and 161° for Frame 5). At Frame 1 the major axis of the M_2 ellipse is orientated from south-east (flood) to north-west (ebb, θ = 150°).
- The phase angles of the shallow water overtides M_4 and M_6 were resolved within 95% confidence intervals up to ± 54°. These large confidence intervals make the outcomes of the harmonic analysis unreliable for detailed analyses and/or tidal forecasting; based on this information flow asymmetries cannot be investigated.

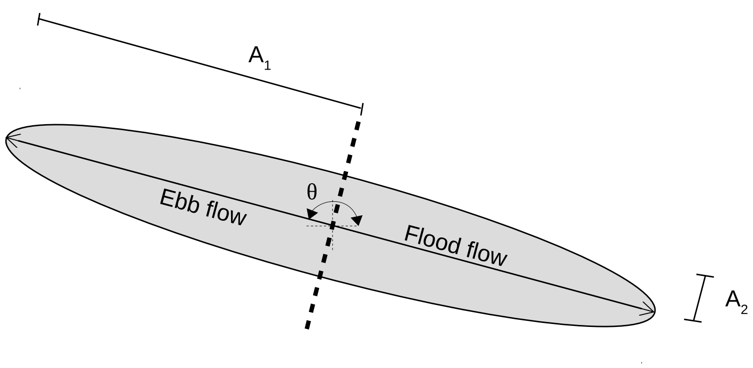

Figure 3.2: Definition of ebb flow and flood flow for an M_2 tidal ellipse of which the orientation is given by θ. The dashed line separates ebb flow and flood flow. A_1 and A_2 are the amplitudes along respectively the semi-major and the semi-minor axis. θ is defined positive counter-clockwise, relative to the positive x-axis.

Frame 1: ETD-N (d = 6.8 m)					
	A_1 [m/s]	A_2 [m/s]	θ [°]	ϕ [°]	E [%]
M_2	0.61 ± 0.03	0.05 ± 0.02	150 ± 2	6 ± 3	68.0
S_2*	0.33 ± 0.03	-0.04 ± 0.02	151 ± 3	63 ± 6	20.3
K_2	0.20 ± 0.03	-0.07 ± 0.02	155 ± 9	217 ± 13	7.8
MU_2	0.1 ± 0.03	0.03 ± 0.02	154 ± 11	113 ± 20	2.0
N_2	0.08 ± 0.03	0.00 ± 0.02	147 ± 15	326 ± 25	1.1
M_6	0.05 ± 0.02	0.01 ± 0.01	175 ± 20	290 ± 54	0.4
M_4	0.03 ± 0.01	-0.01 ± 0.01	103 ± 11	65 ± 15	0.2
MS_4	0.02 ± 0.01	0.02 ± 0.01	176 ± 158	196 ± 166	0.1
K_1	0.02 ± 0.02	0.00 ± 0.01	15 ± 36	43 ± 47	0.1
O_1	0.02 ± 0.01	-0.00 ± 0.01	123 ± 36	311 ± 39	0.1

Frame 3: Inlet (d = 16.3 m)					
	A_1 [m/s]	A_2 [m/s]	θ [°]	ϕ [°]	E [%]
M_2	0.98 ± 0.04	0.03 ± 0.01	99 ± 1	12 ± 2	87.0
S_2*	0.27 ± 0.03	-0.03 ± 0.01	94 ± 2	63 ± 7	6.8
MU_2	0.16 ± 0.04	0.01 ± 0.01	101 ± 3	95 ± 12	2.4
N_2	0.15 ± 0.03	-0.00 ± 0.01	107 ± 3	354 ± 14	2.0
K_2	0.10 ± 0.03	-0.00 ± 0.01	122 ± 7	123 ± 21	1.0
M_6	0.08 ± 0.03	0.00 ± 0.00	95 ± 2	259 ± 22	0.5
K_1	0.03 ± 0.01	0.01 ± 0.00	95 ± 8	138 ± 22	0.1
O_1	0.03 ± 0.01	0.01 ± 0.00	105 ± 10	305 ± 23	0.1
MS_4	0.03 ± 0.01	0.00 ± 0.00	115 ± 5	295 ± 31	0.1
M_4	0.03 ± 0.02	-0.00 ± 0.01	124 ± 12	255 ± 38	0.1

Table 3.2: Amplitudes along the semi-major axis (A_1) and along the semi-minor axis (A_2), orientation angle of the tidal ellipse (θ), and phase angle (ϕ) of ten tidal constituents in the time series of depth-averaged velocities at the ebb-tidal delta (Frame 1) and in the inlet (Frame 3). The amplitudes and the phase angles are listed together with the 95% confidence interval of results. Energy (E) is the energy percentage of the tidal constituents in the harmonic signal. Phase angles are corrected to Greenwich time (GMT). Negative amplitudes indicate a clockwise rotation along the tidal ellipse. * based on the Rayleigh criterion, the results for S_2 are biased by energy of at least the L_2 constituent.

In general, the harmonic analysis of depth-averaged velocity records does not provide a satisfying description of the tidal current. Only the characteristics of energetic tidal constituents were resolved within acceptable accuracy limits. For tidal constituents containing less energy, the amplitudes, the orientation, and the phase angle were resolved within large 95% confidence intervals. Apparently, the non-tidal energy in and around Ameland Inlet is this high that tidal harmonics cannot be considered as stationary in a 40 days records. The representation of the time series by the first 10 harmonic constituents is worse for the velocity record than for the water level record. The latter is in correspondence with earlier findings that tidal currents are more sensitive to nonstationary variations than water levels (e.g. Flinchem and Jay, 2000; Godin, 1983; Guo et al., 2015). To investigate the nonstationarity of the tides further, the next sections discuss the variation in flow asymmetry and the application of continuous wavelet transforms.

3.2. Flow reversal and asymmetry

This section considers the moment of flow reversal, and thus the duration of ebb and flood, as well as the peak velocities in ebb- and flood-direction. A tidal period is defined as an M_2 harmonic period (see Chapter 2). The mean current velocity over the duration of the field campaign is nonzero. This affects the duration of ebb and flood; a residual current in the direction of flood extends the duration of flood, for example. Figure 3.2 shows how ebb flow and flood flow are defined for a tidal ellipse of which the orientation is given by θ.

In order to exclude the orbital motion of wind waves from the flow record, depth-averaged velocities are averaged over a duration of 6 minutes. The duration of depth-averaged flow in flood-direction and the duration of depth-averaged flow in ebb-direction are then determined for every M_2 harmonic period. The results are shown in Figure 3.3 for the four different observation points. The results in this figure are not intended to address tidal asymme-

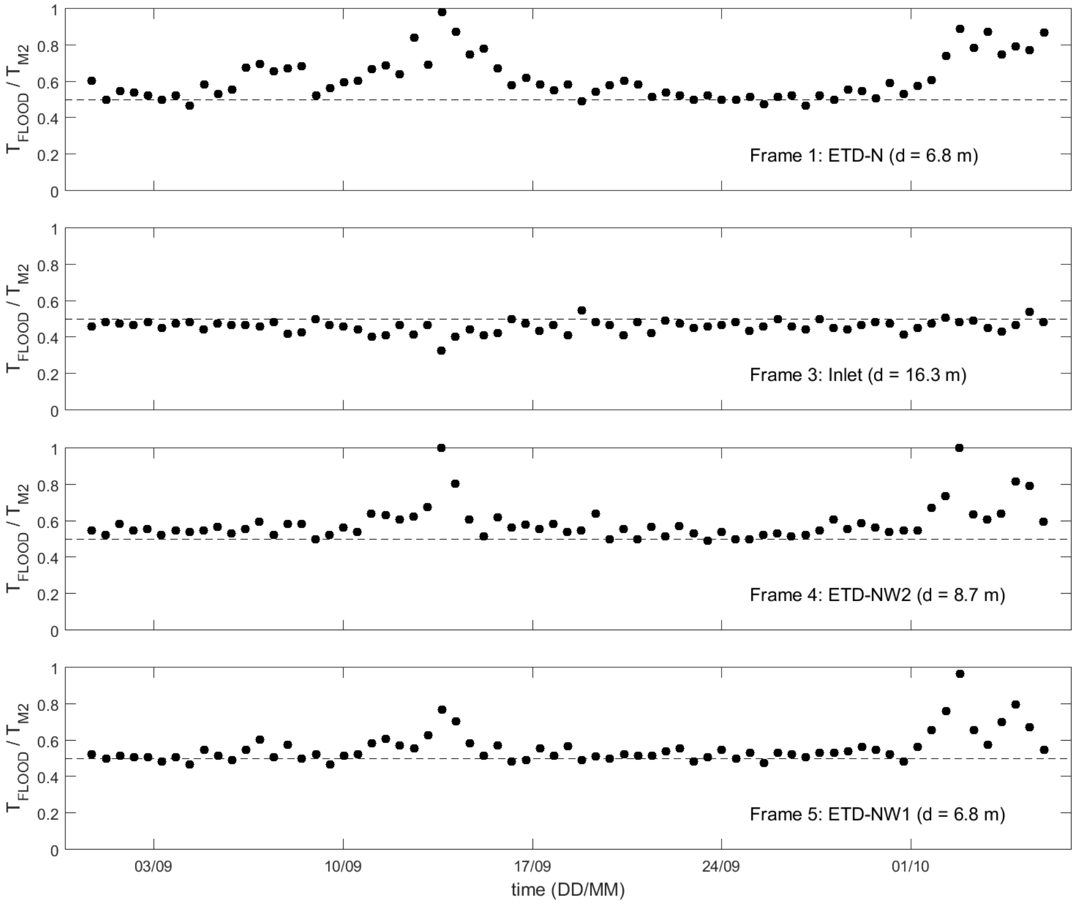

Figure 3.3: Fraction of time during an M_2 tidal cycle that the depth-averaged current was directed in the direction of flood. 69 M_2 tidal periods are included in the records that were obtained at four different locations.

tries, because it is not just the tide that causes the differences between durations of ebb and flood. The results help, however, to investigate the residual flow characteristics and the nonstationarity of the tidal motion.

Figure 3.3 shows a strong variation of the ebb- and flood duration over time. It appears that storm events and related currents can prevent the tidal flow from reversing at the ebb-tidal delta, such that the depth-averaged flow is in the flood-direction for the duration of more than 1.5 tidal periods. The storm event at September 13th led to a longer duration of the eastward directed flood at the ebb-tidal delta. At Frame 3 the duration of ebb flow increased, which corresponds to a longer period of outflow through Ameland Inlet. The fraction of the tidal cycle during which the flow at Frame 3 was outward directed varies between 45% and 67% during the measurement campaign. On average, the depth-averaged flow at the ebb-tidal delta was in the direction of flood during 61%, 59% and 56% of the M_2 period at Frame 1, Frame 4 and Frame 5, respectively. The differences between these locations might be explained by the development of both wind- and wave-induced currents, on which Chapter 4 will elaborate.

During the timespan with calm weather conditions between the two windstorms (second half of September, see Figure 2.4), the duration of flood still exceeds the duration of ebb during most tidal periods at the ebb-tidal delta. At Frame 3, it is still the ebb flow that extends more than half the tidal period during most tidal periods.

Next to the duration of ebb and flood, a difference in peak velocity between ebb and flood usually indicates tidal asymmetries: In a pure tidal signal a longer ebb than flood period corresponds to a larger peak velocity in flood-direction (and vice versa) (e.g. Gatto et al., 2017; Van de Kreeke and Robaczewska, 1993). Figure 3.4 shows the peak velocities in both ebb- and flood-direction per tidal period in the record. In general, the maximum velocities at the ebb-tidal delta are larger in flood-direction (Frame 1, 4, and 5), which corresponds to a stronger flow in eastward direction. The flow through the inlet's main channel (Frame 3) is characterised by larger peak flows in ebb-direction.

In combination with what was found about the ebb- and flood durations (see Figure 3.3), these findings show that the flow around Ameland Inlet cannot be described by classical parameters for tidal asymmetries. Even during calm weather conditions a nonstationary residual flow over the ebb-tidal delta makes both the peak flood flow larger than the peak ebb flow and the flood duration longer than the ebb duration. At the observation point in the inlet, the peak ebb flow is stronger and the ebb duration exceeds the flood duration.

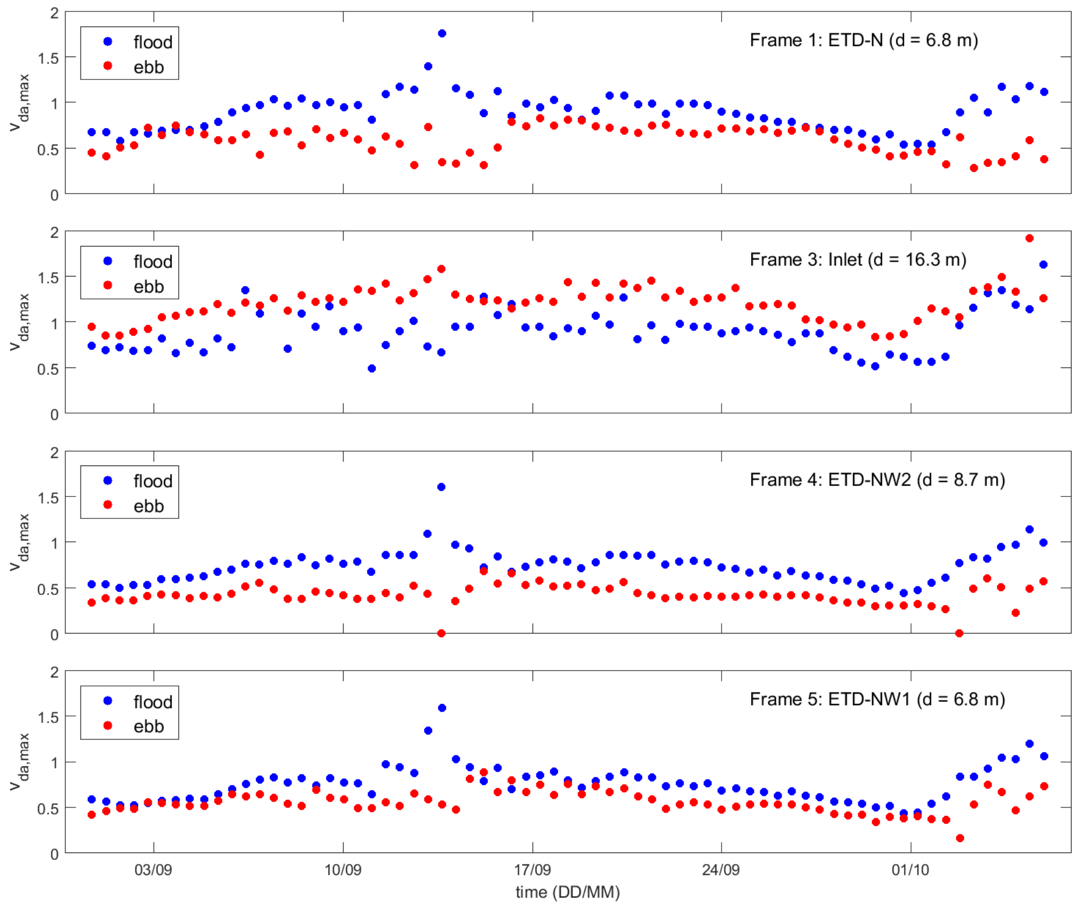

Figure 3.4: Absolute values of the maximum depth-averaged velocities in flood-direction (blue) and in ebb-direction (red) per M_2 tidal period. 69 M_2 tidal periods are included in the records that were obtained at four different locations.

3.3. Continuous wavelet transforms

By using continuous wavelet transforms (CWT), the nonstationary variations of tidal harmonics can be investigated. Different tidal bands can be separated by CWT analysis (e.g. the diurnal band (D_1), the semidiurnal band (D_2) and the quarter-diurnal band (D_4)), but different constituents within one band are seen together. The CWT analysis is applied to time series of water levels and depth-averaged current velocities. Separate CWT analyses are applied to east- and northward directed currents, since different bands have different orientations of the major axis.

Figure 3.5 shows the results of the CWT analysis on time series obtained at the ebb-tidal delta (Frame 1) and in the inlet (Frame 3) by the continuous wavelet power spectra. The top figure relates to the water level time series and the middle and bottom figures relate to the depth-averaged velocities in east- and northward direction, respectively. The white dashed lines indicates the cone of influence; information below this line is unreliable due to edging effects.

The dominant D_2 band (T = 1/2 day) is clear in both the water level variation and the current. A spring-neap variation in the D_2 band is present in the water level signal and, although less pronounced, in the depth-averaged velocities. Storm events at September 13$^{\text{th}}$ and at the beginning of October are captured in the wavelet power spectra by low-frequency fluctuations. Part of the energy of these meteorological events is in the D_1 band (T = 1 day), which makes it

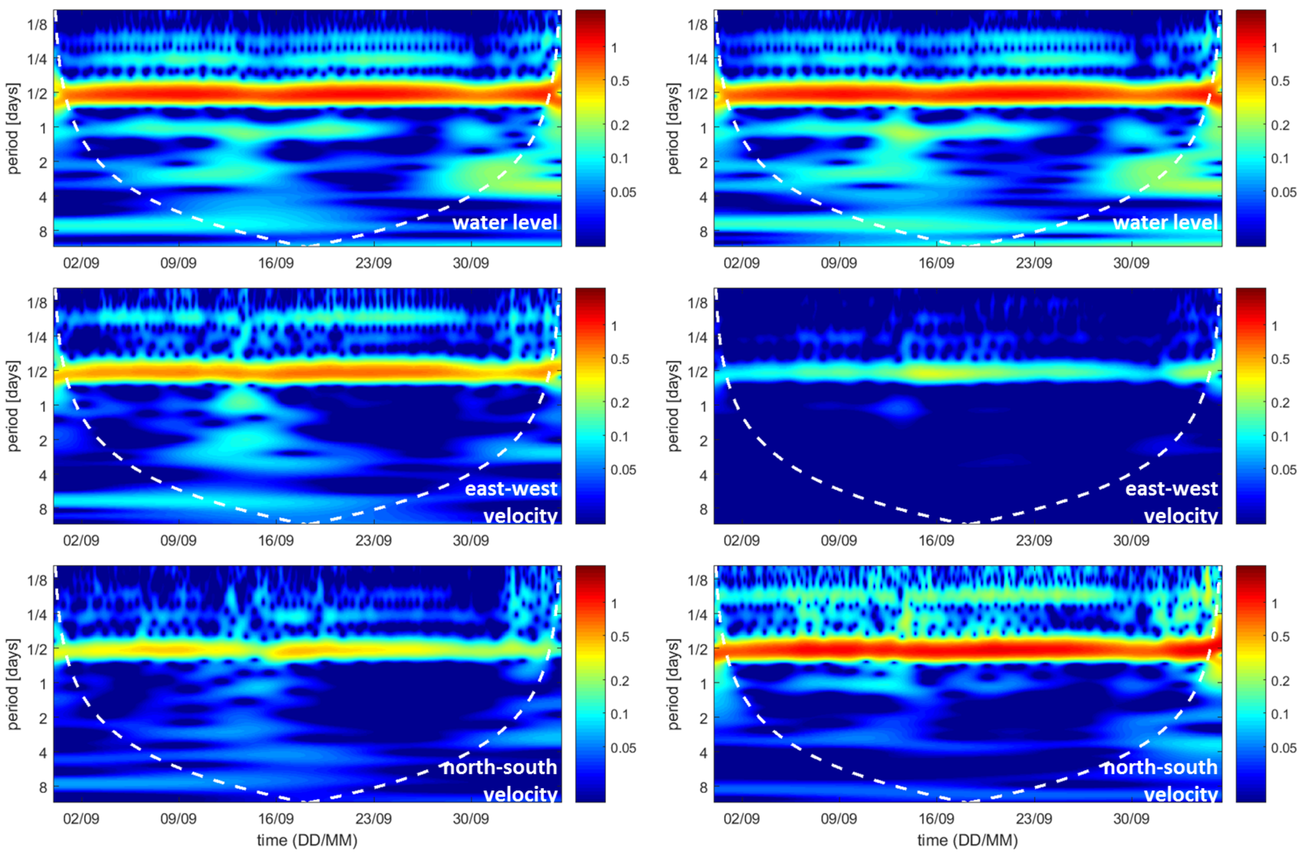

(a) Frame 1: ETD-N (d = 6.8 m)

(b) Frame 3: ETD-N (d = 16.3 m)

Figure 3.5: Continuous wavelet power spectra of time series of the water level (top), depth-averaged east-west velocity (middle) and depth-averaged north-south velocity (bottom) at Frame 1: ETD-N **(a)** and at Frame 3: Inlet **(b)**. The colour indicates the wavelet power and thereby the energy of oscillations in the record. The cone of influence is indicated by the white dashed line.

difficult to investigate the variation of diurnal tidal constituents over time. It follows from the wavelet power spectra - however - that the D_1 band has a relatively stronger signal in the water level than in the depth-averaged current. The variation in the D_1 band over time - be it induced by both meteorological events and by varying diurnal constituents or by meteorological events only - explains the large confidence intervals regarding diurnal constituents in the results of harmonic analysis.

The D_4 band (T = 1/4 day) is particularly present in the water levels, whereas this band is less pronounced in the depth-averaged current. The D_6 band is clearly present in both the water level and the current. The variation in the D_4 band and in the D_6 band (T = 1/6 day) follow the spring-neap variation in the D_2 band; both the D_4 band and the D_6 band have larger magnitudes during spring tide. The spring-neap variation is disturbed by events of lower frequency (T > 1 day), which are related to highly-energetic meteorological events, leading to irregular variations in time. The irregular variations of significant magnitude show the nonstationarity of the tides at this location. This again explains the large confidence intervals in the stationary harmonic analysis.

The shallow water overtides M_4 and M_6 are the most relevant constituents for tide-induced net sediment transport (e.g Chu et al., 2015; Gräwe et al., 2014; Kreeke and Robaczewska, 1993). It is for that reason that the remaining part of this section elaborates on the occurrence of these overtides in the tidal signal. Figure 3.6 shows the wavelet power spectrum for the frequencies of the M_4 and M_6 constituents in the records of water level and depth-averaged velocity in relation to the ratio of the tidal amplitude over the mean water depth per tidal cycle. The latter includes the spring-neap cycle in the water level record. The changes in energy of the shallow water overtides in the water level signal follow the changes in the mentioned ratio. This demonstrates that the water level variations in the D_4 and D_6 bands in the wavelet power spectra indeed follow the spring-neap variation, as was suggested earlier in this section. This finding is in agreement with Friedrichs and Aubrey (1988), who found that non-linear tidal distortion in shallow

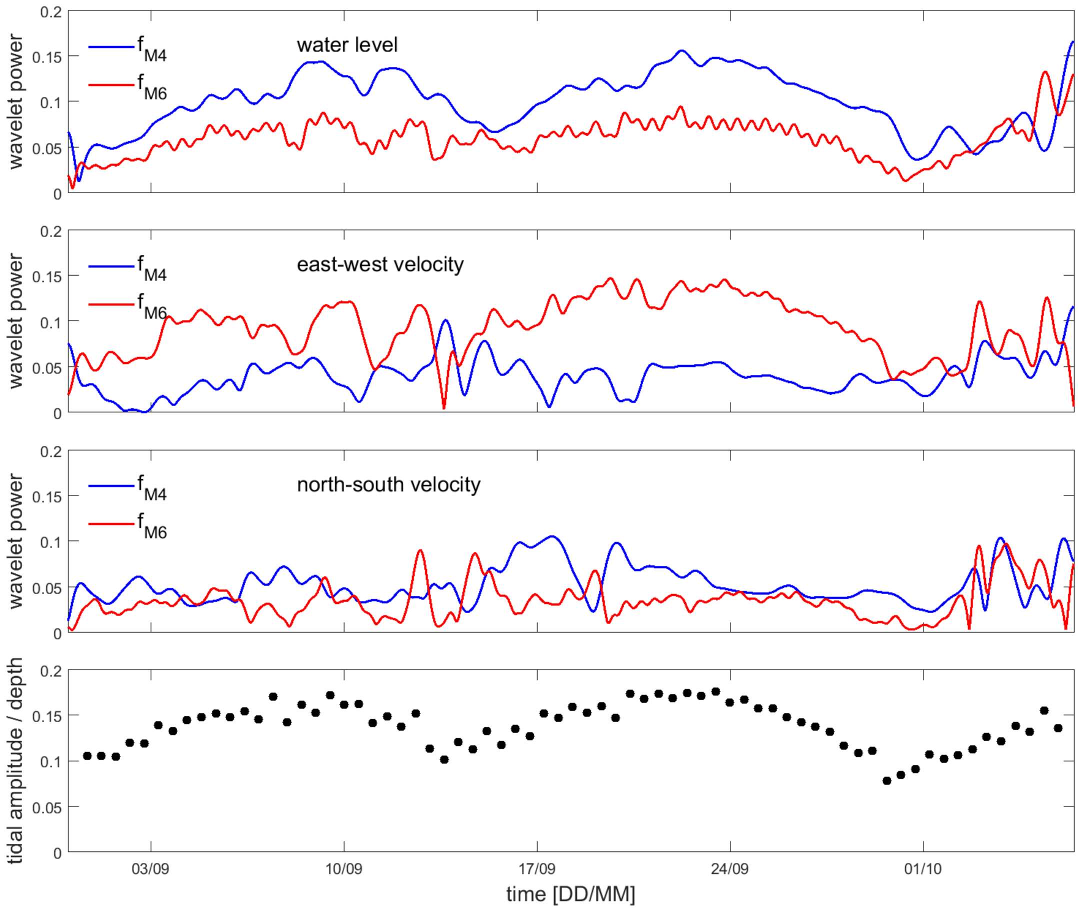

Figure 3.6: Wavelet power with the frequency of shallow water overtides M_4 and M_6 in the wavelet power spectra of the water level (1/4), eastward velocity (2/4), and northward velocity (3/4), and the ratio of tidal amplitude over water depth per tidal cycle in the record (4/4). Records obtained at Frame 1 are used for illustration. Note that the wavelet power at the start and at the end of the record is affected by edging effects.

water is partly caused by the frictional interaction between the tidal wave and the seabed; the frictional interaction was expressed as the ratio between the tidal amplitude and the channel depth. In addition to the variation with the period of a spring-neap cycle, the wavelet power at the M_6 frequency also shows a variation with the period of an M_2 period. Further analysis showed that the wavelet power is highest just after low water: This suggests that even some parts within the M_2 cycle are more favourable for the development of the M_6 overtide than others.

The flow variations in the D_4 and D_6 bands do not necessarily follow the spring-neap cycle. The cycle can be recognised at the frequency of the M_6 constituent around the second spring tide in the record, which is between the two windstorms during the field campaign (September 13th and October 5th). Further, the (strong) variation in wavelet power cannot be explained based on the ratio of the tidal amplitude over the water depth. Apparently, the presence and magnitude of shallow water overtides in the depth-averaged flow is highly nonstationary. The origin of this nonstationarity is investigated using numerical model simulations in the next section of this chapter.

3.4. Tidal disturbances in model simulations

The flow conditions during the 40-days field campaign are reproduced using the numerical model and the results are analysed using continuous wavelet transforms. Disabling the forcing mechanisms one by one (see Section 2.5) helps to investigate what mechanisms make the tidal motion this nonstationary during the 40 days field campaign. The results are discussed for an observation point in the model domain, approximately at the location of Frame 1: ETD-N. Continuous wavelet power spectra are presented in Figure 3.7. Here, only spectra of the water level signal and of the east-west velocity are included for illustration.

Part **D** of Figure 3.7 shows that time series of the water level and the depth-averaged velocity are harmonic in case the model is only forced by tidal water level variations at the model boundaries. In this simulation there is no forcing mechanism that leads to disturbances of the harmonic water movement. In agreement with the harmonic analysis, it is shown that variations in the diurnal band have less energy in the depth-averaged velocity signal than in the water level signal. Including surge at the water level boundaries leads to disturbances in the water level signal at multiple frequency bands. The depth-averaged velocity is especially affected by surge in the D_4 and D_6 bands. This indicates a different development of shallow water overtides due to surge. Including local wind shear stresses and waves hardly changes water level variations in frequency bands that are of interest here. On the other hand, the local wind shear stresses are responsible for mixing up the harmonic flow signal at tidal frequencies and for generating flow variations at lower frequencies (T > 1 day). Wave-induced currents further amplify the disturbances of the harmonic flow signal. A quantitative analysis of the non-tidal forcing mechanisms will follow in Chapter 4.

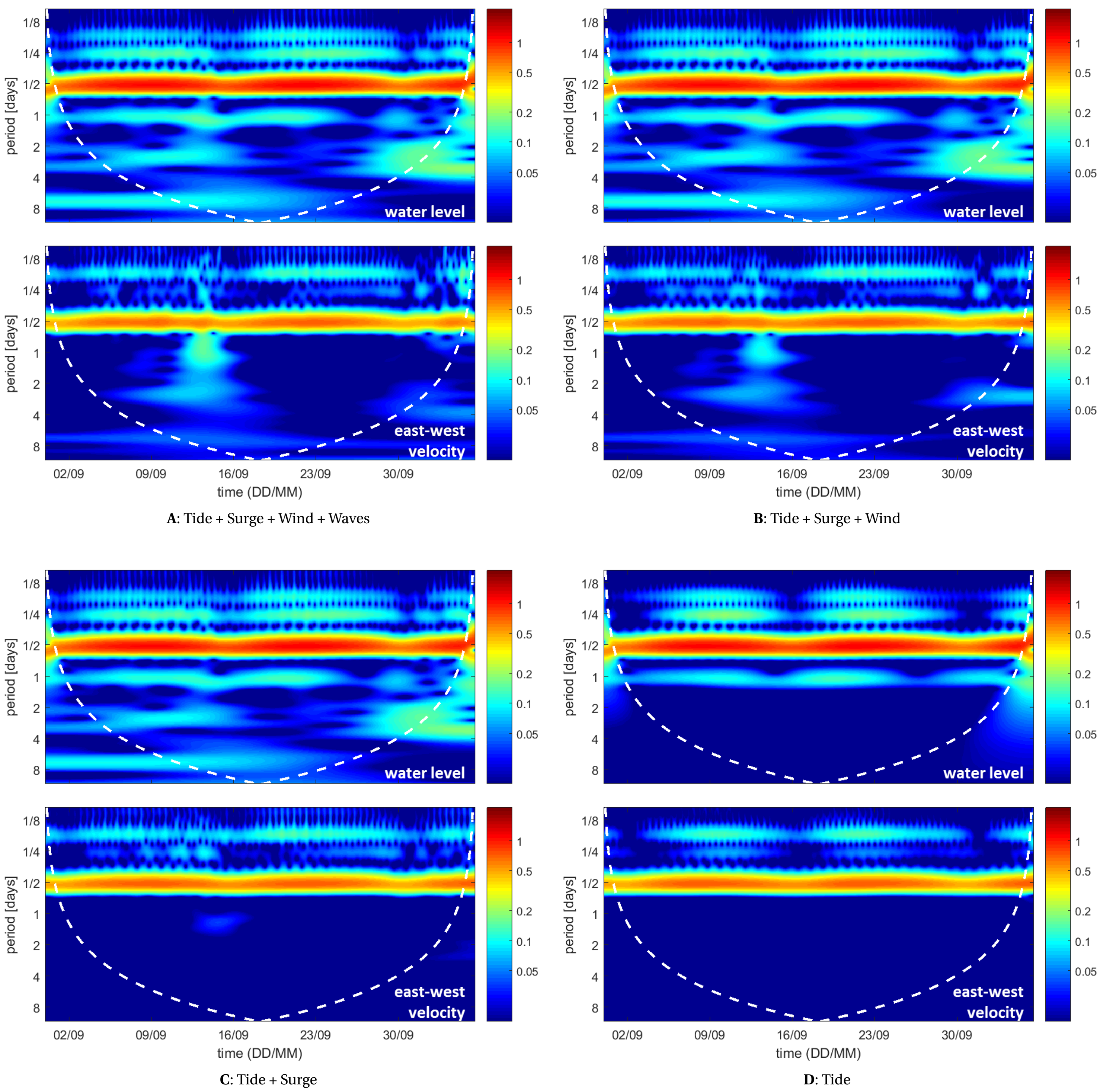

Figure 3.7: Continuous wavelet power spectra of time series of the water level (top) and depth-averaged east-west velocity (bottom) at location Frame 1: ETD-N, based on numerical modelling results of four simulations (**A**, **B**, **C** and **D**) with different sets of forcing mechanisms enabled.

Key points

- A stationary harmonic analysis of 40-days time series of water levels and depth-averaged flow velocites, obtained around Ameland Inlet, yields unreliable results. This is concluded from large confidence intervals around the results. The results of the harmonic analysis can hardly be used for tidal analysis and/or forecasting.
- Non-tidal forcing mechanisms (i.e. meteorological forcing) can induce a residual current over the ebb-tidal delta of Ameland Inlet that is as large as the ebb-current during storm conditions. The residual current then prevents flow from reversing.
- Results of continuous wavelet transforms show that non-tidal physical processes disturb the occurrence and magnitude of harmonic tidal constituents in observed time series. Shallow water overtides M_4 and M_6 are more severely affected in records of the depth-averaged flow velocities than in records of the water level.
- It follows from modelling results that disturbances in the harmonic water level variation are particularly induced by surge. The depth-averaged velocity record at the ebb-tidal delta is nonstationary due to wind, waves and surge. Local wind shear stresses are a large energy source for disturbances of te harmonic flow signal.

4

Non-tidal physical processes

Exploring the effect of wind

This chapter aims to relate field observations on surge and residual transport at various locations in Ameland Inlet system to meteorological forcing conditions. Section 4.1 first discusses the wave conditions observed during the field campaign in relation to the wind conditions. Later sections discuss the surge and residual discharge at various observations points. Modelling results are used to unravel the effect of different forcing mechanisms. In the end of this chapter, the observed flow conditions are used to compute the sediment transport capacity per event.

4.1. Waves and wind

Waves near Ameland Inlet are mostly local wind-generated waves. Based on wave measurements over the period 2007-2017, Elias (2017b) found that contributions of swell (T_{wave} > 9 seconds) are minor (≈ 0.1%). During the 40 days measurement campaign, the significant wave height at the ebb-tidal delta exceeded 4.5 m during storm conditions. Figure 4.1 shows the wave roses at three observation points at the ebb-tidal delta for the duration of the field campaign. Only waves from offshore direction are considered. Waves were mainly coming from the north-northwest. This is particularly true for higher waves (H_{m_0} > 3 m), since these were only observed coming from the north-northwest. This dominant direction for waves is enforced by the geographic location and orientation of Ameland Inlet in relation to the shape of the relatively shallow North Sea. In addition to waves from the dominant direction, smaller waves (H_{m_0} < 2 m) from the north-northeast were observed during the field campaign. The height of these waves is limited by the short fetch in combination with relatively weak winds from this direction (see Chapter 2).

At the measurement frame in the main channel of the tidal inlet (Frame 3), the significant wave height did not exceed 1 m, which demonstrates the effectiveness of the ebb-tidal delta in the dissipation of wave energy. Although the three locations at the ebb-tidal delta are relatively close, there are some differences in the observed wave field. The largest waves are measured at Frame 4, for example, and at Frame 1 the fraction of waves from the north is larger. These differences are expected to be induced by interactions between the waves and the seabed (i.e. shoaling, breaking, refraction), of which the details are not part of this study.

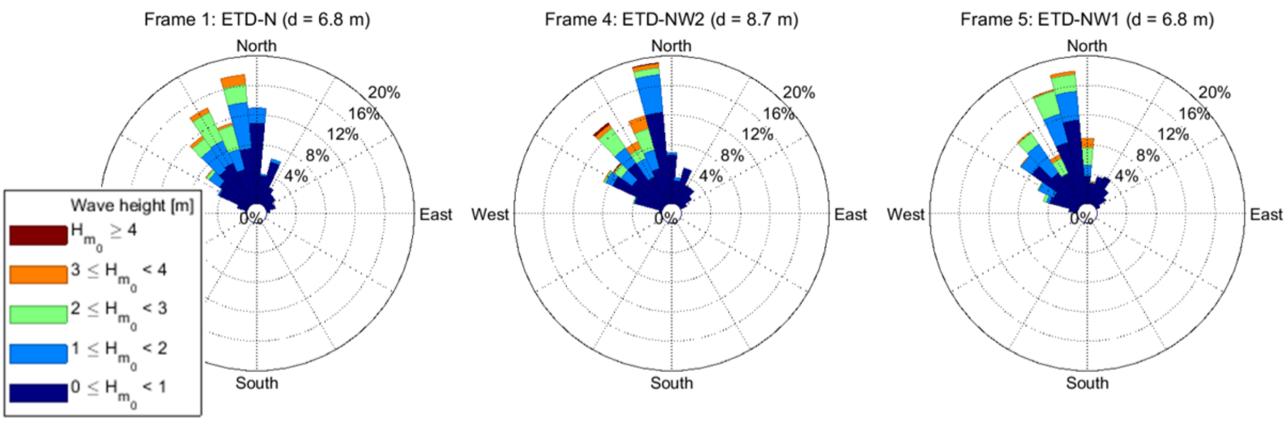

Figure 4.1: Wave roses of observed surface waves during the field campaign at three different locations at the ebb-tidal delta of Ameland Inlet. Only waves coming from offshore direction are considered.

The wind conditions that were observed during the field campaign were discussed in Section 2.2. Particularly strong winds were dominantly coming from the west/southwest. It was mentioned already that waves around Ameland Inlet are locally generated by wind. To investigate the correlation between wind and wave characteristics, Figure 4.2 relates the significant wave height (H_{m_0}) to the average wind speed and wind direction. The scatterplots show a strong correlation between the wind speed and the significant wave height per burst, provided the wind is coming from offshore. Strong winds from the south-southwest, as observed relatively often during the field campaign (see Figure 2.3), do not generate high waves (H_{m_0}< 1.5 m) at the ebb-tidal delta of Ameland Inlet.

Both breaking waves and wind shear stresses are expected to contribute to a residual current over the ebb-tidal delta and around the tidal inlet, and to surge in the nearshore region. However, the strong correlation between the two makes it difficult to separate the contribution of waves and wind to surge and residual currents. Later in this chapter, the different forcing mechanisms are unravelled by using modelling results. In the analysis of field data, the wave- and wind-induced currents are considered together. The exact forcing mechanisms then remain unknown.

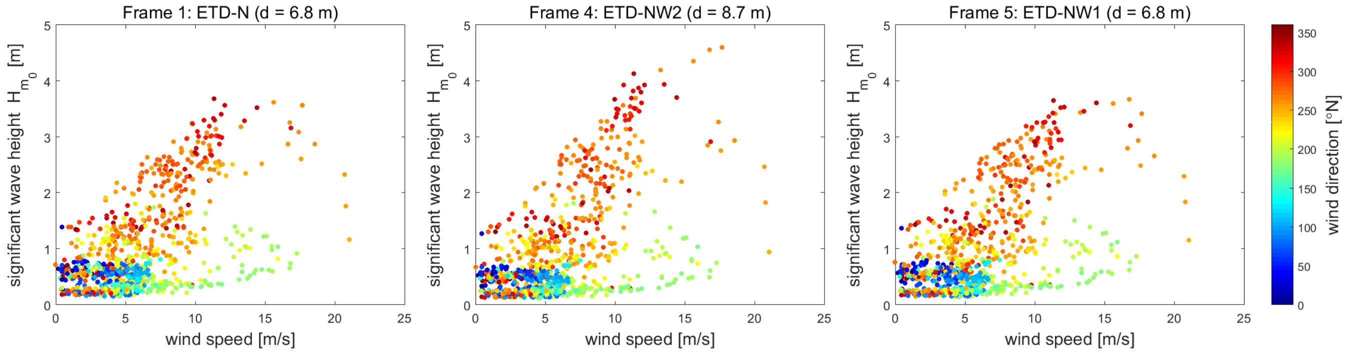

Figure 4.2: Relation between the wind conditions (i.e. speed and direction) and the significant wave height (H_{m_0}), as observed during the field campaign at three different locations at the ebb-tidal delta. Every dot represents the conditions during a burst of half an hour. The wind conditions are measured at KNMI station Hoorn Terschelling.

4.2. Water level set-up

In this section the large-scale water level variations induced by wave- and wind-induced set-up are investigated based on field observations. Because the tide dominates the water level variation, this section specifically considers the variation in tide-averaged water levels. Water levels are therefore averaged over an M_2 tidal cycle.

Figure 4.3 shows the water depth as measured during the field campaign at one locations at the ebb-tidal delta (Frame 4: ETD-NW2) and at one location in the tidal inlet's main channel (Frame 3: Inlet). Time series of the variation in water depth at the other two locations at the ebb-tidal delta (i.e. Frame 1: ETD-N and Frame 5: ETD-NW1) look similar. To exclude the depth variations by surface waves, measured records are averaged over a burst of half an hour. The moment of maintenance to the measurement frames is indicated by the vertical dashed lines (see Section 2.2). Coloured dots represent the average water depth over a tidal cycle and indicate the water level set-up. Here, it is remarked that water level set-up is considered positive if the tide-averaged water level is above the average water level during the field campaign, which is biased by periods of strong set-up during the field campaign rather than by periods of strong set-down. The tide-averaged water depth shows a certain variation that relates to daily inequalities, induced by a combination of diurnal and semidiurnal constituents. One learns from Figure 4.3 further that fluctuations in the tide-averaged water depth are in the order of 1 m.

Since wind and wave conditions are strongly correlated, it is hard to distinguish wave- and wind-induced set-up based on the field data of a 40 days field campaign. Hence, wave- and wind-induced set-up are considered together in relation to the wind conditions (i.e. observed waves are generated by local winds). Figure 4.4 shows the tide-averaged set-up (set-down) above (below) the mean water depth for the tidal periods in the record in relation to the wind characteristics during the tidal period. In general, the set-up and set-down are very similar for the two locations. Again, figures regarding observation points Frame 1: ETD-N and Frame 5: ETD-NW1 would look similar.

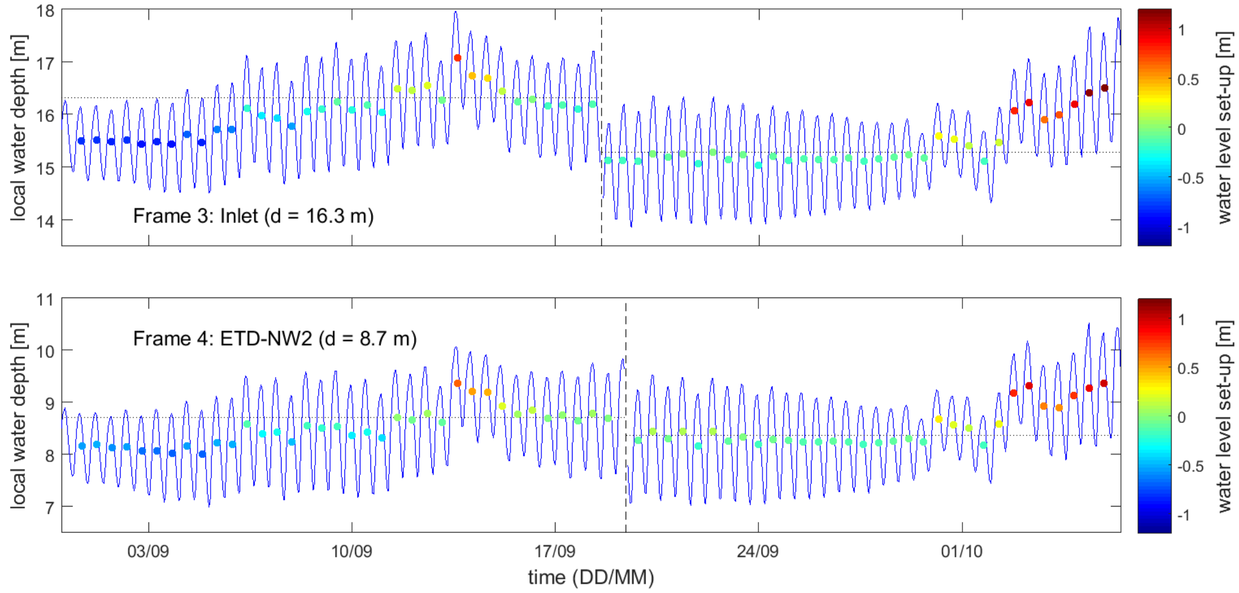

Figure 4.3: Time series of the local water depth as measured at Frame 3: Inlet (top) and at Frame 4: ETD-NW2 (bottom). Coloured dots represent the average water depth and the water level set-up per tidal cycle. The horizontal dotted line indicates the mean water depth. The vertical dashed line indicates the moment at which the measurement frame was lifted to the surface for maintenance; after servicing the frames were located at a slightly different location (see also Section 2.2).

Set-down was observed during strong winds from the southwest. At both locations, set-up was highest during strong winds from the west or northwest. The seven periods during which set-up was highest were successive periods at the end of the field campaign (see Figure 4.3). Apparently, wind and/or wave conditions were such that set-up was high for more than 3 days. Based on the information presented here, the set-up was likely enforced by the persistence of a strong wind from the west. For other wind conditions than strong winds from the west-northwest, observed set-up magnitudes are more scattered. Set-down is observed during winds from different directions.

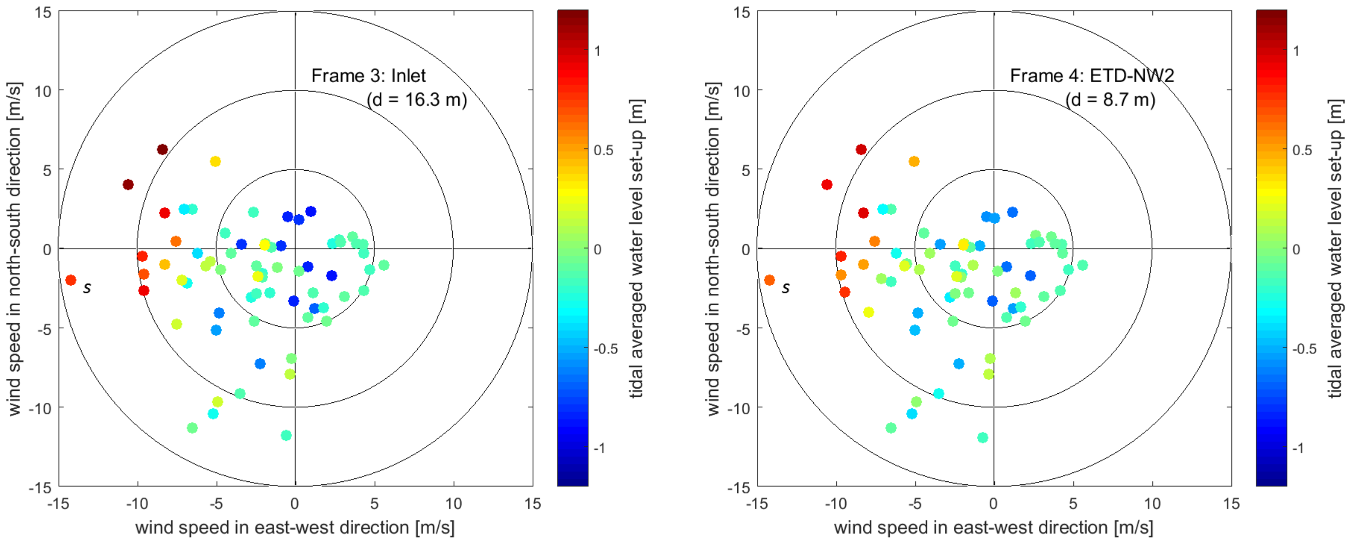

Figure 4.4: Average water level set-up over a tidal period in relation to the average wind conditions during that period. Every dot represents an M_2 tidal period during the field campaign. The place of the dot in the figure indicates the wind conditions. For example: A dot in the lower left quadrant indicates wind from the southwest and the distance to the origin indicates the average wind speed. A dot in the lower right quadrant indicates wind from the southeast. The *s* indicates the tidal period that includes the peak of the windstorm at September 13^{th}.

Next to set-up at the ebb-tidal delta and near the inlet, the set-up in the Wadden Sea is of particular interest for the flow through the tidal inlet. Set-up (or set-down) in the basin changes the volume of water in the tidal basin, and thus the flow through the inlet. Records of the water level in 2017 at permanent stations Nes and Holwerd, both located in the eastern part of the tidal basin (see Figure 2.2), are used to investigate the correlation between wind conditions and set-up in the tidal basin. Figure 4.5 shows the tide-averaged set-up at these locations in relation to the wind conditions per tidal period. The difference between maximum set-up and maximum set-down is approximately 2.5 m. The correlation with both the wind speed and the wind directions appears strong and similar for the two locations. Strong winds ($w_s > 10$ m/s) from the west-northwest generally cause a set-up at these two locations of around 1-1.5 m. Weaker winds from the same direction lead to a smaller set-up. During winds from the southwest, set-up at these locations is either zero or slightly positive. Less observed winds from the east and southeast generally cause a set-down of the water level.

The correlation between the set-up and the wind direction is enforced by the orientation of the tidal inlet system; set-up at Holwerd and Nes is high during winds from offshore (north-northwest) and set-down is high during winds from the land (south-southeast). Small differences in water level set-up are observed between the stations of Holwerd and Nes. The set-up at Holwerd is larger (smaller) if the wind is coming more from the north (south). This is inherent to the locations of these two observation points in the system. In addition, there seems to be an influence of the alongshore wind: Winds from the west contribute to set-up at Holwerd and Nes, whereas winds from the east contribute to set-down. This suggests an alongshore set-up over the tidal basin, possibly due to the geometry of the tidal basin (i.e. the Ameland Inlet basin becomes smaller towards the east).

The implications of surge in the Wadden Sea and at the ebb-tidal delta for flow through and around Ameland Inlet are investigated in the coming sections, based on field observations and modelling results.

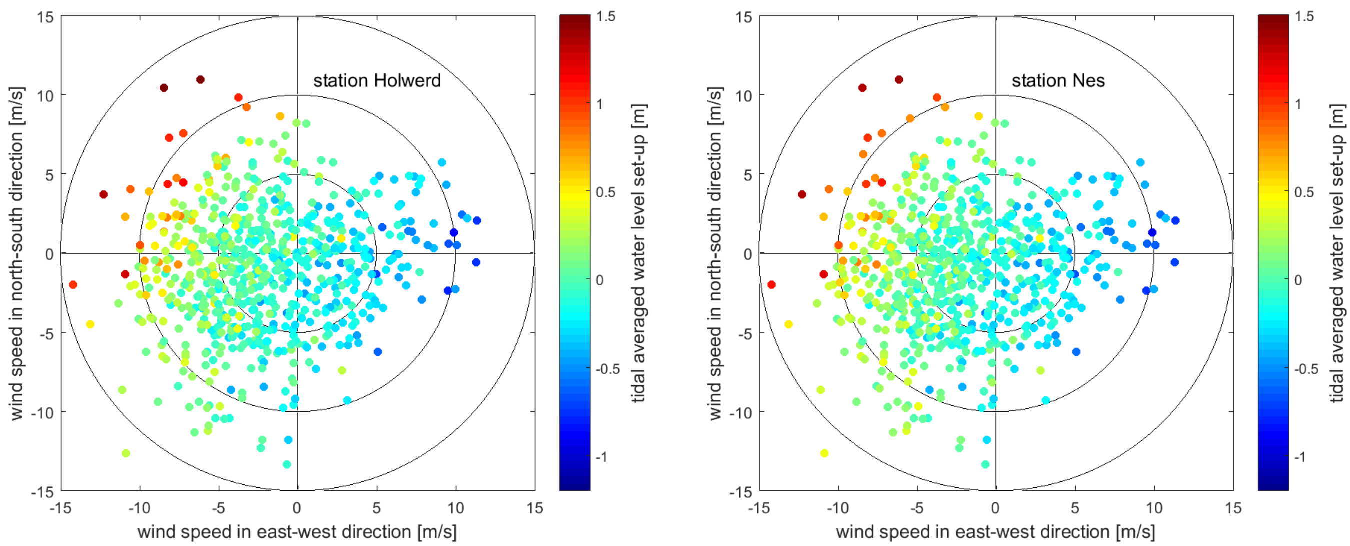

Figure 4.5: Tide-averaged water level set-up at permanent water level stations Holwerd (left) and Nes (right) in relation to the tide-averaged wind conditions. Every tidal period in 2017 is represented by a dot in the scatterplot. The place of the dot in the figure indicates the wind conditions.

4.3. Residual discharge

The first part of this section discusses flow measurement obtained at the three observation points at the ebb-tidal delta and the observation point in the tidal inlet's main channel. The subtidal discharges are then considered in relation to the wind forcing. The second part of this section includes modelling results to unravel the contribution of different forcing mechanisms.

4.3.1. Field observations

Figure 4.6 first shows the discharge per unit width in east- and northward direction for the four observation points. These figures are made up of burst-averaged values to exclude orbital motions by waves. Black dots present the average discharge per M_2 tidal cycle. In general, Figure 4.6 shows a residual discharge over the ebb-tidal delta in northeastward direction. During some tidal cycles, the discharge is more southeast directed. The plots that relate to Frame 3 show a residual discharge to the north, which implies a net outflow from the basin at this location in the inlet.

Although the instantaneous discharge is dominated by the tidal motion, the residual discharge is not. The residual discharge is here considered as the net discharge over an M_2 harmonic tidal period. The residual discharge per tidal period is considered in relation to the tide-averaged wind conditions in Figure 4.7. The field campaign covered 69 tidal periods; every tidal period is represented by an arrow in Figure 4.7. Interesting observations per location are the following:

- At Frame 1, the residual discharge is eastward directed during every tidal cycle in the record. The magnitude of the eastward residual flow depends on the wind field; large residual flows are observed during strong winds from the west. During winds from the east, the residual discharge is more northeast directed. During relatively strong winds from the northwest, the residual discharge appears a bit more southward directed than on average. The red arrows indicate the successive tidal periods that cover the stormy period in the beginning of October, which led to a large setup at the ebb-tidal delta (see Figure 4.4). Winds from the southwest also lead to a large residual discharge at this location. During these wind conditions wave heights are generally not very high (see Figure 4.2), which seems to indicate the contribution of local wind shear stresses to residual flows.

- At Frame 3, the residual discharge is northward directed (export from the basin) during 68 of the 69 tidal periods in the record. This matches expectations, because Frame 3 was located in the inlet's channel and the tidal wave is partly progressive; water levels are generally lower during ebb flow and the channel thus has a larger contribution in the outward flow. The residual discharge was inward directed for only one of the tidal periods in the record, which was during the second windstorm in the field campaign. The residual outflow at Frame 3 was largest during strong winds from the west and southwest. Another interesting observation is that the residual outflow stayed relatively large for two tidal periods after the storm event on September 13$^{\text{th}}$. The tidal period that includes the storm's peak and the two successive tidal periods are indicated in Figure 4.7 by *s*, *s+1* and *s+2*, respectively. The tidal period before the storm peaked in wind speed is indicated by *s-1*. The arrows of these four periods are indicated in black.

- The direction of the residual discharge at Frame 4 is relatively constant in time, especially during calm winds. The magnitude of the residual discharge per tidal cycle increases with the wind speed from the west; during strong winds from the west, but also during strong winds from the northwest and from the southwest, the residual discharge is relatively large. Among these strong wind periods there is some variation in the direction of the residual current; during some periods it is a little more directed northeast, during other periods a little more east: The first windstorm (black arrows) belongs to the first class and the second windstorm (red arrows) to the second. The first windstorm's peak at September 13$^{\text{th}}$ induced a very large residual discharge in northeast direction (indicated by the large black arrow).

- At Frame 5 the residual discharge is in general smaller in magnitude than at Frame 1 and at Frame 4, and its direction is more variable, between northeast and southeast. The limited magnitude of the residual discharge might be related to the lower water depth than at Frame 4, but it might also indicate that a wave-induced current is less strong at this part of the ebb-tidal delta. The development of a wave-induced current might also explain why the residual discharge is directed either more northeast or more southeast during cycles with similarly strong winds from the west. The tidal periods with a residual discharge towards the southeast all belong to the stormy period around the second windstorm (indicated by red arrows). Also at this location, the residual current is still eastward directed during wind from the east.

The results presented in Figure 4.7 show that there is a strong correlation between wind conditions and the observed residual discharge at the ebb-tidal delta and in the inlet of Ameland Inlet system. Because of the correlation between wind and waves, however, it remains unknown whether the residual discharge is driven by wind shear stresses (i.e. wind-driven) or by breaking waves (i.e. wave-driven). Most likely the residual discharge is driven by a combination of both; if that is true then the interest is at unravelling the contribution of the two in the total residual flow.

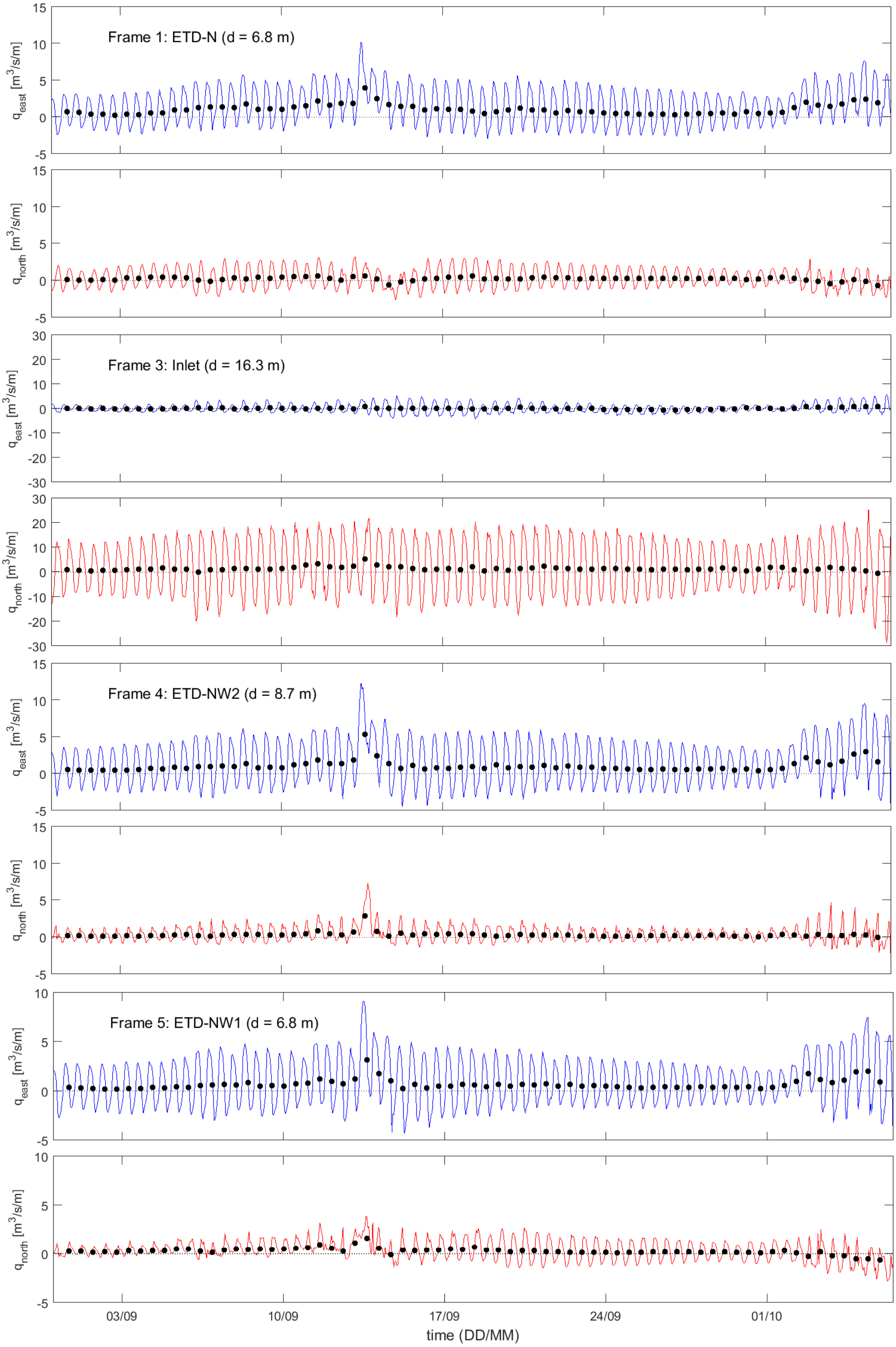

Figure 4.6: Time series of the discharge in east- and northward direction as measured at Frame 1 (top), Frame 3, Frame 4 and Frame 5 (bottom). Black dots represent the average discharge per tidal cycle. Magnitudes are given per unit width. Note: the vertical scale differs per location.

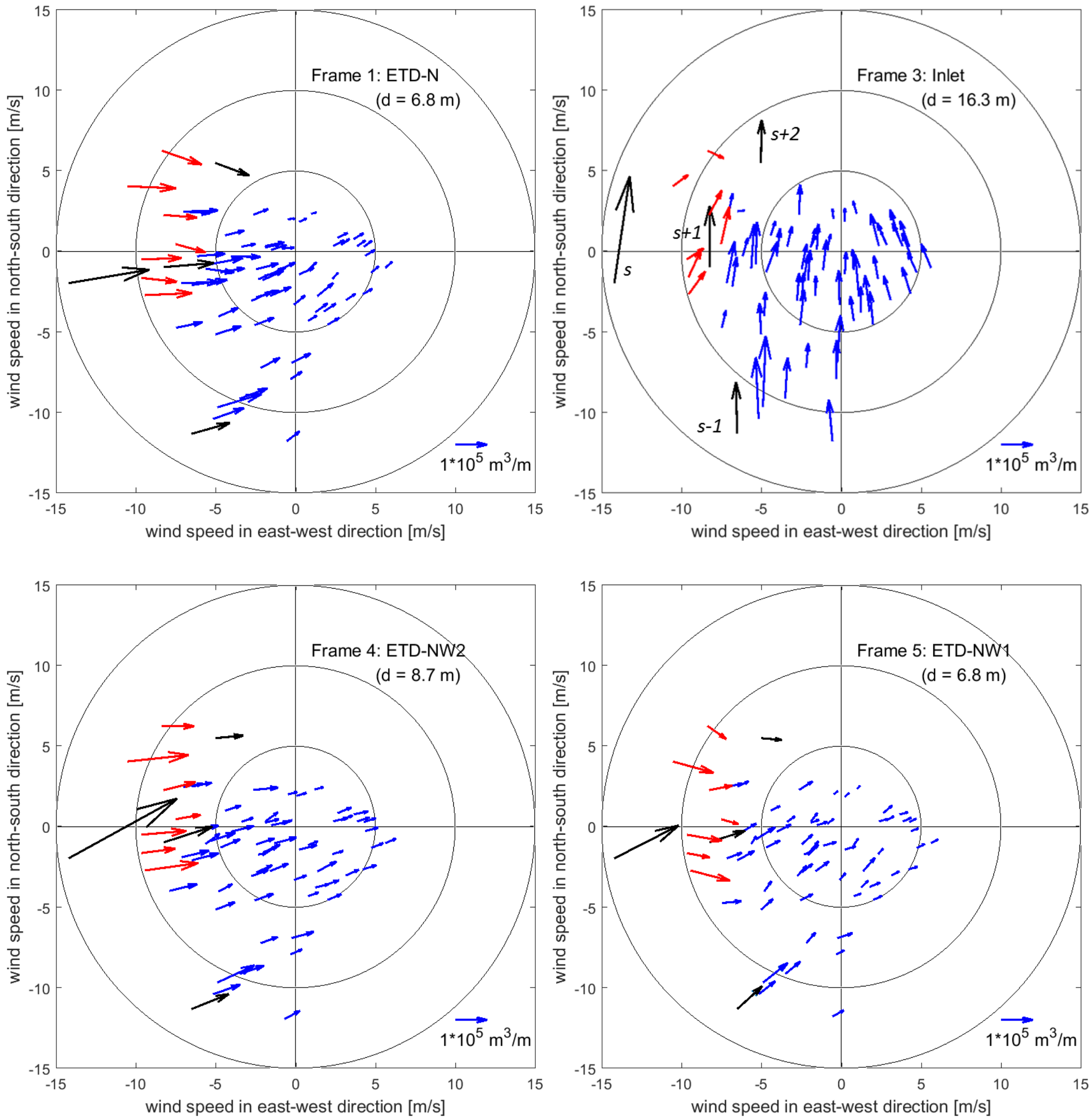

Figure 4.7: Residual discharge per tidal cycle in relation to the tide-averaged wind conditions. The arrows indicate the magnitude and direction of the residual discharge. The place in the figure where an arrow starts indicates the wind conditions. Black arrows indicate a few tidal periods around the first windstorm (mid September). Red arrows indicate the tidal periods around the second windstorm (begin October).

4.3.2. Responsible forcing mechanisms

The different model simulations enable different processes governing the flow through the domain. These simulations are used to reproduce the field observations of residual flows, as presented in Figures 4.8, 4.9 and 4.10 for the observation points at the ebb-tidal delta and for Figure 4.11 for the observation point in the inlet's channel. The four different simulations are presented in separate figures. Differences between the field observations and the model results are caused by measurement errors and the model performance, but more importantly by a schematisation of the bathymetry onto the model's grid resolution. The latter induces a difference in mean water depth between the observation point in the field and the related grid cell in the model domain. Appendix B elaborates further on the consequences of a schematised bathymetry for the residual flow at observation point Frame 3: Inlet.

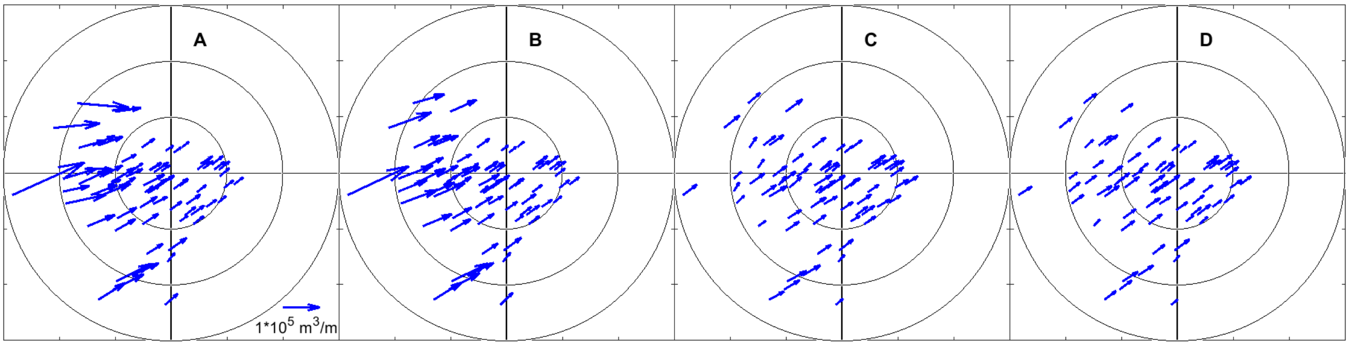

Figure 4.8: Residual discharge per tidal cycle in relation to the tide-averaged wind conditions, based on modelling results at observation point Frame 1: ETD-N. The mean water depth at this location in the model is 6.2 m. The four figures present four different simulations with different sets of forcing mechanisms enabled: **A**: Tide + Surge + Wind + Waves, **B**: Tide + Surge + Wind, **C**: Tide + Surge, **D**: Tide.

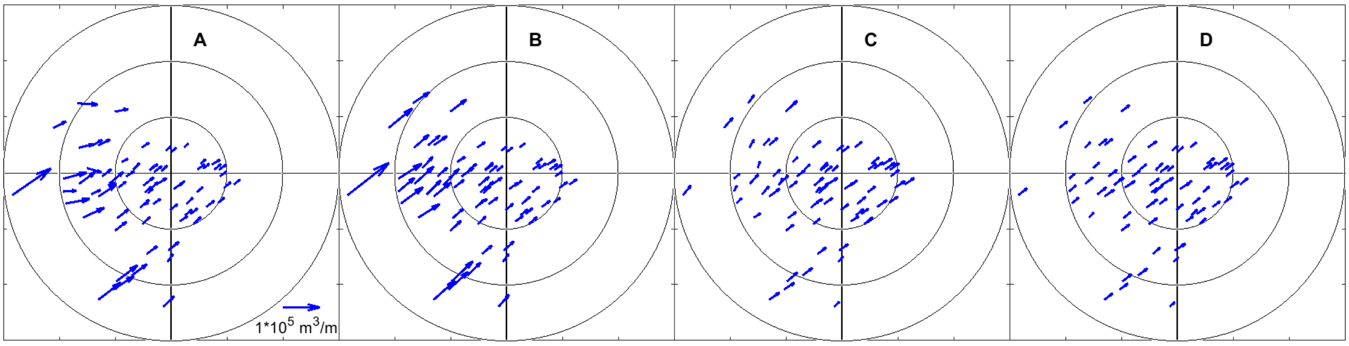

Figure 4.9: Residual discharge per tidal cycle in relation to the tide-averaged wind conditions, based on modelling results at observation point Frame 4: ETD-NW2. The mean water depth at this location in the model is 6.3 m. The four figures present four different simulations with different sets of forcing mechanisms enabled: **A**: Tide + Surge + Wind + Waves, **B**: Tide + Surge + Wind, **C**: Tide + Surge, **D**: Tide.

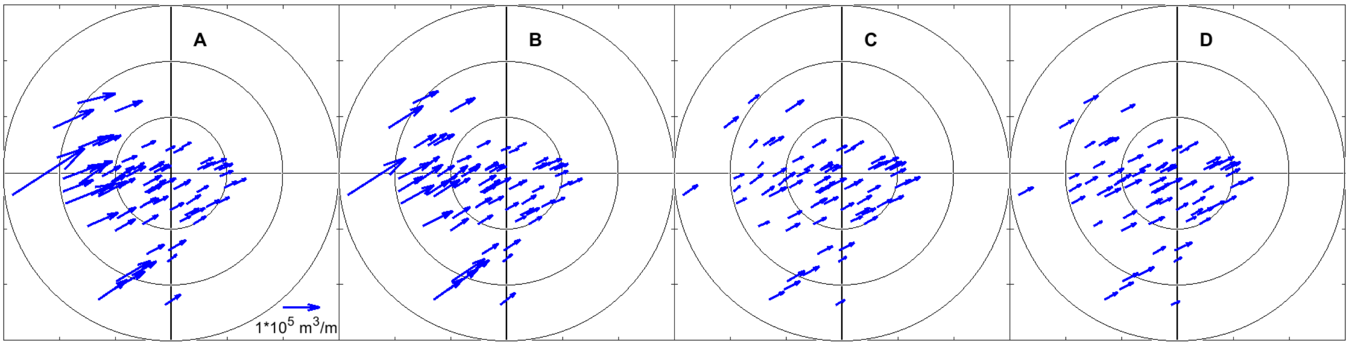

Figure 4.10: Residual discharge per tidal cycle in relation to the tide-averaged wind conditions, based on modelling results at observation point Frame 5: ETD-NW1. The mean water depth at this location in the model is 8.1 m. The four figures present four different simulations with different sets of forcing mechanisms enabled: **A**: Tide + Surge + Wind + Waves, **B**: Tide + Surge + Wind, **C**: Tide + Surge, **D**: Tide.

At observation points at the ebb-tidal delta (Figures 4.8, 4.9 and 4.10), wave-driven currents clearly affect the direction of the residual discharge. Without the development of a wave-driven current (**B** relative to **A**), the residual flow over the ebb-tidal delta was directed in northeast direction for every tidal period during the field campaign. Depending on the occurrence and magnitude of waves, the residual discharge can be directed more east-southeast. This is most clearly visible for tidal periods during wind conditions that led to relatively high waves (those periods are in the upper left quadrant of the figures, see also Figure 4.2).

In part **B** of the figures, the correlation between the residual discharge and the wind conditions is only due to local wind effects and surge at the model boundary. In part **C** the residual discharge is only driven by water level variations (tide + surge) at the model boundaries and in part **D** only by tidal water level variations. With only the tide as a forcing mechanism the residual discharge per tidal period was north-eastward directed at the ebb-tidal delta. Including surge at the model boundary induces a relatively small variation in the direction and the magnitude of the residual current among tidal periods. During the field campaign, wind-driven flows amplified the residual discharge in north-eastward direction up to four times (**B** relative to **C**). Following the series of figures presented here, it is especially the wind shear stress that amplifies the tide-induced residual discharge over the ebb-tidal delta.

Figure 4.11 presents a series of figures regarding the residual flow at the observation point in the inlet. Again, the residual flow changes in direction and magnitude due to wave-induced currents for high wave conditions only. Local wind conditions are most important for the variation in magnitude of the residual flow; the standard deviation of the magnitude of the residual flow per tidal period (σ) is $1.5{\cdot}10^4$ m^3/m for data from simulation **B** and $\sigma = 6.2{\cdot}10^3$ m^3/m for data from simulation **C**. The difference in magnitude due to local wind conditions is largest for winds from the west-southwest, which is expected to be induced by the wind dependent interconnectivity of tidal basins in the Wadden Sea. This is investigated further in Chapters 5 and 6. The variation in magnitude in part **C** of Figure 4.11 is due to intertidal storage in the basin, and therefore larger than in part **D** ($\sigma = 4.7{\cdot}10^3$ m^3/m).

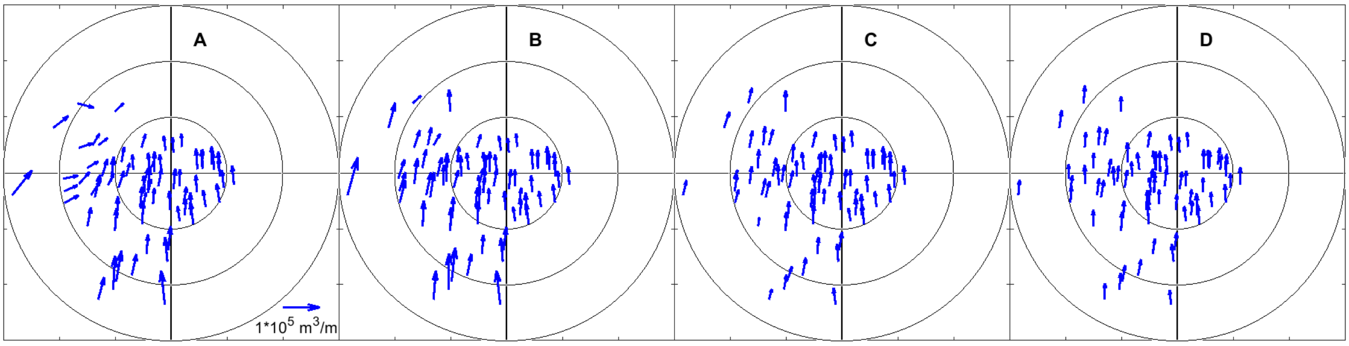

Figure 4.11: Residual discharge per tidal cycle in relation to the tide-averaged wind conditions, based on modelling results at observation point Frame 3: Inlet. The mean water depth at this location in the model is 11.8 m. The four figures present four different simulations with different sets of forcing mechanisms enabled: **A**: Tide + Surge + Wind + Waves, **B**: Tide + Surge + Wind, **C**: Tide + Surge, **D**: Tide.

The residual discharges according to different model simulations can also be considered relative to each other (i.e. **A** relative to **B**; **B** relative to **C**; **C** relative to **D**), which provides more quantitative insight in the governing processes. This is illustrated in Figures 4.12, 4.13 and 4.14 for the three observation points at the ebb-tidal delta and in Figure 4.15 for the observation point in the tidal inlet. The first plot in these figures (**A - B**) presents the residual discharge induced by waves, the second plot (**B - C**) presents the residual discharge induced by local wind shear stresses, the third plot (**C - D**) presents the residual discharge induced by surge at the boundary of the model domain, and the fourth plot (**D**) shows the residual discharge due to the tidal motion only. What has been discussed earlier in this section also follows from this series of figures. The tidal periods during which wave- and wind-driven currents significantly contribute to the residual discharge are, however, pointing out more clearly here.

4.4. Sediment transport model

In order to investigate the sediment transport capacity in response to the combined effect of waves and a residual current, the Soulsby - van Rijn equation for total load transport (suspended load + bedload) is used to determine the sediment transport potential for observed hydrodynamic events (Soulsby, 1997). For this purpose, the depth-averaged velocity and the near-bed velocity (i.e. average of the first two measured values from the bed) are determined for every time step. Per burst of half an hour the mean depth-averaged velocity is used as a measure for the current and the root-mean-squared near-bed velocity is used as a measure for the wave orbital velocities. The total sediment load per unit width [$m^3/s/m$] is then defined as:

$$\mathbf{q_s} = A_S \bar{\mathbf{U}} \left[\left(|\bar{U}|^2 + \frac{0.018}{C_D} U_{rms}^2 \right)^{1/2} - \bar{U}_{cr} \right]^{2.4}, \tag{4.1}$$

where $\bar{\mathbf{U}}$ is the depth-averaged horizontal current velocity, U_{rms} is the root-mean-square wave orbital velocity, C_D is the drag coefficient due to a current only and $\bar{U}_{cr}$ is the threshold current velocity for a given grain size. The characteristic grain diameters are assumed as $D_{50} = 200$ μm and $D_{90} = 1.5$ D_{50}.

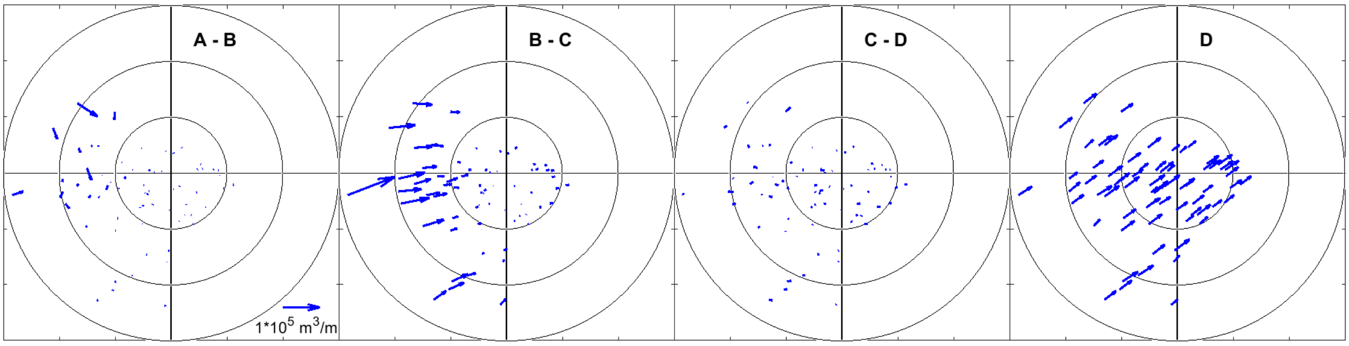

Figure 4.12: Contribution of each of the forcing mechanisms to residual discharge at observation point Frame 1: ETD-N, by considering the differences between plots in Figure 4.8. **A**: Tide + Surge + Wind + Waves, **B**: Tide + Surge + Wind, **C**: Tide + Surge, **D**: Tide.

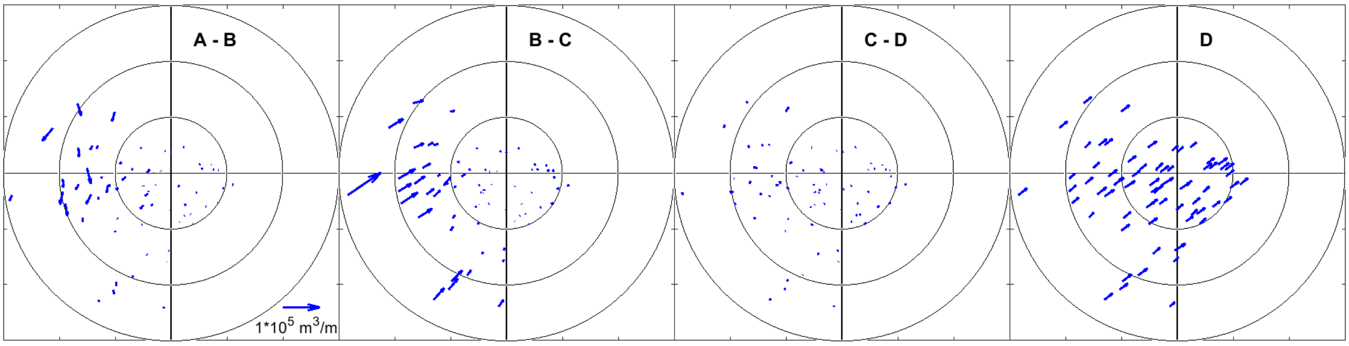

Figure 4.13: Contribution of each of the forcing mechanisms to residual discharge at observation point Frame 4: ETD-NW2, by considering the differences between plots in Figure 4.9. **A**: Tide + Surge + Wind + Waves, **B**: Tide + Surge + Wind, **C**: Tide + Surge, **D**: Tide.

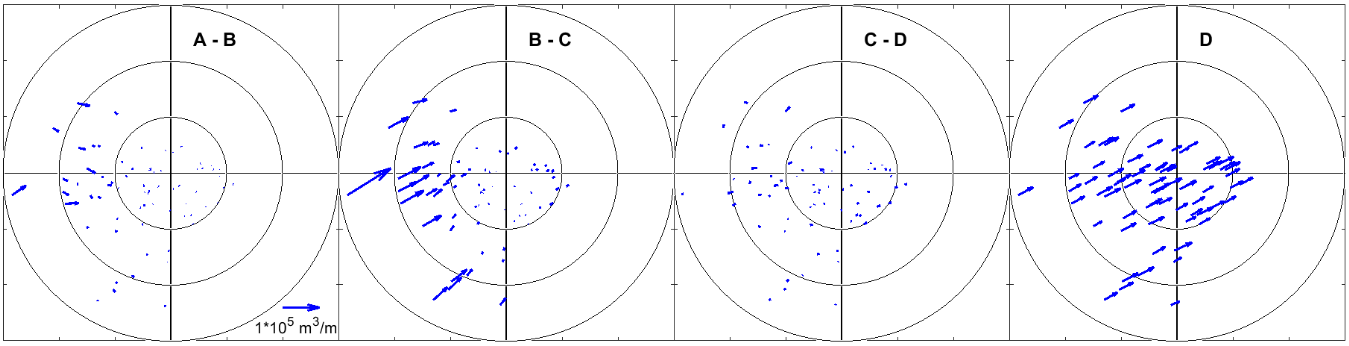

Figure 4.14: Contribution of each of the forcing mechanisms to residual discharge at observation point Frame 5: ETD-NW1, by considering the differences between plots in Figure 4.10. **A**: Tide + Surge + Wind + Waves, **B**: Tide + Surge + Wind, **C**: Tide + Surge, **D**: Tide.

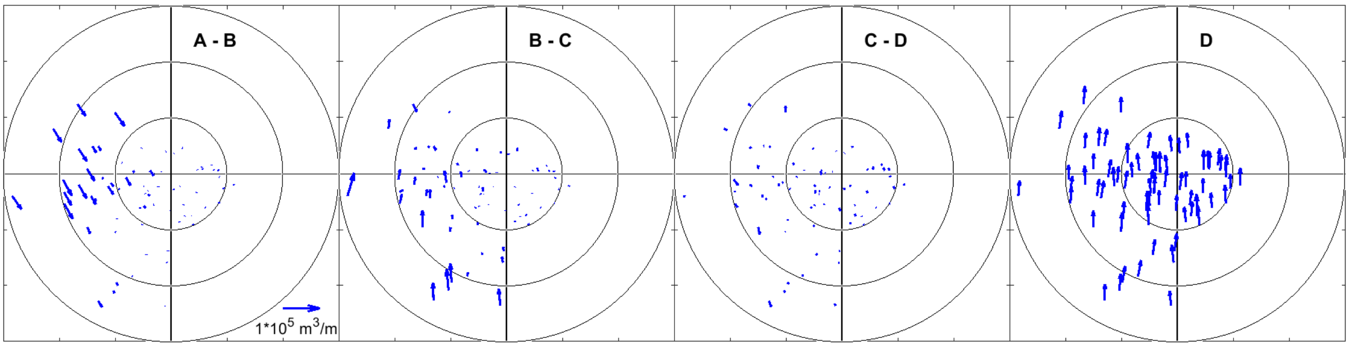

Figure 4.15: Contribution of each of the forcing mechanisms to residual discharge at observation point Frame 3: Inlet, by considering the differences between plots in Figure 4.11. **A**: Tide + Surge + Wind + Waves, **B**: Tide + Surge + Wind, **C**: Tide + Surge, **D**: Tide.

In Equation 4.1 the effect of a bed slope is neglected and A_S is a calibration coefficient (Soulsby, 1997). The availability of sediment is, for simplicity, not taken into account. Equation 4.1 is not the most advanced sediment transport formula known in literature, since it does not include the direction of wave propagation nor wave asymmetries (i.e. without a current there is no transport). The equation is - however - sufficiently accurate for the purpose of this section, namely to investigate the relative importance of different events in the residual sediment transport.

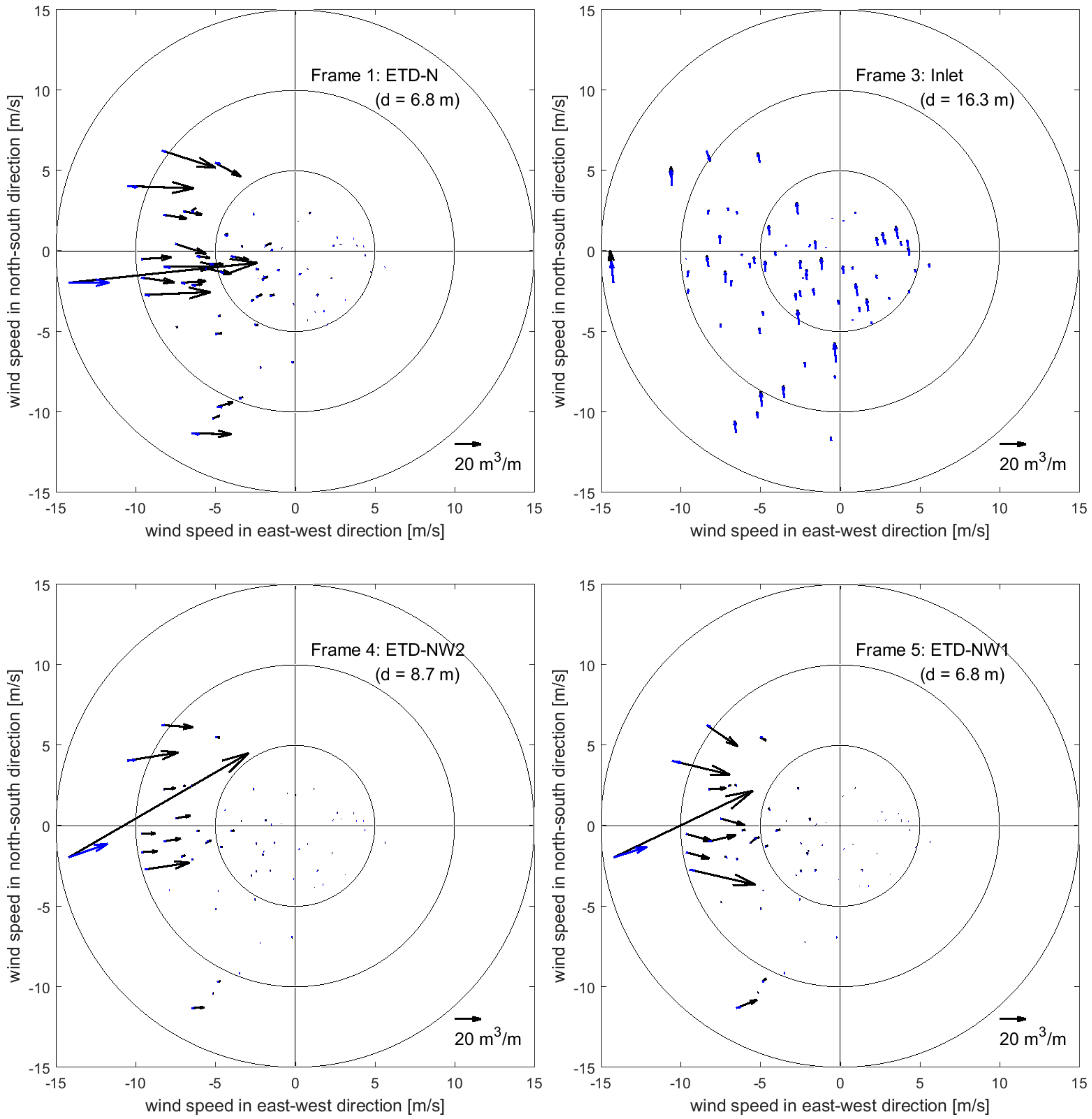

Figure 4.16: Residual sediment transport potential per tidal period in relation to the average wind conditions over that period. Values are calculated based on measured hydrodynamic conditions according to Equation 4.1. The arrows indicate the magnitude and direction of the computed residual sediment transport. The place in the figure where an arrow starts indicates the tide-averaged wind conditions. Black arrows represent the sediment transport potential including the stirring effect of waves, blue arrows represent the sediment transport potential by the current only.

The correlation between wind speed and wave height has been addressed before (see Section 4.1). It might therefore be no surprise that the combination of large residual flows with high waves during strong winds from the west/northwest has a large sediment transport potential. This is illustrated in Figure 4.16. These plots are set-up similarly as in Figure 4.7. Figure 4.16 shows the sediment transport capacity per tidal cycle both with the inclusion of the stirring effect of waves (black arrows) and without the inclusion of this effect (blue arrows), both based on Equation 4.1. A difference in direction between the black and the blue arrow indicates that wave energy was larger during a specific part of the tidal cycle (i.e. ebb or flood).

At the ebb-tidal delta, the combination of a residual flow and the stirring effect of waves make the residual sediment transport during tidal periods with strong winds from the west dominant over calmer periods. At the three observation points at the ebb-tidal delta, the sediment transport is particularly high because of the stirring effect of waves, which is presented by much larger black arrows than blue arrows in Figure 4.16. At Frame 3, in the inlet (d = 16.3 m), the orbital velocity of waves near the bottom is much smaller than at the shallower ebb-tidal delta, and therefore the stirring of waves is of less importance in the sediment transport capacity; only during a few periods the black arrow is larger than the blue arrow in Figure 4.16. Whereas the residual sediment transport during calm wind periods seems almost negligible at the ebb-tidal delta, these periods do have a significant contribution at Frame 3.

The dominant contribution of some tidal events over others in the cumulative sediment transport over the ebb-tidal delta and the correlation of these dominant events with the wind speed are illustrated in Figure 4.17. For the cumulative sediment transport at the ebb-tidal delta over the duration of the field campaign, it appears that a few tidal cycles (≈ 20%) during which the wind speed was highest contribute to the vast majority (≈ 80%) of the cumulative sediment transport. Among these tidal cycles with high wind speeds, there are still a few periods that hardly contribute. This can be explained by the wind direction, since the wind during these tidal cycles was high, but coming from a direction that does not lead to large waves at the ebb-tidal delta (e.g. southwest). At Frame 3, the contribution of each tidal period to the cumulative sediment transport is more equal and less dependent on the wind speed.

Generally speaking, residual sediment transport at observation points at the ebb-tidal delta is for a large part driven by highly energetic wind- and wave conditions. In the tidal inlet's channel, the contribution of calm periods in the residual sediment transport is more significant than at the ebb-tidal delta. The transport through the inlet does not necessarily increase for periods with higher wind speeds.

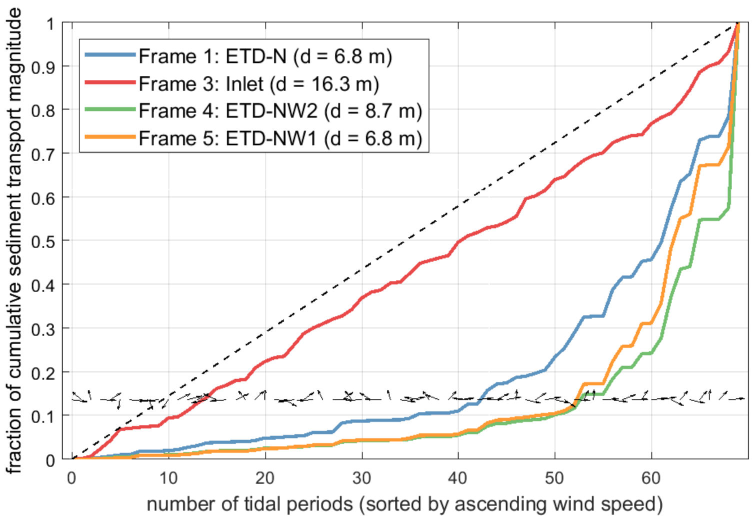

Figure 4.17: Fraction of the cumulative sediment transport magnitude (computed, vertical axis) during a certain number of tides that are ordered by ascending wind speed (horizontal axis). The small arrows indicate the wind direction as measured at KNMI station Hoorn Terschelling. The dashed line indicates the hypothetical case of equal residual sediment transport for every tidal period.

Key points

- The range between set-up and set-down at the ebb-tidal delta and in Ameland basin is around 2.5 m. The surge level mainly depends on the wind conditions in relation to the orientation of the inlet system.
- Field observations show that the residual discharge at the ebb-tidal delta is directed northeast. A variation in the magnitude of the residual discharge correlates with wind conditions. Wave-induced flows change both the direction and the magnitude of the residual discharge during high wave conditions. Large wind shear stresses aligned with the prevailing wind direction amplify the residual discharge in northeast direction.
- At the observation point in the inlet the residual flow was directed outward. Although measured wave heights are low at this location, wave-driven flows affect the direction and magnitude of the residual flow in a similar manner as at the ebb-tidal delta. Winds from the southwestern quadrant contribute to an additional outflow at this point in the inlet.
- The cumulative sediment transport at observations points at the ebb-tidal delta is, at least for the duration of the field campaign, dominated by a few periods with highly energetic waves and large residual flows.

5
Watersheds
Leaking borders

This chapter discusses the flow over the watersheds of Terschelling and Ameland in order to investigate the exchange with neighbouring basins. These watersheds are also called Terschellinger Wad and Pinke Wad, respectively. The first part of this chapter relates to the analysis of field observations. The second part includes results from numerical modelling to quantify the residual flows over the full cross-section and to extend the analysis in time. The last part of this chapter discusses the capacity of the flow over the watersheds to transport sediment, based on modelling results.

5.1. Field observations

Three Aquadopp instruments were placed at each of the watersheds of Terschelling and Ameland for approximately one month (see Figure 2.2). For five of the six instruments the low water level did not always exceed the level of the instrument's pressure head, leading to gaps in the record. Figure 5.1 shows time series of the water depth for one instrument at each of the watersheds. The maximum water depth at the six locations rises just over 3 m. The difference between high water levels varies with approximately 1.5 m during the field campaign. Figure 5.1 shows time series of the instantaneous discharge in two directions for one instrument at each of the watersheds. At gaps in the record, the water level did not exceed the blanking distance of the instrument; therefore no flow velocities were measured at these periods. Figure 5.1 shows much variation in the magnitude of the instantaneous discharge at the observation points. A large peak in the discharge occurred during the storm event at September 13th.

Regarding the exchange processes at the borders of Ameland Inlet system, particularly the residual flow is of interest. Earlier work, based on numerical modelling, has shown that the residual flow over the watershed of Terschelling varies with the wind conditions (Duran-Matute et al., 2016). Holding on to that finding, the residual discharge per tidal period is presented in relation to the tide-averaged wind conditions for each of the six instruments in Figure 5.3. Flow towards the east of the watershed is defined positive. The values presented in Figure 5.3 are biased by missing observations during some low water conditions. It is expected, however, that these low water conditions have only a minor contribution to the subtidal discharge.

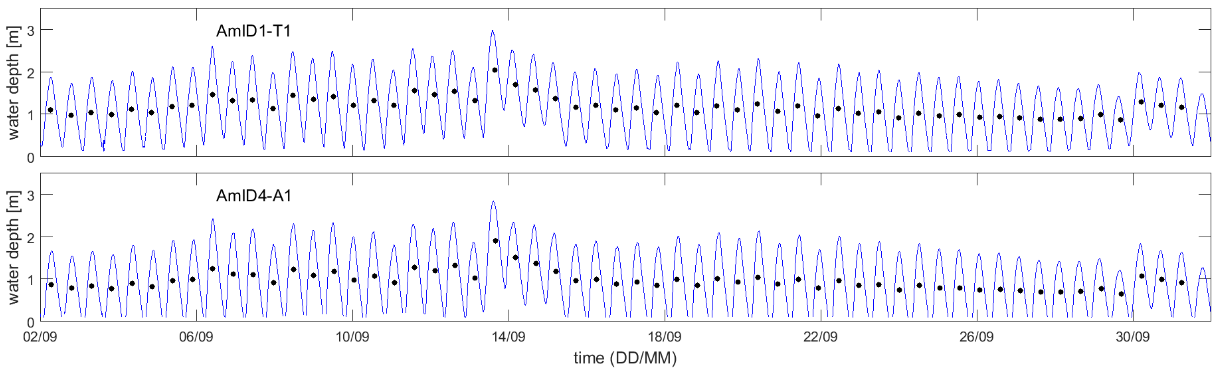

Figure 5.1: Time series of the local water depth as measured at observation points at the watersheds behind Terschelling (AmID1-T1) and behind Ameland (AmID4-A1). Black dots indicate tidal averaged water depths.

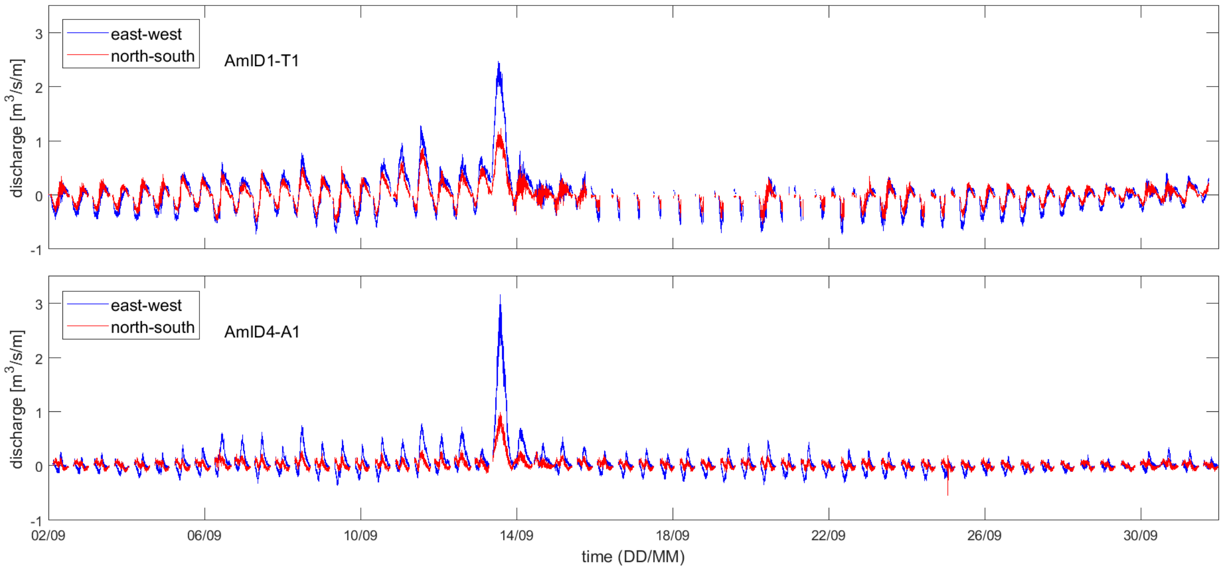

Figure 5.2: Time series of the instantaneous discharge in east- and northward direction per unit width as measured at observation points at the watersheds behind Terschelling (AmID1-T1) and behind Ameland (AmID4-A1). Gaps in the record indicate periods during which the water level did not exceed the blanking distance of the instrument.

Figure 5.3 indeed shows the variation with the wind conditions in the field measurements. The most interesting observations regarding the instruments at Terschellinger Wad are the following:

- At AmID1-T1, the residual discharge is generally westward directed during calm conditions, independent of the wind direction. During tidal periods with mild winds from the southwest, the residual discharge is eastward directed and the eastward discharge increases with increasing wind speeds.
- At AmID2-T2 the subtidal discharge is lower in magnitude than at AmID1-T1. The malfunctioning of the AmID2-T2 instrument in the second half of the field campaign makes that not many tidal periods are included in the record. During calm wind conditions the residual discharge at AmID2-T2 is westward directed.
- The discharge at AmID3-T3 is mostly westward directed during calm wind conditions, although some tidal periods in the record (i.e. 7/57) lead to an eastward residual. At this location the residual discharge is again lower in magnitude, likely also because the average water depth is smaller than at AmID1-T1 and at AmID2-T2.

Generally, significant residual discharges to the east of Terschellinger Wad are observed during mild winds from the west (between south and northwest). The tidal period that includes the storm event on September 13th is included in Figure 5.3 as the darkest red dot (i.e. high wind speed), indicating a peak in the eastward discharge. Apparently, this event induced a very large residual discharge over the watershed, considered relative to the residual discharge over other tidal periods during the field campaign.

Some of the findings for Terschellinger Wad are also valid for Pinke Wad. The largest eastward flows are observed coinciding with mild to strong winds from the west. Unfortunately, no periods of strong wind from the east were observed during the field campaign. Again the direction of the residual discharge during calm wind conditions varies per location, which is believed to be caused by the position of the instruments in the system (e.g. in a channel or at a tidal flat). Figure 5.3 indicates that the residual discharge over the watershed behind Ameland was larger during mild winds from the west than during strong winds from the southwest, something which is not true for the watershed behind Terschelling. Based on the information presented here, it is expected that the flow over the watershed behind Terschelling is more sensitive to winds from the southwest, whereas the flow over the watershed behind Ameland is more sensitive to winds from the west-northwest. If this is true, it can be explained by the shape of the Wadden Sea and hence the orientation of the watersheds; towards the east, the Dutch Wadden Sea is orientated more east-west than northeast-southwest, as it is in the western part.

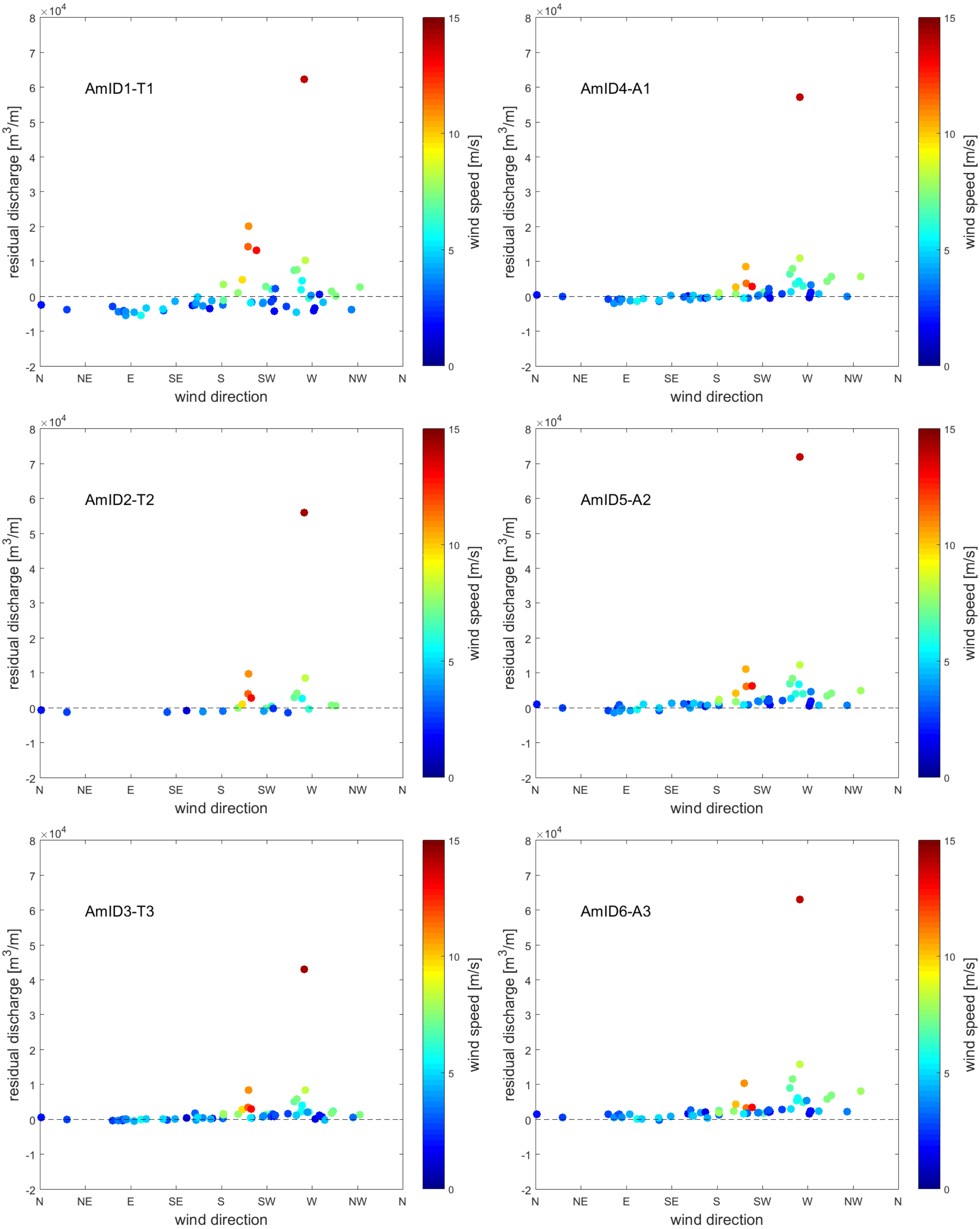

Figure 5.3: Residual discharge per unit width per tidal period as measured by Aquadopp instruments at the watersheds behind Terschelling (left three scatterplots) and Ameland (right three scatterplots). The magnitude of the residual discharge per tidal period is the net volume transport in the principal direction. Transport is defined positive in eastward direction. The locations are indicated in Figure 2.2.

The field observations are the evidence for the exchange with neighbouring basins as a function of the wind conditions. These observations are, however, limited to six observation points in the system for a duration of approximately one month. The modelling results are used in the next section to extend the analysis of flow over the watersheds in time, and to integrate the magnitude of the residual discharge over the width of the watershed.

5.2. Numerical modelling

Cross-sections at the watersheds behind Terschelling and Ameland are defined in the Delft3D model along grid lines, as illustrated in Figure 5.4. Output time series have a resolution of $\Delta t = 10$ min. As in the discussion of field observations, flow towards the east of the watershed is considered positive.

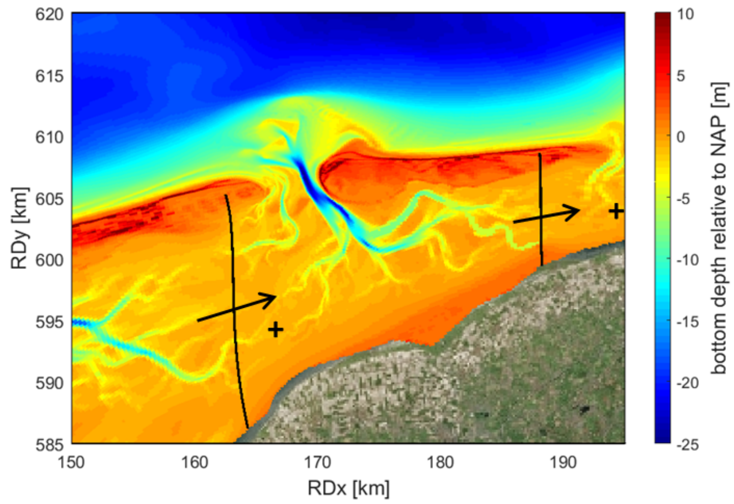

Figure 5.4: Locations of cross-sections in the model domain where flow over the watersheds is considered. The cross-sections are aligned with grid lines, approximately at the positions of the watersheds behind Terschelling (left) and Ameland (right).

As a comparison between the field observations and the modelling results, Figure 5.5 first shows for the two watersheds the residual discharge per tidal period integrated over the cross-section in relation to the acting wind forcing. Data points are limited to the extent of the field campaign. One is referred to Figure 5.3 for a similar investigation at the observation points in the field. The results in Figure 5.5 are computed by integration over the full width of the watershed, hence the magnitude is orders of magnitude larger than in Figure 5.3. The similar dependence of the residual discharge on the wind conditions in the field observations and in the modelling results gives confidence in the capabilities of the numerical model to simulate flows over the watersheds correctly.

5.2.1. Quantitative analysis

According to the modelling results, the residual discharge over the Terschelling watershed in 2017 is $13.8 \cdot 10^9$ m^3 in eastward direction. The residual discharge over the Ameland watershed in 2017 is $6.9 \cdot 10^9$ m^3 in eastward direction. The difference between the two is about sixteen times the mean tidal prism through Ameland Inlet. Figure 5.6 illustrates the course of the residual discharge over the two watersheds in time. The residual discharge over the Ameland watershed is smaller, but also less varying in time. The course of the residual discharge is seasonally dependent. At the end of summer the cumulative discharge over the two watersheds is approximately equal in magnitude. During the winter months at the end of the year the difference in residual discharge starts to become significant; the residual flow over the Terschelling watershed is much larger than the residual flow over the Ameland watershed.

In Figure 5.7, the residual discharges over the two watersheds are presented per tidal period. Pearson's linear correlation coefficient between the subtidal flow over the two watersheds is $\rho = 0.91$. The best linear fit through the data points in a least-squares sense has a slope of 0.26, which implies the residual flow per tidal period over the Ameland watershed is 26% of the residual flow over the Terschelling watershed. Given the tidal prism through Ameland Inlet is approximately $4.2 \cdot 10^8$ m^3, the residual discharge over the watersheds must have a significant effect on the residual flow through Ameland Inlet. This will be investigated further in Chapter 6.

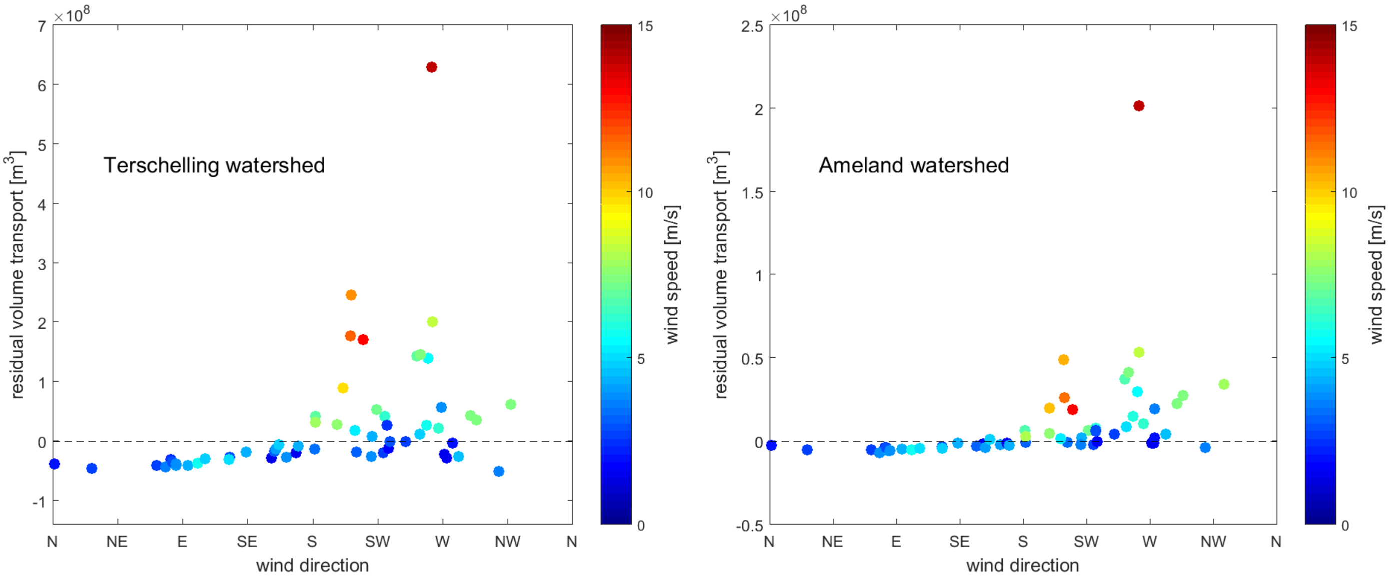

Figure 5.5: Modelling results of the residual discharge over the watersheds of Terschelling (left) and Ameland (right) per tidal period in relation to the tide-averaged wind conditions for the duration of the field campaign. Note the scales of the vertical axes differ to improve visibility. A tidal period is here defined as in the discussion of field observations, so starting at low water at the watershed.

It is already visible in Figure 5.4 that the Wadden Sea becomes smaller towards the east and the cross-section at the Ameland watershed is thus smaller than at the Terschelling watershed. The ratio between the conveyance capacity of the two watersheds at mean water level conditions is approximately 0.33, following a Chézy based approach;

$$K = C d^{3/2} B, \tag{5.1}$$

where K is the conveyance capacity [m^3/s], C is the Chézy coefficient, d is the water depth and B is the width of the cross section. The Chézy coefficient was assumed equal for the two cross sections. The difference in conveyance capacity between the watersheds largely explains the different magnitudes of the residual flows, also because the magnitude of the residual flow per unit width was similar in field observations at the two watersheds.

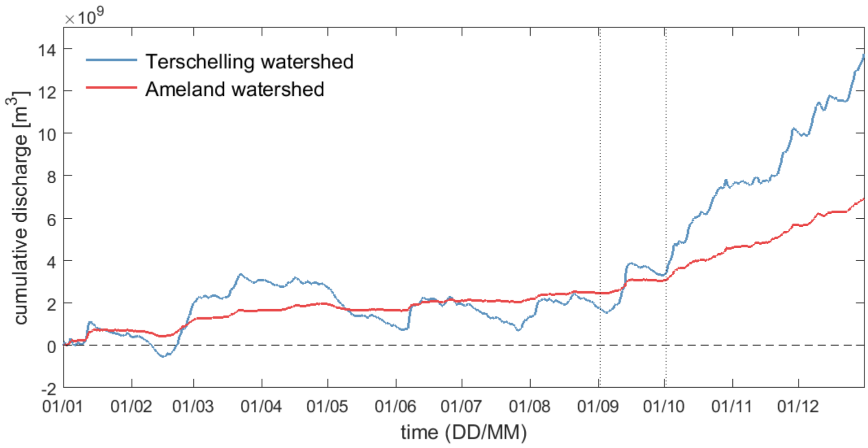

Figure 5.6: Course of the residual discharge over the watersheds of Terschelling and Ameland in 2017. The vertical dotted lines indicate the timespan of field observations. Flow towards the east of the watersheds is considered positive.

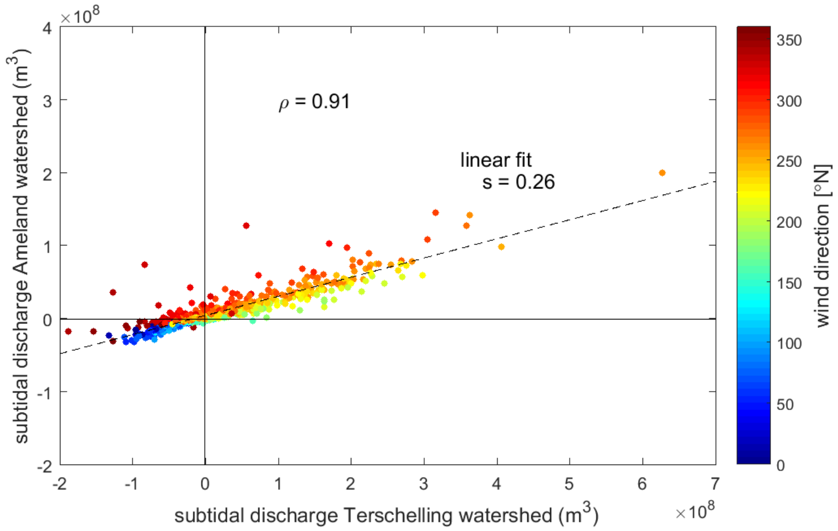

Figure 5.7: Scatterplot of the residual discharge per tidal period over the Terschelling watershed and over the Ameland watershed. ρ is the linear correlation coefficient of the data and the dashed line shows the best linear fit to the data in a least-squares sense (s is the slope of the line). The colour represents the tide-averaged wind direction.

5.2.2. Responsible forcing mechanisms

The modelling results are discussed in relation to the acting wind forcing in this section and the results of simulations with different sets of forcing mechanisms are presented.

Figure 5.8 presents the residual discharge over the watersheds per tidal period in 2017, in relation to the tide-averaged wind conditions. The results for the Terschelling watershed convey the same message as included in Duran-Matute et al. (2016), namely the residual flow over the watershed is largest for the two preferential wind directions west-southwest and north-northeast. The magnitude of residual flows over the Terschelling watershed are similar as found by Duran-Matute et al. (2016). Based on the data points in Figure 5.8, the preferential wind directions for flow over the Ameland watershed are directed west-northwest and east-northeast. This was already suggested in the discussion of field observations; the inclusion of more data points in the modelling results approves this suggestion. This can also be seen in Figure 5.7, since the ratio between the subtidal discharges over the Ameland watershed and over the Terschelling watershed is higher for winds from the northwestern quadrant than for winds from the south-western quadrant.

To further underline the dominant contribution of wind shear stresses for flow over the watersheds, Figure 5.9 shows the course of the residual discharge over the watersheds of Terschelling and Ameland in 2017 for the four different model simulations. Wave effects induce only minor modifications to the residual discharge at these shallow areas. Without the effect of wind shear stresses the yearly residual flow even reverses towards the west. The effect of surge at the model boundaries in Figure 5.9 is biased by the fact that the dominant driving mechanism was already disabled in simulation **C**, such that (non-linear) interactions between wind shear stresses and surge are not unravelled in these results. Surge levels at the watersheds, either locally generated or enforced at the model boundaries, are still expected to increase the conveyance capacity for flow over the watersheds and thus the residual flow. Figure 5.10 indicates this by presenting the residual discharge in relation to the maximum water level per tidal period. The variation in maximum water level includes surge levels, but also tidal variations (e.g. spring-neap variations and daily inequalities). Although not clearly included in Figure 5.9, Figure 5.10 suggests that the surge level positively correlates to the residual discharge over the watersheds and thus to the interconnectivity of basins.

5.2.3. Conveyance at shallow areas

The residual discharge over the watersheds of Terschelling and Ameland indicates the development of a wind-driven current through the Wadden Sea. Here, the aim is to further investigate the trajectory of this current. The main question is if the shallow areas convey much of the flow, or that the so-called Wadden Sea current is more concentrated in the tidal channels. The flow over a cross-section in the Wadden sea is therefore considered in two sections. Figure 5.11 shows the location of this cross-section in the model domain and the bathymetry along the cross-section. The cross-section is split into two sections, named A1 and A2. A1 mainly consists of a shallow (intertidal) area and A2 crosses the deeper channels in the Wadden Sea. The conveyance capacity of section A1 (see Equation 5.1) for mean water level conditions is around 25 times smaller than the conveyance capacity of section A2.

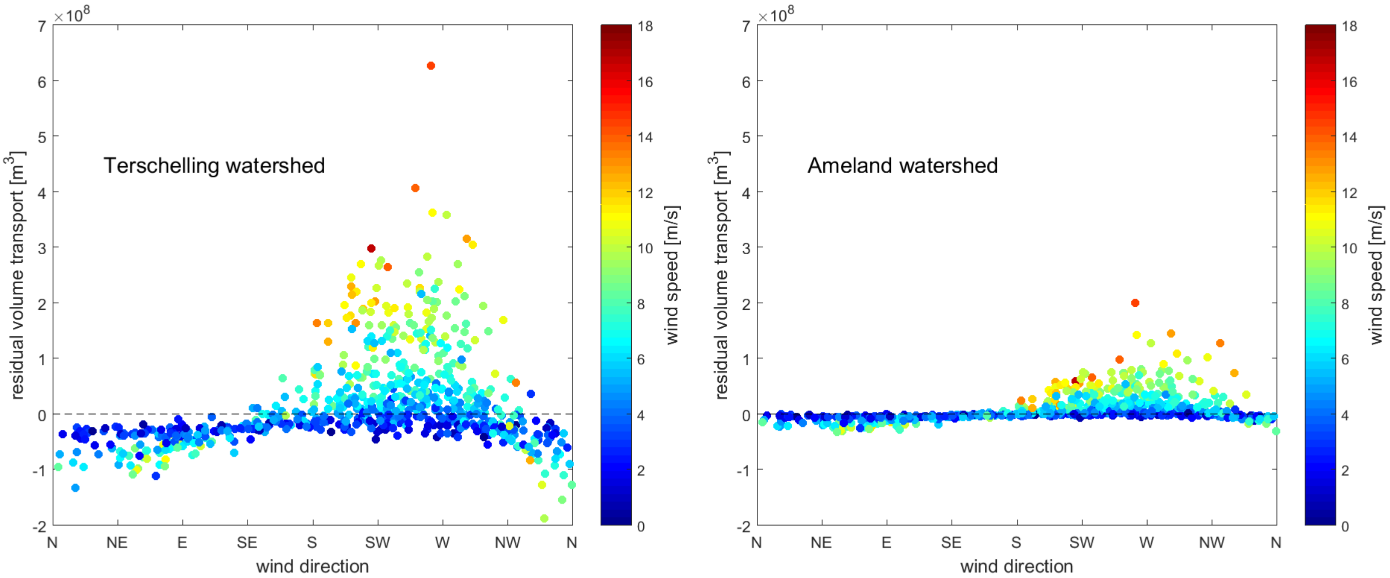

Figure 5.8: Scatterplot of the residual discharge over the watersheds of Terschelling (left) and Ameland (right) per tidal period in 2017 in relation to the tide-averaged wind conditions. Data is obtained from modelling results. A tidal period is for this figure defined to start at flow reversal from ebb to flood in Ameland Inlet (Frame 3: Inlet).

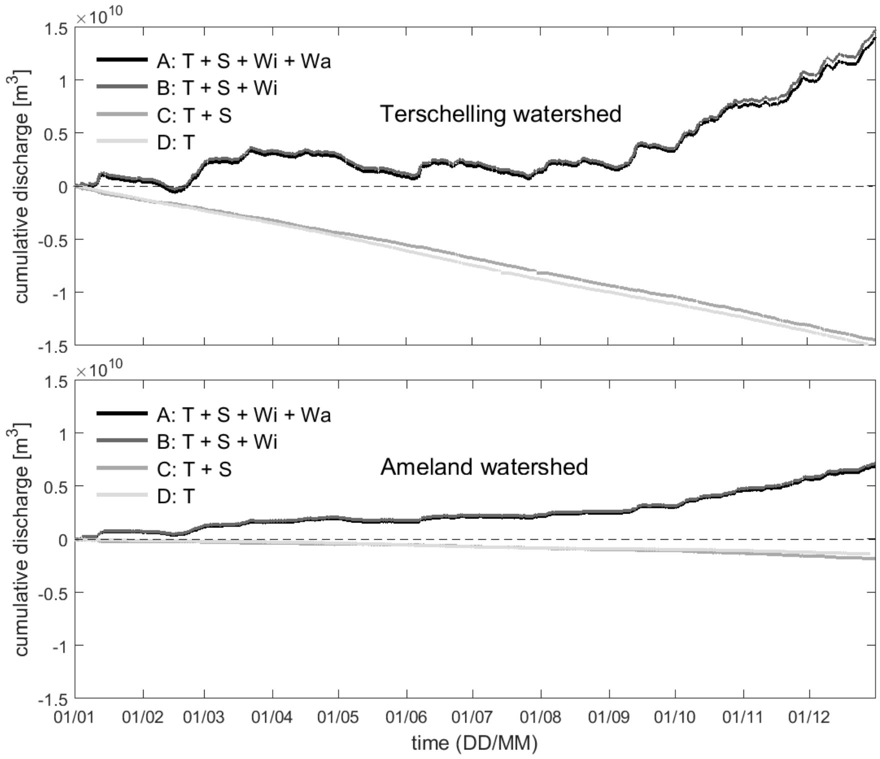

Figure 5.9: Course of the cumulative discharge over the watersheds of Terschelling and Ameland in 2017 for four model simulations with different sets of forcing mechanisms enabled. The results for simulation **A** are also included in Figure 5.6.

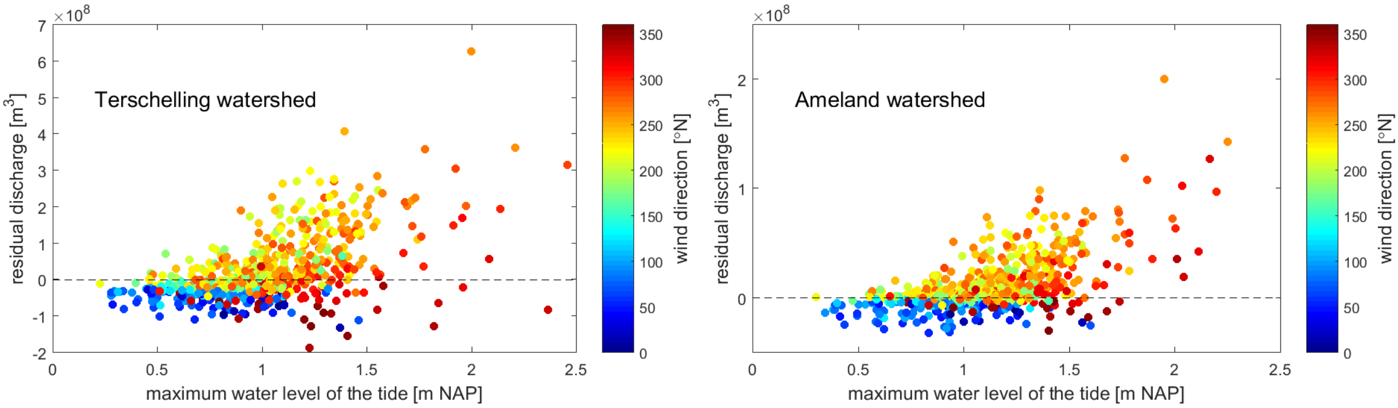

Figure 5.10: Residual discharge over the watersheds of Terschelling (left) and Ameland (right) per tidal period in 2017 in relation to the maximum water level. Colours indicate the average wind direction. Note the scales of the vertical axes differ to improve visibility..

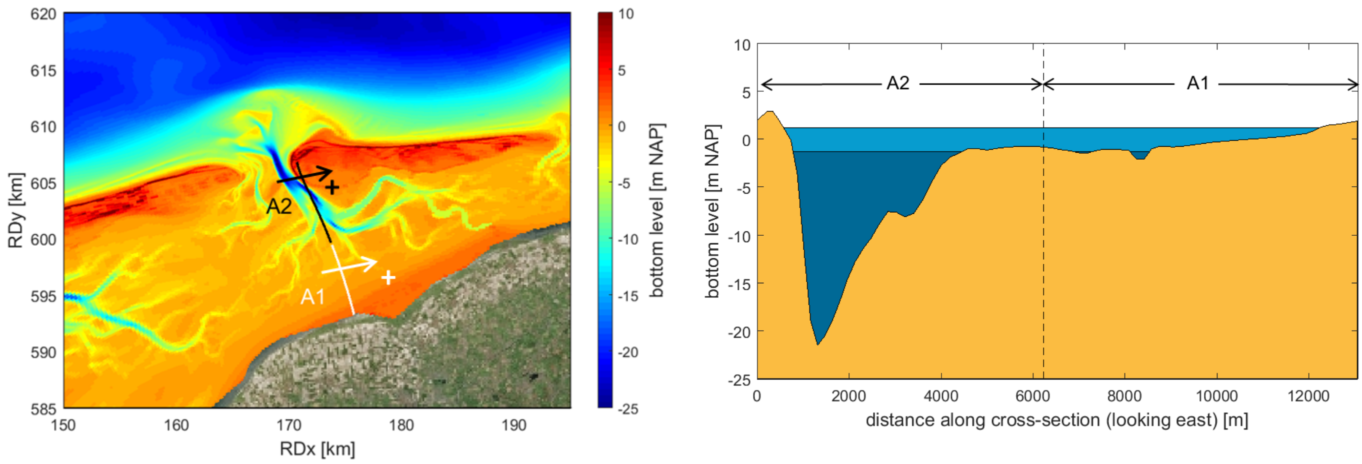

Figure 5.11: Locations and orientation of cross-sections A1 and A2 in the Wadden Sea (left) and the model bathymetry along the cross-sections, looking towards the east (right). Flow towards the east is considered positive.

Figure 5.12 shows per tidal period the residual discharge and the cumulative discharge towards the east and towards the west through section A1, in relation to the tide-averaged wind conditions. Figure 5.13 relates to section A2. For section A1 (i.e. the shallow section) the variation of the residual discharge with the wind conditions is similar to what was observed at the watersheds. During calm wind conditions a return flow makes residual flows over this section directed towards the west. For strong winds towards the west, there is hardly any tidal flow towards the east. For strong winds towards the east, the discharge is towards the east for entire tidal periods. The residual discharge through section A2 is generally directed towards the east during calm wind conditions. There is more variation in the magnitude of the residual discharge through section A2 than can be explained based on the wind conditions only. If winds from the preferential directions get stronger, the residual discharge increases.

The shallow part (A1) is more clearly governed by the wind conditions than the deeper section (A2), even such that the discharge was only in one direction for several tidal periods. Remarkable is that the residual discharge over the shallow section can be as large as the residual discharge over the deeper section, although the conveyance capacity is much smaller. Apparently, the shallow parts are at least as important as the deeper parts for the residual discharge over a full cross-section. The wind shear stress has a larger effect on the depth-averaged flow at shallow areas, and shallow areas thus are of importance for the conveyance of residual flows towards the next watershed.

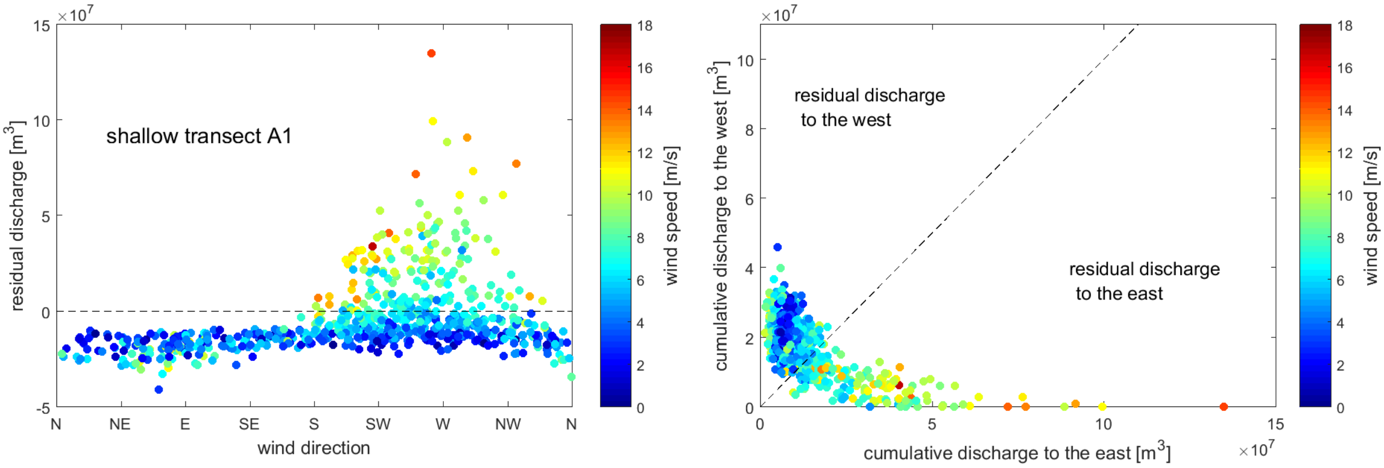

Figure 5.12: Residual discharge per tidal period through section A1 in relation to the tide-averaged wind conditions (left) and the cumulative discharge towards the two sides of the section (right). The dashed lines separate residuals to the west from residuals to the east.

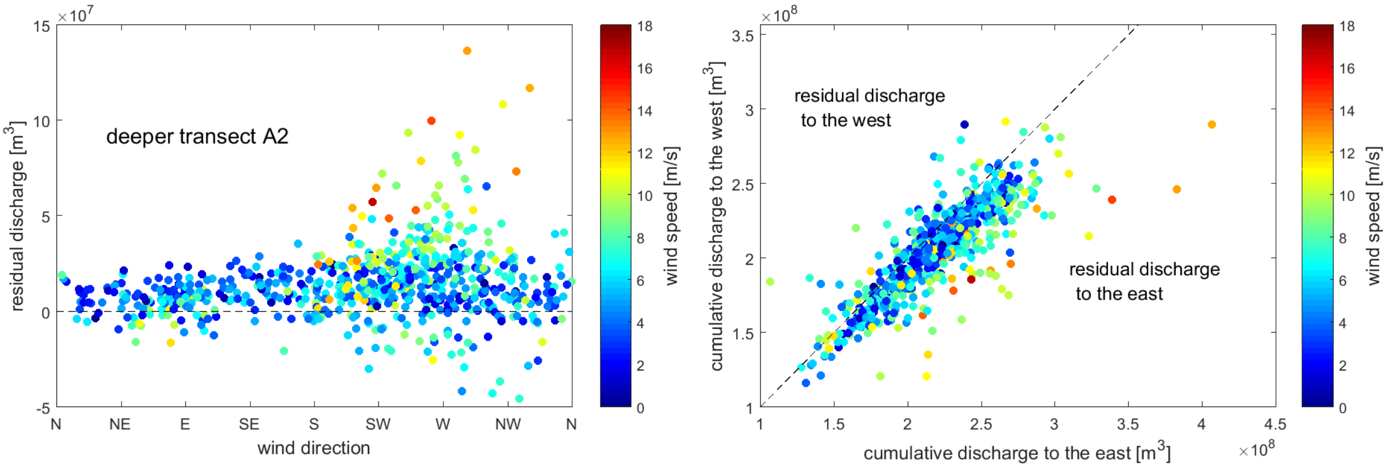

Figure 5.13: Residual discharge per tidal period through section A2 in relation to the tide-averaged wind conditions (left) and the cumulative discharge towards the two sides of the section (right). The dashed lines separate residuals to the west from residuals to the east.

5.3. Sediment transport capacity

Based on the modelling results, the sediment transport capacity of the flow over the watersheds can be investigated. The Delft3D model only includes one sand fraction and the results are therefore not necessarily representative for the true volume exchange with neighbouring basins. These results - however - provide much qualitative insight in the consequences of the conveyance over the watersheds for sediment exchange. Figures 5.14 and 5.15 first show time series for the sediment transport (suspended load + bedload transport) over the watersheds of respectively Terschelling and Ameland for the duration of the field campaign. Time series of the measured discharge at observations points at these watersheds for this period are included in Figure 5.2. The peak values for sediment transport at September 13th are this large that the time series are presented at two different vertical scales.

The peaks at September 13th are really distinct. There is more sediment moving over the watersheds during this storm event than during the remaining part of the field campaign. For every tidal period, the residual sediment transport is directed towards the east of the watershed, but for many tidal periods in the record the magnitude of the residual sediment transport is only small (< 50 m^3 for the Terschelling watershed and < 10 m^3 for the Ameland Watershed). The residual sediment transport during the tidal period covering the peak of the storm on September 13th is 3 orders higher in magnitude ($\cdot 10^3$) than during other tidal periods. In addition there are a few other tidal periods during which a significant residual transport is observed. Spring tides bring more sediment into motion than neap tides, as indicated in Figures 5.14 and 5.15.

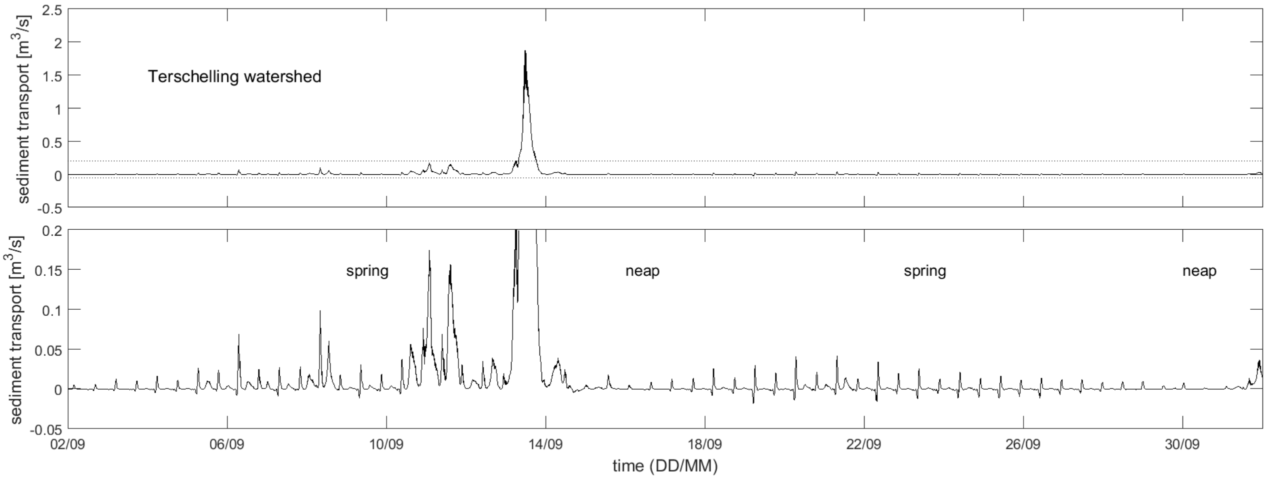

Figure 5.14: Time series of the sediment transport (D = 200μm) over Terschellinger Wad for the duration of the field campaign. The lower plot zooms in on the area between the horizontal dotted lines in the upper plot. Sediment transport towards the east is considered positive.

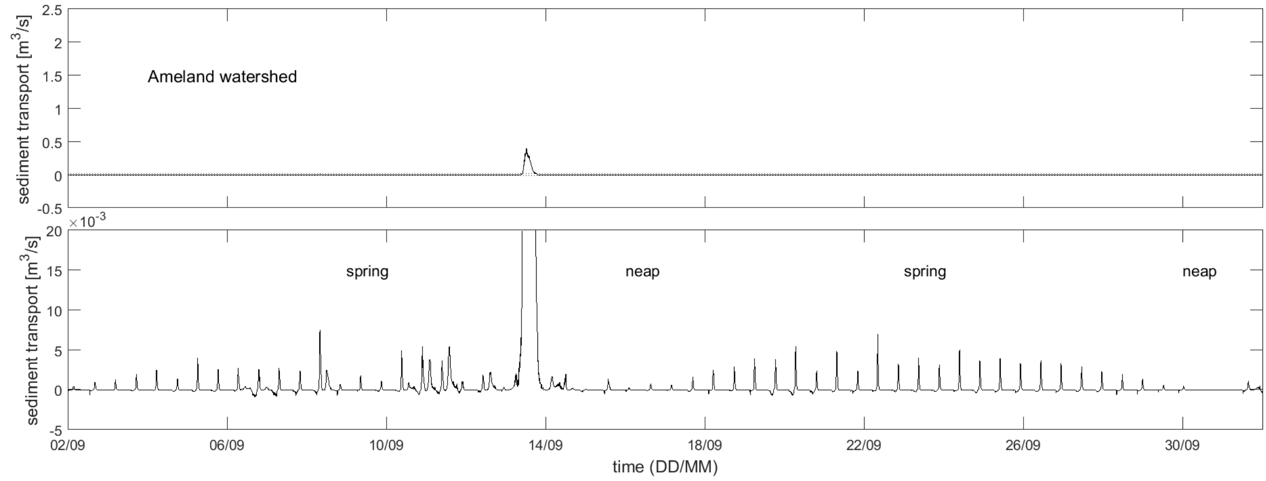

Figure 5.15: Time series of the sediment transport (D = 200μm) over Pinke Wad for the duration of the field campaign. The lower plot zooms in on the area between the horizontal dotted lines in the upper plot. Sediment transport towards the east is considered positive. Note the vertical scale in the lower figure is different from Figure 5.14.

Figure 5.16 shows the cumulative sediment transport over each of the two watersheds for a full year and for simulations with different forcing mechanisms enabled. Distinct are the big steps in the residual transport, indicating short periods of time with large sediment transport capacities. The storm event at September 13th had the biggest contribution in the yearly residual of all tidal periods. The difference between the sediment transport over the Terschelling watershed and the Ameland watershed is around a factor 10. Both yearly residual transports are directed towards the east. Although waves do hardly change the residual discharge over the watersheds (see Figure 5.9), the stirring mechanism of waves at these shallow areas largely increases the sediment transport over the watersheds. The significant wave height can rise up to 0.8 m/s at some locations in the cross-section, according to modelling results. For simulations without waves and wind the residual discharge over the watersheds is directed towards the west, whereas the residual sediment transport is still in eastward direction. This indicates a certain flow asymmetry at the watersheds during calm wind conditions.

Considering the wind conditions that lead to large residual sediment transports, Figure 5.17 shows the residual sediment transport per tidal period in relation to the tide-averaged wind conditions. Compared to similar figures for the discharge (see Figure 5.8), it is now less tidal periods that lead to a significant transport. 5% of the tidal periods are responsible for more than half the yearly sediment transport over the watersheds. According to Figure 5.17, the tide-averaged wind speed must exceed at least 8 m/s to yield a significant residual sediment transport over the watershed.

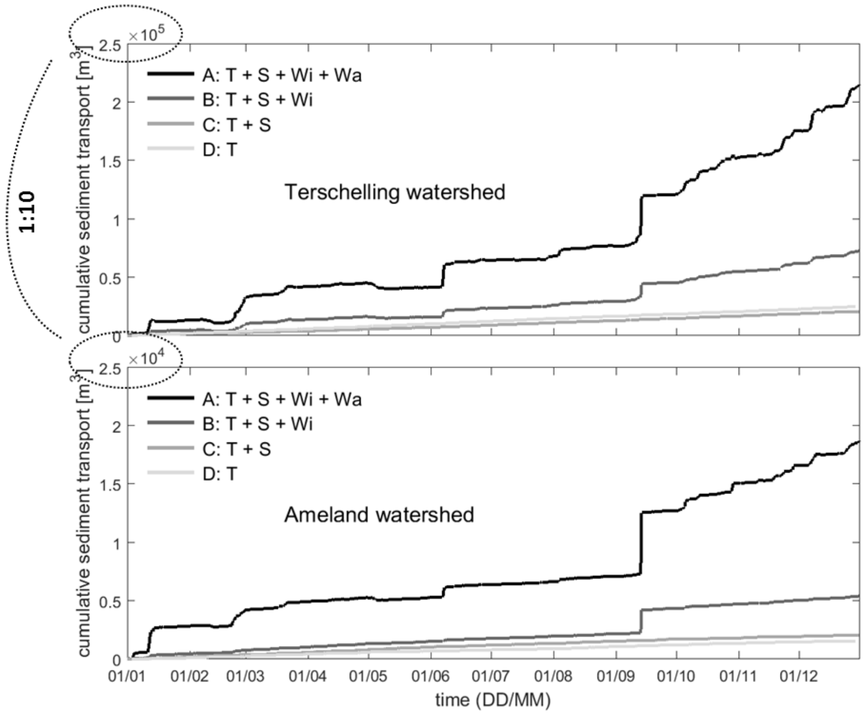

Figure 5.16: Course of the residual sediment transport (D = 200μm) over the watersheds of Terschelling (top) and Ameland (bottom). Results of four different model simulations with different sets of forcing mechanisms are included. Sediment transport towards the east is considered positive. Note the vertical scales of the two figures differ a factor 10.

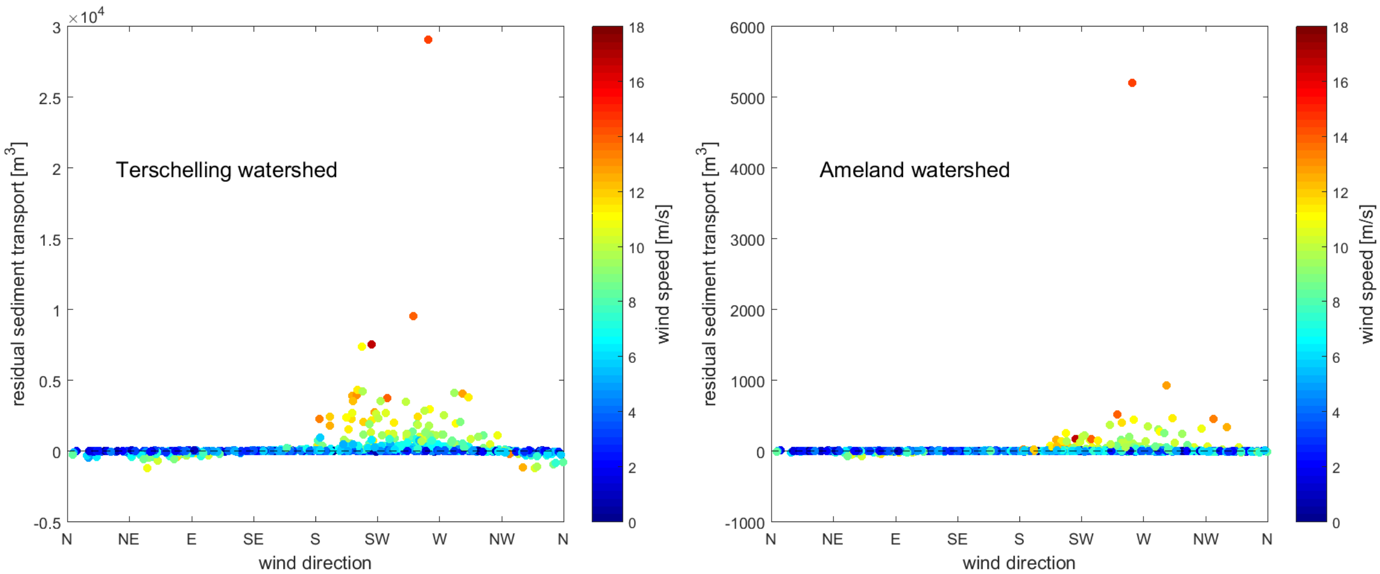

Figure 5.17: Residual sediment transport (D = 200μm) over the watersheds of Terschelling (left) and Ameland (right) per tidal period in 2017 in relation to the tide-averaged wind conditions. Note the scales of the vertical axes differ to improve visibility.

Key points

- The residual discharge over the watersheds of Terschelling and Ameland is dominantly governed by local wind shear stresses. Evidence from field observations was supported with numerical modelling results.
- The conveyance capacity and the residual flow at the Ameland watershed are smaller than at the Terschelling watershed. The difference in magnitude of the residual flow between the two watersheds is largely contributing to the residual flow through Ameland Inlet. The residual discharge per tidal period over the Ameland watershed can be estimated as 25-30% of the residual discharge over the Terschelling watershed.
- The orientation of the principal wind directions for the Ameland watershed is different than for the Terschelling watershed, as can be understood from the orientation of the tidal inlet system. This, in relation to the prevailing winds form the southwest, has additional consequences for the residual flow through Ameland Inlet.
- A wind driven residual discharge through the Wadden Sea was found to be of the same order of magnitude (i.e. per unit width) at shallow shoals and in deeper channels.
- Wind speeds need to exceed 8 m/s for a significant residual sand transport over the watersheds. The residual sand transport over the watersheds at a time scale of about a year is dominated by storm events.

6
System behaviour
Connecting the dots

In the current chapter, results from earlier chapters are merged with new modelling results to find the implications of what was discussed before for the residual discharge through Ameland Inlet. The second part of this chapter discusses spatial and temporal variations in flow and sediment transport, and thereby the representativeness of field observations for the general behaviour of Ameland Inlet system.

6.1. Exchange flow through Ameland Inlet

This section first considers the residual discharge through Ameland Inlet in 2017. Subsequently, the depth-averaged flow structure in Ameland Inlet is discussed based on modelling results for a full year.

6.1.1. Residual discharge

The residual flows over the watersheds determine the net flow through Ameland Inlet, as presented in Figure 6.1. Over 2017, there is a residual outflow through Ameland inlet of $6.9{\cdot}10^9$ m^3, which is about 16 times the mean tidal prism. Mainly during the winter months the residual discharge is outward directed, due to the wind-driven residual inflow over the Terschelling watershed. During calmer periods (i.e. summer), Ameland Inlet experiences a residual inflow. This leads to an interesting sawtooth pattern in the cumulative discharge, shown in Figure 6.1.

Because the residual flow through Ameland Inlet varies with the wind dependent flow over the watersheds, the residual discharge through the inlet is largely dependent on the acting wind conditions. This is presented in Figure 6.2 as the residual flow per tidal period in relation to the tide-averaged wind conditions. Per tidal period the residual outflow can be almost as large as the mean tidal prism. In agreement with the seasonality in Figure 6.1, the residuals are generally in flood-direction during calm wind conditions, but also during stronger winds from the north-northeast.

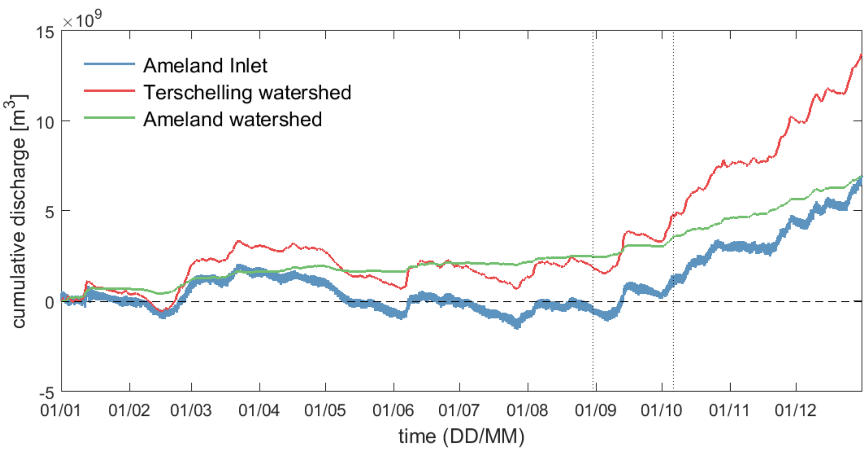

Figure 6.1: Course of the residual discharge through Ameland Inlet and over the watersheds of Terschelling and Ameland in 2017. Flows towards the north and towards the east are considered positive, which implies inflow into Ameland basin for the Terschelling watershed and outflow for Ameland Inlet and the Ameland watershed. The vertical dotted lines indicate the timespan of field observations.

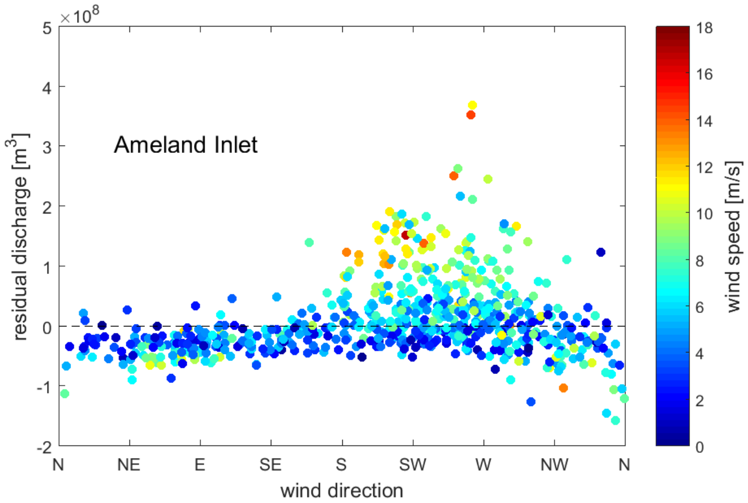

Figure 6.2: Scatterplot of the residual discharge through Ameland Inlet per tidal period in relation to the tide-averaged wind forcing. The results are based on model simulations of a full year (2017). Outward directed flow (= ebb) is considered positive.

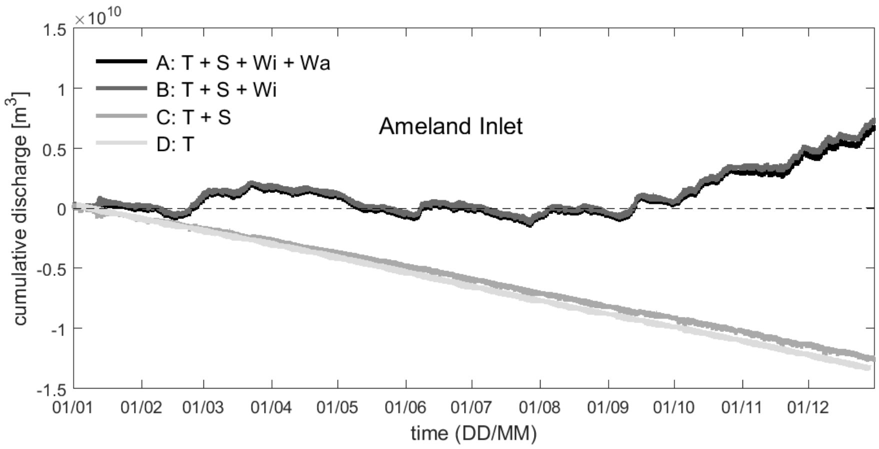

Figure 6.3: Course of the cumulative discharge through Ameland Inlet in 2017 for four model simulations with different sets of forcing mechanisms enabled. The results for simulation **A** are also included in Figure 6.1. Discharge is considered positive in ebb-direction (outward).

During strong-winds from the west-southwest the residuals are directed outward. The preferential wind direction for residual outflow through Ameland Inlet is the same as for inflow over the Terschelling watershed. This was already expected from the volume balance of Ameland basin (see Figure 6.1). Large residual inflows through Ameland Inlet during winds from the north can be explained by the orientation of the inlet, since wind shear stresses are then directed more or less perpendicular to the inlet (see e.g. Figure 1.1). These inflows lead to a westward residual discharge over the Terschelling watershed, as was observed in Figure 5.8.

From the different model simulations it follows that wave-driven currents cause a small residual inflow through Ameland Inlet; the course of the residual discharge through Ameland Inlet in 2017 is slightly modified by including waves in the simulation. This is shown in Figure 6.3, and is qualitatively in agreement with field measurements at observation point Frame 3: Inlet (see e.g. Figures 4.7 and 4.15). Because there is a residual inflow during calm wind conditions, the residual discharge is continuously in flood-direction in model simulation without wind forcing. Local wind effects thus change the direction of the residual discharge through Ameland Inlet. Supported by Figure 5.9, it is now clear that during calm wind conditions Ameland basin experiences a residual inflow through Ameland Inlet and over Pinke Wad, and a residual outflow over Terschellinger Wad.

6.1.2. Flow structure in Ameland Inlet

During the field campaign, the residual discharge at the observation point in the inlet (Frame 3: Inlet) was directed outward for almost all tidal periods in the record (see Figure 4.7). Since this is not true for the residual discharge integrated over the inlet's cross-section, the flow structure in Ameland Inlet is investigated here using numerical modelling results. The cross-section is indicated in Figure 6.4. For every grid cell along that cross-section the dominant flow direction is determined for every tidal period in 2017. The results are presented in Figure 6.5 as the fraction of tidal periods in 2017 that were ebb-dominant. Figure 6.5 also shows the bed level in the model bathymetry, the cumulative discharge in ebb- and in flood-direction, and the magnitude and direction of the residual discharge per grid cell over 2017. The inlet is orientated under an angle of approximately 16° relative to the positive x-axis.

Because the tidal wave is partially progressive and the water level in the inlet is thus generally higher during flood than during ebb, the channels were expected to be ebb-dominant. To some extent this appears to be true. Even the shallow channels at Boschplaat are either less flood-dominant than the shoals between the channels or they are ebb-dominant. And in general, the deepest channel in the cross-section (i.e. Borndiep) is also ebb-dominant. It follows from Figure 6.5, however, that there is a section in the Borndiep channel that is not ebb-dominant. At this section, only 37% of the tidal periods in 2017 had a residual flow in outward direction and the residual flow over a full year is directed in transversal direction. The shallower eastern part of Borndiep is clearly flood-dominant. The variation in residual flow direction over the inlet's channel makes the field observations at observation point Frame 3: Inlet regarding the direction of residuals not necessarily representative for the entire inlet.

A possible explanation for the remarkable residual flow structure in the Borndiep channel can be the complex and highly varied bathymetry in this area. The explanation follows from the flow characteristics a little further offshore than the inlet. This is supported by Figure 6.6, which shows the residual flow in 2017 per grid cell in a cross-section approximately 500 m offshore of Ameland Inlet, and by Figure 6.4, which shows the bathymetry around the inlet. A flood-dominant channel (i.e. Westgat) is orientated from west-northwest to east-southeast. The flood flow in this channel confluences into the Borndiep channel a bit further offshore than the white cross-section in Figure 6.4. It is expected that the momentum of flow from this channel causes the residual flow on the western side of Borndiep channel to be directed east-southeast at the white cross-section (see Figure 6.4). Considering the flood-dominant flow from the Westgat channel as a kind of jet flow into Borndiep channel can then explain why the residual flow in Ameland Inlet is not offshore directed for a certain section (see Figure 6.5).

The shallow eastern part of Borndiep channel bifurcates into a separate channel further offshore, which becomes shallower towards a shallow shoal (i.e. Bornrif). This part is flood-dominant for almost all tidal periods. The conveyance from this channel causes the eastern part of Borndiep also to be flood-dominant (see Figure 6.5).

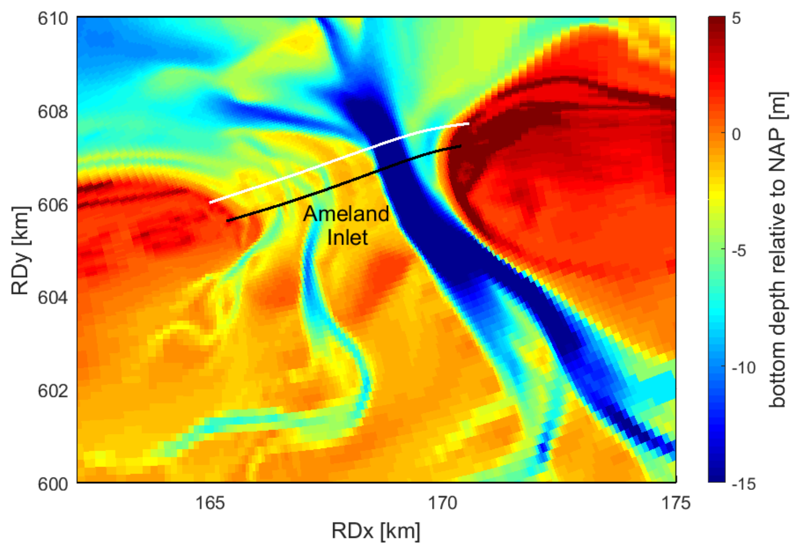

Figure 6.4: Model bathymetry at Ameland Inlet and the position of cross-sections in the inlet. The black line is considered the inlet gorge and used in that way throughout this study. The white line is used to explain the residual flow structure in the inlet in Figure 6.6.

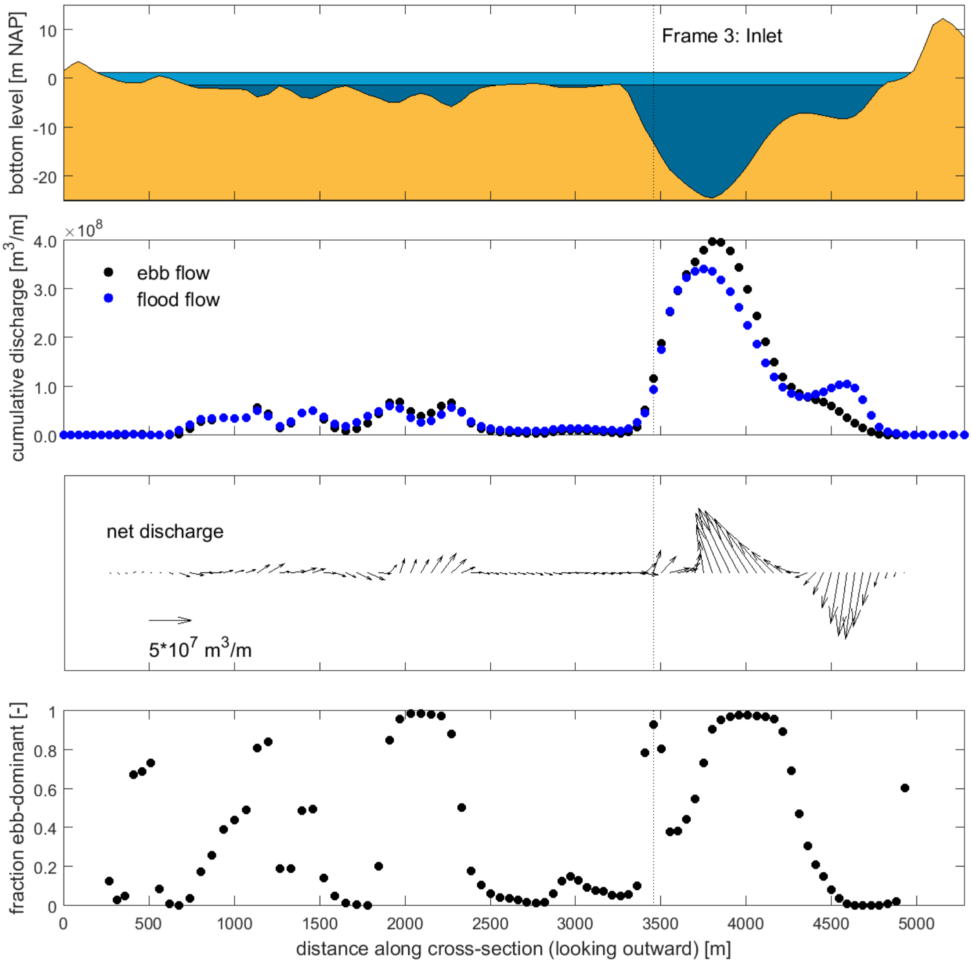

Figure 6.5: Flow structure in Ameland Inlet, based on modelling results of a full year (2017). The top figure shows the bed level in the cross section, the lighter blue indicates the tidal range. The two middle figures show per grid cell the cumulative discharge in ebb- and flood-direction and the magnitude and direction of the residual discharge over a full year. The bottom figure shows per grid cell the fraction of times the subtidal discharge was outward direction (= ebb). The vertical dotted line indicates the position of measurement Frame 3 in the cross-section during the field campaign. The location of the cross-section is indicated in Figure 6.4 by the black line.

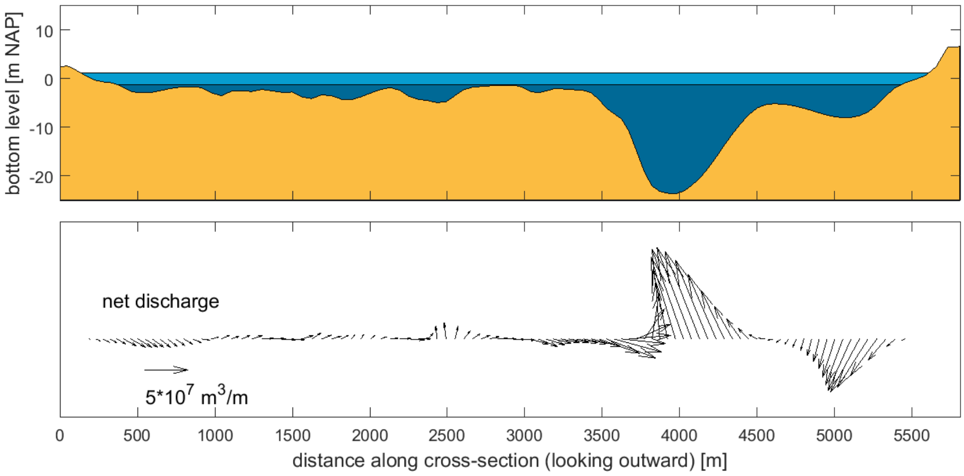

Figure 6.6: Magnitude and direction of the residual discharge over a full year for every grid cell in a cross-section just offshore of Ameland Inlet. The location of the cross-section is indicated in Figure 6.4 by the white line.

6.2. Variations in space and time

In Chapter 4, the temporal variations in residual discharge and sediment transport are discussed for the duration of the field campaign at several observation points. In this section the duration is extended to a full year, and also the spatial variations are considered. The content of this section is largely based on modelling results.

Residual discharge

Considering the magnitude of residual flow per tidal period, Figure 6.7 shows the cumulative residual discharge for a fraction of tidal periods that are sorted by ascending wind speed. The four observation points from the field campaign are included and every tidal period in 2017 is included in the underlying data. The way in which the modelling results are presented here only includes the magnitude of the residual discharge, such that a change in direction of the residual flow would not lead to changes in the presented figures. In general, the line in Figure 6.7 becomes more non-linear for more shallow locations. This implies that shallow locations are more significantly governed by wave- and wind-driven residual currents. The fraction of the cumulative discharge during the 80% least windy tides is now used as a characteristic parameter for the non-linear behaviour. This characteristic parameter, from now on referred to as $f_{80,dis}$, is determined based on the modelling results for every grid cell at the ebb-tidal delta. The results are presented in Figure 6.8.

At the three observation points at the ebb-tidal delta the value for $f_{80,dis}$ is around 70%. At the observation point in the inlet (Frame 3: Inlet) the course is almost linear. It follows from Figure 6.8 that there is more spatial variation in the value of $f_{80,dis}$ than captured in the field observations. At some shallow parts of the ebb-tidal delta, $f_{80,dis}$ reduces to 0.6. The residual discharge at these locations is thus more severely influenced by wave- and wind-driven currents. At the eastern part of the ebb-tidal delta, there is a shallow area where $f_{80,dis}$ even drops to around 0.52, likely because it is both shallow and it is conveying much water during large residual outflows from Ameland Inlet. The darker blue area at the right edge of Figure 6.8 indicates the start of the surfzone along the North Sea coast of Ameland. Further offshore than the ebb-tidal delta, the residual discharge is also more influenced by the wind. This area has not been in the scope of this project earlier. It is believed that a strong alongshore current during periods with high wind speeds increases the residual discharge offshore of the ebb-tidal delta.

Residual sediment transport

A similar analysis is done for the residual sediment transport. The non-linearity of the residual sediment transport is presented for the same four observation points in Figure 6.9. The stirring contribution of waves makes that sorting the tidal periods by ascending wind speed is fairly different from sorting the tidal periods by ascending contribution in the cumulative sediment transport. Since the highest-energy waves are generated by winds from a different direction (northwest) than the prevailing wind direction for strong winds (west-southwest), the sediment transport

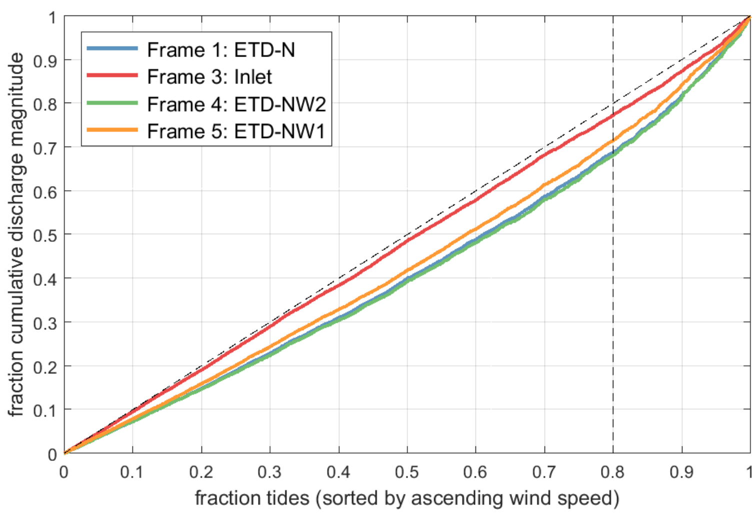

Figure 6.7: Fraction of the cumulative discharge over a year (vertical axis) during a fraction of the tidal periods that are ordered by ascending wind speed (horizontal axis). The diagonal dashed line indicates the situation in which the residual discharge of every tidal period is the same in magnitude. Results are included for four observation points during the field campaign.

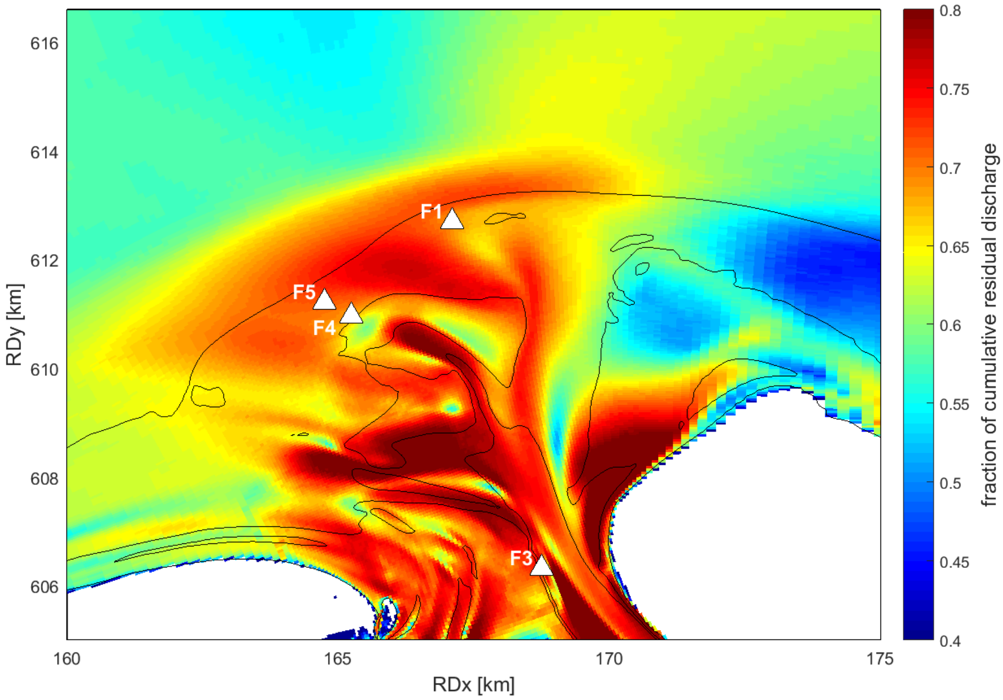

Figure 6.8: Fraction of the cumulative residual discharge during the 80% least windy tides ($f_{80,dis}$) per grid cell at the ebb-tidal delta. Triangles indicate the locations of observation points included in Figure 6.7. Isobars are 0, -5 m and -10 m depth contours relative to NAP.

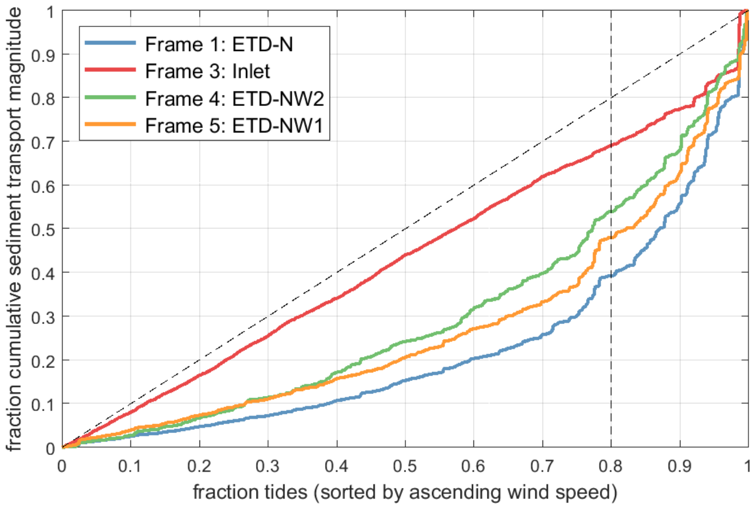

Figure 6.9: Fraction of the cumulative sediment transport over a year (vertical axis) during a fraction of the tidal periods that are ordered by ascending wind speed (horizontal axis). The diagonal dashed line indicates the situation in which the sediment transport of every tidal period is the same in magnitude. Results are included for four observation points during the field campaign.

during a tidal period can be high, whereas the tide-averaged wind speed is not particularly high. These tidal periods can be recognised in Figure 6.9 by the stepwise course. Figure 6.9 is similar to Figure 4.17, which is based on the sediment transport as computed from field observations. During field observations the non-linearity in sediment transport at the ebb-tidal delta was even higher, likely induced by the relatively strong meteorological forcing (i.e. winds) during this timespan (see Section 2.2).

Figure 6.10 presents $f_{80,sedt}$ for every grid cell at the ebb-tidal delta. Note that the fraction of the cumulative sediment transport does not address the magnitude of the cumulative sediment transport. The increased non-linearity compared to the residual discharge is now addressed in space. At the shallowest parts of the ebb-tidal delta, the value of $f_{80,sedt}$ reduces to around 0.3. Offshore of the three observation points at the ebb-tidal delta the values of $f_{80,sedt}$

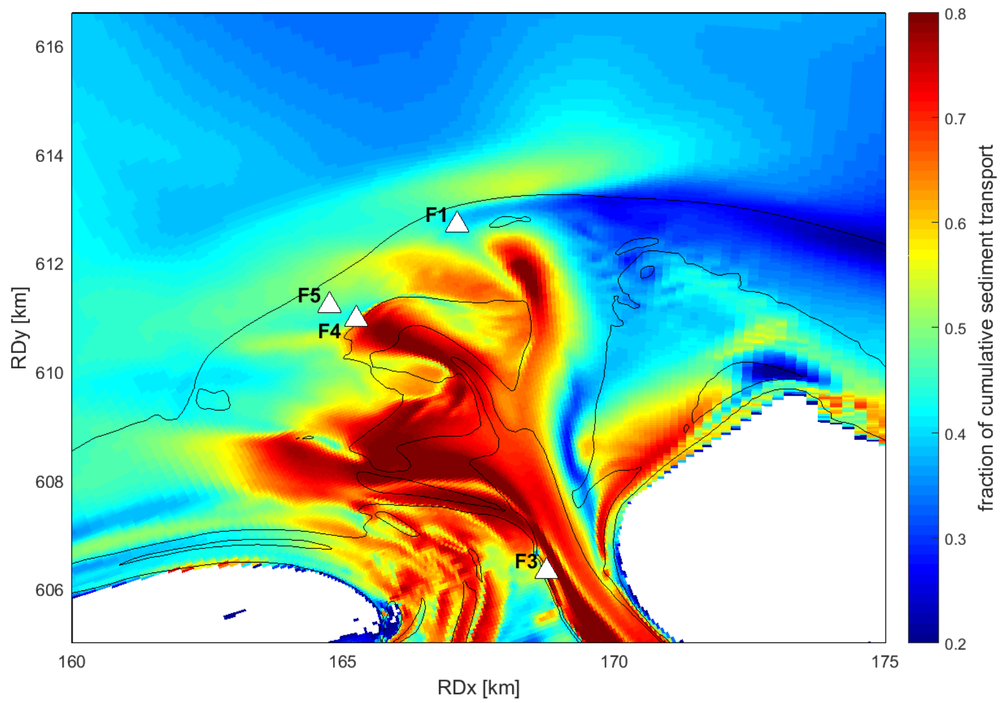

Figure 6.10: Fraction of the cumulative residual sediment transport during the 80% least windy tidal periods ($f_{80,sedt}$) per grid cell at the ebb-tidal delta. Triangles indicate the locations of observation points included in Figure 6.9. Note the colour scale is different from Figure 6.8.

are also low; sediment transport rates can be expected to be high during high-wave conditions in combination with a strong alongshore current, and thus during strong wind conditions. Frame 3 is located at one of the darkest red areas in Figure 6.10, indicating it is one of the most linearly behaving points in the system regarding the course of the cumulative sediment transport over time. Observations at Frames 1, 4 and 5 are considered representative for the outer edge of the ebb-tidal delta, for water depths between 5 to 12 m. Closer towards the inlet the tidal currents become more concentrated in the channels and the linearity increases. At shallower shoals next to the channels, the meteorological forcing mechanisms are of more importance again. This spatial variability at the ebb-tidal delta is hardly included in results from point observations in the field.

The most important finding in this section is probably the spatial variation at the ebb-tidal delta. The discharge and the sediment transport through channels are mainly governed by tidal currents and therefore almost linear in time. At shallower parts, the residual discharge is more governed by meteorological forcing conditions. For the sediment transport over these shallow areas, the stirring effect of wind waves is of importance, next to the residual flows.

The modelling results regarding sediment transport in the entire inlet system are presented in a similar way in Figure 6.11. Although this method was initially intended to investigate the spatial representativeness of field observations, it also provides more insight in the governing processes per location. Warm colours (i.e. red and orange) in Figure 6.11 indicate locations where sediment transport is governed by (concentrated) tidal currents. Cool colours (i.e. blue and to a lesser extent green) indicate locations where sediment transport is governed by meteorological forcing conditions. The spatial pattern is strikingly similar to the bathymetry in Ameland basin (see e.g. Figure 2.2). This emphasizes how much the shallowness of Ameland inlet system explains about the importance of meteorological forcing conditions for hydrodynamics and residual sediment transport.

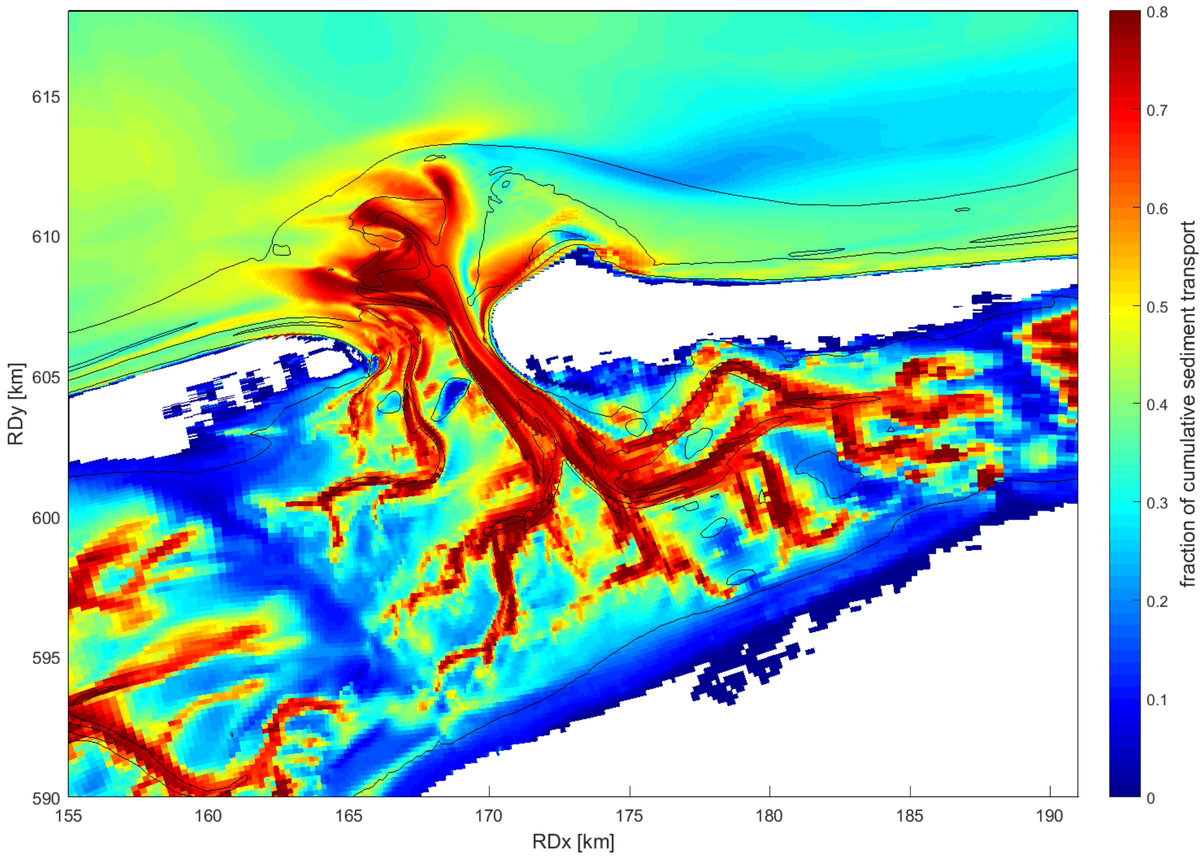

Figure 6.11: $f_{80,sedt}$ per grid cell in Ameland Inlet system, based on a numerical simulation of a full year (2017). Isobars are 0, -5 m and -10 m depth contours relative to NAP. Note the colour scale is different from Figure 6.10.

Key points

- Residual flow over the watersheds of Terschelling and Ameland leads to a residual outflow through Ameland Inlet of around 16 times the mean tidal prism in 2017. The residual outflow is largest during winds from the west-southwest. Ameland Inlet experiences a residual inflow during calm wind conditions.
- The flow structure in Ameland Inlet shows a spatially varying ebb- or flood-dominance, also in the main channel (i.e. Borndiep). The flow structure can (partly) be explained by the local bathymetry. Observation point Frame 3 was located at a peculiar point in the inlet, and field observations at this point are therefore not necessarily representative for the entire inlet.
- The spatial variation in the contribution of meteorological forcing conditions to residual discharge and sediment transport at the ebb-tidal delta is larger than captured in the field observations. Numerical modelling results, on the other hand, provide much insight into spatial patterns.

7
Discussion

The results in this study mainly addressed the nonstationarity of flow and sediment transport at the ebb-tidal delta of Ameland Inlet due to meteorological forcing conditions and the wind-driven interconnectivity of tidal basins. The latter has consequences for the residual flow through the tidal inlet and thus contributes to the nonstationary flow conditions at the ebb-tidal delta.

Spatial and temporal representativeness

Few studies have addressed the flow characteristics at ebb-tidal deltas based on field observations. The present study started with a classical harmonic analysis on time series obtained in the field during a 40-days field campaign. It turned out the harmonic constituents were strongly disturbed by non-tidal energy. As a consequence, parts of the results from harmonic analysis were unreliable. Considering the non-tidal energy, the field campaign took place during a period in which meteorological forcing (i.e. wind) was stronger than year-averaged. The fraction of time during which the wind speed exceeded 16 m/s was four times as high over the duration of the field campaign than over 2017. This makes the temporal extent of field observations not necessarily representative for the general behaviour of the system. On the other hand, the field observations provide useful insights into the interaction of tides with other forcing mechanisms during highly energetic conditions.

Field observations of the flow conditions are limited to three observations points at the ebb-tidal delta, one in the tidal inlet's main channel, and three observation points at each of the two watersheds. Results from numerical modelling have been used to increase the spatial extent. The same modelling results were used in Chapter 6 to discuss the representativeness of the field measurements at observation points for the larger system. It was found that there is more spatial variation in the effect of meteorological forcing on residual discharge and sediment transport at the ebb-tidal delta than captured in the field observations. This underlines the importance of numerical modelling for a further analysis of the system behaviour. Also, it indicates that conclusions from point observations in a complex system like Ameland Inlet should be treated with great care. Observation point Frame 3: Inlet was found to be located at a peculiar point in the inlet, where flow conditions were different from representative for the entire inlet due to the local bathymetry (see Figure 6.5). One is urged to consider this while interpreting findings from field observations at observation point Frame 3: Inlet.

Insights regarding sediment transport rates that are discussed in this study are based on Delft3D modelling results. In these model simulations, the sediment composition is assumed uniform (D = 200 μm) and sediment transport rates are computed based on the Van Rijn transport formulations (Van Rijn, 2007ab). The sensitivity of the modelling results to these assumptions has not been investigated yet.

Basin connectivity

The interconnectivity of tidal basins in the Western Dutch Wadden Sea has been part of earlier research by Duran-Matute et al. (2016). The results from field observations at the Terschelling watershed provide evidence for their findings. In addition, their quantitative analysis based on modelling results has been extended towards the next watershed and the consequences for Ameland Inlet were investigated. During 41% of the tidal periods in 2017 the residual discharge over the Terschelling watershed is more than 10% of the mean tidal prism through Ameland Inlet. During 19% of the tidal periods the residual discharge also exceeds 20% of the tidal prism. These numbers indicate a significant exchange between back-barrier basins. The difference in conveyance capacity between the watersheds of Terschelling and Ameland leads to a yearly residual outflow through Ameland Inlet. Exchange over the watersheds was found to increase with increasing water levels. This supports Wang et al. (2018), who suggest that the exchange may increase if watersheds become less distinct due to relative sea level rise.

Studies considering the long-term sediment budget of tidal basins in the Dutch Wadden Sea (e.g. Kragtwijk et al., 2004; Van Goor et al., 2003; Wang et al., 2018) are often based on aggregated models, such as ASMITA (Stive et al., 1998). These models do not include the exchange with adjacent basins, but do assume tidal basins to be closed at the watersheds. Since the transport over the watersheds and thus the exchange with neighbouring basins was found to be important for hydrodynamics and residual sediment transport, an important mechanism is missing in aggregated models. It is yet to be investigated what the consequences of exchange between basins are for the empirical equilibrium relations underlying aggregated models, since these are eventually used to assess the long-term sediment budget of tidal inlet systems. This could for example lead to equilibrium relations for the volume of morphological elements that include more system characteristics than just the tidal range and the basin area.

Generalisation

The shallowness of the Wadden Sea, in combination with the alignment with the prevailing wind direction, appears to yield favourable conditions for net exchange between basins. Offshore of the inlet, wind shear stresses induce an alongshore current over the shallow ebb-tidal delta. The extent of shallow areas is found to be important for the development of wind-driven residual currents, as was shown in Chapter 5 and in earlier work by Li (2013). In his research on the development of wind-driven residual currents, Li (2013) found with numerical experiments that residual currents at shallow areas are driven by wind shear stresses in the direction of the wind, leading to compensation flows at deeper areas. This is also what is observed around Ameland Inlet; wind shear stresses do not generate large flows through deeper channels, but they generate flows at shallow areas that affect the residuals in deeper parts.

Specific for Ameland Inlet is the difference in conveyance capacity between the two bordering watersheds. This leads to significantly large consequences of flow over the watersheds for the residual flow through Ameland Inlet. Also, the system orientation (see Figure 7.1) in relation to the prevailing wind directions is such that nearby tidal inlets on the west of Ameland Inlet (i.e. Texel Inlet and Eierlandse Gat) experience a residual inflow during the strong southwestern winds (Duran-Matute et al., 2016), such that there is ample supply for eastward residual flows over Terschellinger Wad. This is believed to be different for watersheds in the East Frisian Wadden Sea, where a possible residual inflow through inlets must be induced by a pressure gradient.

Figure 7.1: Satellite image of the Wadden Sea area and the barrier islands. The orientation of the Wadden Sea relative to the North Sea changes from west-east to south-north towards the east. The white dotted oval indicates Ameland Inlet system. Courtesy: Wadden Sea Secretariat.

Since the orientation of the shallow system in relation to the prevailing wind direction is believed to induce the importance of wind-generated residuals, these are the conditions for a more general application of the results of this study beyond Ameland Inlet. Other inlet systems in the Dutch and German Wadden Sea may therefore benefit from the results presented here. Further North, towards Denmark, the Wadden Sea becomes more north-south orientated (see Figure 7.1), and the strong winds from the west are then expected to better contribute to surge than to residual (alongshore) flows and transport. This difference in wind dependence between inlets in the Dutch Wadden Sea and the East Frisian Wadden Sea on the one hand and inlets in the North Frisian Wadden Sea on the other hand was also mentioned by Gräwe et al. (2016) while investigating the correlation between wind stress and residual transport velocity profiles.

Implications

At Ameland Inlet system the complex bathymetry and the energy of both tidal and meteorological forcing leads to nonstationary flow fluctuations. The spatial variation of the relative contributions of different forcing mechanisms is both interesting and challenging. Locations where the transport of matter is dominated by highly energetic meteorological conditions and where the transport of matter is more deterministic due to the concentration of tidal currents are intertwined. Investigating patterns therein helps to evaluate plausible pathways of sediment particles, but also to investigate benthic habitat distributions.

Analyses and simulations of this and similar systems lose their accuracy if the forcing mechanisms are schematised. This is however inevitable in process-based morphodynamic simulations of multiple years, in order to avoid excessive computation times. A commonly applied morphodynamic updating technique is based on the multiplication of morphological change per computational time step by a morphological scaling factor (MF) (see e.g. Roelvink, 2006), in order to reduce computation times by a factor MF. Such an approach comprises the selection of a morphological representative tidal signal and representative wave conditions (e.g. Walstra et al., 2013). For Ameland Inlet, wind-driven residual currents are believed to govern the morphodynamic evolution together with tides and waves, and therefore an additional challenge is to determine a representative wind climate. Since swell waves are more or less absent around Ameland Inlet, the correlation between wind and wave conditions could possibly lead to a combined classification in representative meteorological conditions.

In earlier studies, Ameland Inlet has often been considered as a tidal basin bordered by closed watersheds. In this study the conditions that lead to a residual flow have been discussed and the in- and outflow over the watersheds was found of such a magnitude that it has significant consequences for the exchange processes through Ameland Inlet. A residual outflow during strong wind conditions and a residual inflow during calm conditions are believed to be crucial for the system's sediment budget.

8
Concluding remarks

A residual current over the ebb-tidal delta of Ameland Inlet system was observed in field observations, of which a variation in direction and especially in magnitude was driven by meteorological forcing mechanisms. The residual current was found to be as large as the ebb-current for a storm event during the measurements, thus preventing flow from reversing at the ebb-tidal delta. Tidal constituents could not accurately be resolved from 40 days of field observations, because of nonstationary variations in the flow. Modelling results revealed that both waves and local wind shear stresses lead to nonstationary flow variations.

Winds from the west amplify the residual flow over the ebb-tidal delta in northeast direction. Also, high waves from the northwestern quadrant change the residual flow. Since waves observed near Ameland Inlet are locally generated wind waves, high waves are often observed simultaneously with high wind shear stresses. The combination of the stirring effect of waves with strong residual flows makes it such that a limited number of periods (≈ 20%) contribute to the vast majority (≈ 80%) of the cumulative sediment transport at shallow parts of the ebb-tidal delta.

The wind-dependent interconnectivity of tidal basins in the Dutch Wadden Sea yields a yearly residual outflow through Ameland Inlet. Per tidal period, the residual outflow can be in the order of magnitude of the mean tidal prism (up to 90% during storm conditions). The variation in residual flow through Ameland Inlet varies with the wind forcing, and therefore shows a seasonal variation; i.e. strong winds from the prevailing wind direction usually occur during the autumn and winter months. During calm wind conditions, Ameland Inlet experiences a residual inflow. This is illustrated schematically in Figure 8.1. The residual flow over the Ameland watershed is smaller than the residual flow over the Terschelling watershed. Per tidal period the residual discharge over the Ameland watershed can be estimated as 25-30% of the residual discharge over the Terschelling watershed. The preferential wind directions for flow over the watersheds can be explained from the orientation of the Wadden Sea. The discharge over the Terschelling watershed per tidal period can be as large as the mean tidal prism through Ameland Inlet.

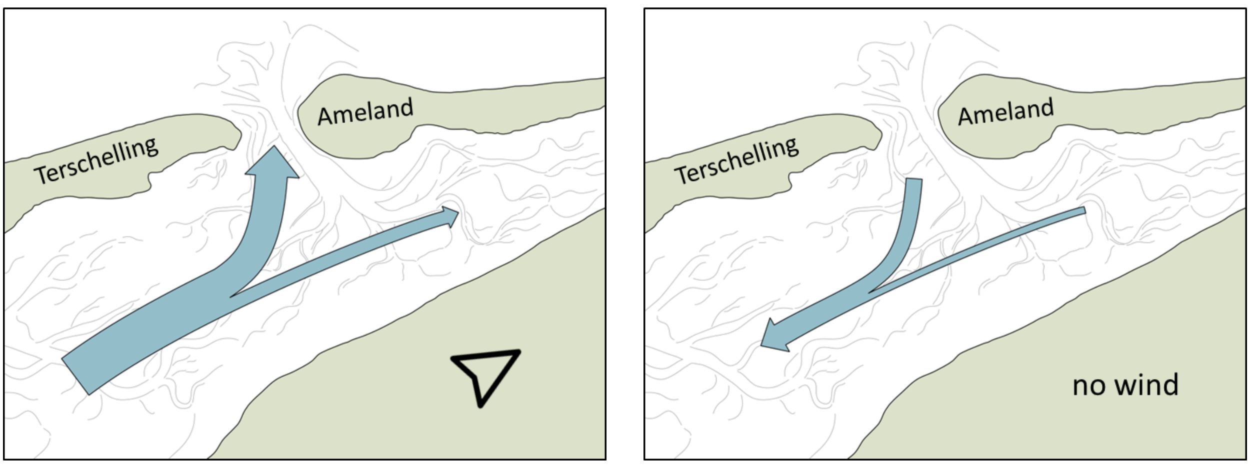

Figure 8.1: Schematic presentation of the large scale exchange flows between Wadden Sea basins and the North Sea, both for the prevailing southwestern winds (left) and for calm wind conditions (right).

Since wind shear stresses and wind waves generate residual flows both locally and at the scale of the system, wind forcing has an important contribution in the exchange processes that determine the development of Ameland Inlet system. Wind forcing and the variability therein should therefore always be considered in analyses and predictive model simulations of shallow tidal inlet systems.

Focus of future research

In the present study, large scale hydrodynamics have been investigated and some first insights regarding sediment transport were discussed. This contributes to the objectives of the Kustgenese 2.0 and SEAWAD research programmes, but also leaves plenty of opportunities for further research. The suggestions given here mainly concern the extension of analyses of sediment transport and sediment pathways.

So far, modelling efforts regarding sediment transport have only considered one uniform sand fraction. The sensitivity of results to the grain diameter of uniform sand would improve the quality of results. An even better representation of reality would include multiple sediment fractions. The quality of numerical model simulations of sediment transport and eventually of morphodynamic development is expected to benefit from the analysis of field measurements regarding sediment transport, which were part of the Kustgenese 2.0 / SEAWAD field campaign. This is going to be an essential step for improvement of the predictive capabilities of numerical simulations for coastal management in general, and for studies regarding the feasibility of nourishments at ebb-tidal deltas in particular.

The hydrodynamic field observations at the watersheds, obtained during the fall 2017 field campaign, led to essential insights into the exchange between tidal basins in the Wadden Sea. Regarding the sediment balance of the Wadden Sea, it would be useful if a future field campaign also includes field measurements of the sediment transport over the watersheds. In the present study, a measure of the sediment transport capacity was based on modelling results, assuming that the sediment consists of one uniform sand fraction. Previous surveys (e.g. Compton et al., 2013; Rijkswaterstaat, 1999) report a finer sediment composition at the watersheds, which partially consists of mud. This is not well-represented by the current model assumptions. Field observations of sediment transport at the watersheds are expected to yield fundamental insights on the transport of suspended matter, and more particularly on the transport of mud, as well as better estimates of the sediment volumes going in and out of tidal basins.

Moreover, one is recommended to investigate the occurrence of three-dimensional flow structures (i.e. due to baroclinic flows) and their importance for residual discharge and sediment transport. This should address the validity of the assumption to use a depth-averaged approach in the analysis of field observation and in modelling efforts. The present study has also discussed the characteristics of the flow structure in Ameland Inlet. It would be useful and interesting to validate and investigate this flow structure further with field observations. Especially that combination of field observations with modelling results is expected to yield valuable insights into the physical processes that govern the development of tidal inlet systems.

Bibliography

Bartholomä, A., Kubicki, A., Badewien, T. H., and Flemming, B. W. (2009). Suspended sediment transport in the German Wadden Sea - seasonal variations and extreme events. *Ocean Dynamics*, 59(2):213–225.

Bertin, X., Fortunato, A. B., and Oliveira, A. (2009). A modeling-based analysis of processes driving wave-dominated inlets. *Continental Shelf Research*, 29:819–834.

Booij, N., Ris, R., and Holthuijsen, L. (1999). A third-generation wave model for coastal regions. Part I: Model description and validation. *Journal of Geophysical Research*, 104:7649–7666.

Chen, J.-L., Hsu, T.-J., Shi, F., Raubenheimer, B., and Elgar, S. (2015). Hydrodynamic and sediment transport modeling of New River Inlet (NC) under the interaction of tides and waves. *Journal of Geophysical Research: Oceans*, 10.1002:4028–4047.

Chu, A., Wang, Z., and de Vriend, H. J. (2015). Analysis on residual coarse sediment transport in estuaries. *Estuarine, Coastal and Shelf Science*, 163(PB):194–205.

Codiga, D. L. (2011). Unified tidal analysis and prediction using the UTide Matlab functions.

Compton, T. J., Van der Meer, J., Holthuijsen, S., Dekinga, A., Horn, J., and Klunder, L. (2013). Synoptic intertidal benthic surveys across the Dutch Wadden Sea 2008 to 2011.

Cowell, P. J., Stive, M. J. F., Niedoroda, A. W., Vriend, H. J. D., Swift, D. J. P., Kaminsky, G. M., and Capobianco, M. (2003). The coastal-tract (Part 1): A conceptual approach to aggregated modeling of low-order coastal change. *Journal of Coastal Research*, 19(4):812–827.

Dronkers, J. (1986). Tidal asymmetry and estuarine morphology. *Netherlands Journal of Sea Research*, 20(2/3):117–131.

Duran-Matute, M., Gerkema, T., De Boer, G. J., Nauw, J. J., and Gräwe, U. (2014). Residual circulation and freshwater transport in the Dutch Wadden Sea: A numerical modelling study. *Ocean Science*, 10(4):611–632.

Duran-Matute, M., Gerkema, T., and Sassi, M. G. (2016). Quantifying the residual volume transport through a multiple- inlet system in response to wind forcing: The case of the western Dutch Wadden Sea. *Journal of Geophysical Research: Oceans*, 121:7431–7454.

Elgar, S., Raubenheimer, B., and Guza, R. T. (2005). Quality control of acoustic Doppler velocimeter data in the surfzone. *Measurement Science and Technology*, 16(10):1889–1893.

Elias, E. P. (2017a). Stroming en sedimenttransport langs de Boschplaat op Terschelling. *Deltares report 11200878-000*.

Elias, E. P. (2017b). Understanding the present- day morphodynamics of Ameland inlet. *Deltares report 1220339-006*.

Elias, E. P., Cleveringa, J., Buijsman, M. C., Roelvink, J. A., and Stive, M. J. (2006). Field and model data analysis of sand transport patterns in Texel Tidal inlet (the Netherlands). *Coastal Engineering*, 53(5-6):505–529.

Elias, E. P., Van Der Spek, A. J., Wang, Z. B., and De Ronde, J. (2012). Morphodynamic development and sediment budget of the Dutch Wadden Sea over the last century. *Netherlands Journal of Geosciences*, Geologie e(3):293–310.

Flinchem, E. P. and Jay, D. A. (2000). An introduction to wavelet transform tidal analysis methods. *Estuarine, Coastal and Shelf Science*, 51(2):177–200.

Friedrichs, C. T. and Aubrey, D. G. (1988). Nonlinear tidal distortion in shallow well-mixed estuaries: a synthesis. *Estuarine, Coastal and Shelf Science*, 30(6784):321–322.

Gatto, V. M., van Prooijen, B. C., and Wang, Z. B. (2017). Net sediment transport in tidal basins: quantifying the tidal barotropic mechanisms in a unified framework. *Ocean Dynamics*, 67(11):1385–1406.

Godin, G. (1983). The spectra of point measurements of currents: their features and their interpretation. *Atmosphere - Ocean*, 21(3):263–284.

Goring, D. G. and Nikora, V. I. (2002). Despiking acoustic doppler velocimeter data. *Journal of Hydraulic Engineering*, 128(1):117–126.

Gräwe, U., Burchard, H., Müller, M., and Schuttelaars, H. M. (2014). Seasonal variability in M2 and M4 tidal constituents and its implications for the coastal residual sediment transport. *Geoophysical Research Letters*, (41):5563–5570.

Gräwe, U., Flöser, G., Gerkema, T., Duran-Matute, M., Badewien, T. H., Schulz, E., and Burchard, H. (2016). A numerical model for the entire Wadden Sea: Skill assessment and analysis of hydrodynamics. *Journal of Geophysical Research: Oceans*, pages 5231–5251.

Guo, L., van der Wegen, M., Jay, D. A., Matte, P., Wang, Z. B., Roelvink, D., and He, Q. (2015). River-tide dynamics: Exploration of nonstationary and nonlinear tidal behavior in the Yangtze River estuary. *Journal of Geophysical Research: Oceans*, 120:3499–3521.

Hayes, M. O. (1979). Barrier island morphology as a function of tidal and wave regime. *Barrier Islands: From the Gulf of St. Lawerence to the Gulf of Mexico*, edited by.

Henderson, S. M., Guza, R., Elgar, S., and Herbers, T. (2006). Refraction of surface gravity waves by shear waves. *Journal of Physical Oceanography*, 36(4):629–635.

Herbers, T., Elgar, S., and Guza, R. (1999). Directional spreading of waves in the nearshore zone. *Journal of Geophysical Research*, 104(C4):7683–7693.

Israël, C. G. and Dunsbergen, D. W. (1999). Cyclic morphological development of the Ameland Inlet, the Netherlands. *Proceedings of Symposium on River, Coastal and Estuarine Morphodynamics (Genova, Italy)*, 2:705–714.

Jaffe, B. E., List, J. H., and Sallenger, A. H. (1997). Massive sediment bypassing on the lower shoreface offshore of a wide tidal inlet - Cat Island Pass, Louisiana. *Marine Geology*, 136(3-4):131–149.

Jay, D. A. and Flinchem, P. (1997). Interaction of fluctuating river flow with a barotropic tide: A demonstration of wavelet tidal analysis methods. *Journal of Geophysical Research*, 102(C3):5705–5720.

Jones, J. E. and Davies, A. M. (2008). On the modification of tides in shallow water regions by wind effects. *Journal of Geophysical Research: Oceans*, 113(5).

Kaiser, G. (2011). *A Friendly Guide to Wavelets*.

Kragtwijk, N. G., Zitman, T. J., Stive, M. J., and Wang, Z. B. (2004). Morphological response of tidal basins to human interventions. *Coastal Engineering*, 51(3):207–221.

Kreeke, J. V. D. and Robaczewska, K. (1993). Tide-induced residual transport of coarse sediment: Application to the Ems Estuary. *Netherlands Journal of Sea Research*, 31(3):209–220.

Lee, D.-Y. and Wang, H. (1985). Measurement of surface waves from subsurface gage. *Coastal Engineering 1984*, pages 271–286.

Leffler, K. E. and Jay, D. A. (2008). Enhancing tidal harmonic analysis: Robust (hybrid L1 /L2) solutions. *Continental Shelf Research*, 29:78–88.

Lesser, G. R., Roelvink, J. A., van Kester, J. A., and Stelling, G. S. (2004). Development and validation of a three-dimensional morphological model. *Coastal Engineering*, 51(8-9):883–915.

Li, C. (2013). Subtidal water flux through a multiple-inlet system: Observations before and during a cold front event and numerical experiments. *Journal of Geophysical Research: Oceans*, 118(4):1877–1892.

Makin, V. K. (2005). A note on the drag of the sea surface at hurricane winds. *Boundary-Layer Meteorology*, 115(2005):169–176.

Miner, M. D., Kulp, M. A., FitzGerald, D. M., and Georgiou, I. Y. (2009). Hurricane-associated ebb-tidal delta sediment dynamics. *Geology*, 37(9):851–854.

Mori, N., Suzuki, T., and Kakuno, S. (2007). Noise of acoustic doppler velocimeter data in bubbly flows. *Journal of Engineering Mechanics*, 133(1):122–125.

Nederhoff, C. M., Schrijvershof, R., Tonnon, P. K., and van der Werf, J. J. (2019). The Coastal Genesis II Terschelling - Ameland inlet (CGII-TA) model. *Deltares report 1220339-008*.

Nummedal, D., Penland, S., and Gerdes, R. (1980). Geologic response to hurricane impact on low-profile Gulf Coast barriers. *Gulf Coast Association of Geological Societies*.

Purkiani, K., Becherer, J., Klingbeil, K., and Burchard, H. (2016). Wind-induced variability of estuarine circulation in a tidally energetic inlet with curvature. *Journal of Geophysical Research: Oceans*, 121(5):3261–3277.

Ridderinkhof, W., De Swart, H. E., Van Der Vegt, M., Alebregtse, N. C., and Hoekstra, P. (2014). Geometry of tidal inlet systems: A key factor for the net sediment transport in tidal inlets. *Journal of Geophysical Research: Oceans*, 119(10):6988–7006.

Rijkswaterstaat (1999). *Sedimentatlas Waddenzee*.

Roelvink, J. A. (2006). Coastal morphodynamic evolution techniques. *Coastal Engineering*, 53(2-3):277–287.

Salles, P., Valle-Levinson, A., Sottolichio, A., and Senechal, N. (2015). Wind-driven modifications to the residual circulation in an ebb-tidal delta: Arcachon Lagoon, Southwestern France. *Journal of Geophysical Research: Oceans*, 120:12458–12473.

Sha, L. P. (1989). Variation in ebb-delta morphologies along the West and East Frisian Islands, The Netherlands and Germany. *Marine Geology*, 89(1-2):11–28.

Sha, L. P. and De Boer, P. L. (1991). Ebb-tidal delta deposits along the west Frisian Islands (the Netherlands): processes, facies architecture and preservation. *Clastic tidal sedimentology*, 16(1991):199–218.

Smith, N. P. (1990). Wind domination of residual transport in a coastal lagoon. *Coastal and Estuarine Studies - Residual Currents and Long-term Transport*.

Soulsby, R. L. (1997). *Dynamics of marine sands: A manual for practical applications*.

Stive, M. J. F., Capobianco, M., Wang, Z. B., Ruol, P., and Buijsman, M. C. (1998). Morphodynamics of a tidal lagoon and adjacent coast. In *8th International Biennial Conference on Physics of Estuaries and Coastal Seas, The Hague, The Netherlands*, pages 397–407.

Valle-Levinson, A., Delgado, J. A., and Atkinson, L. P. (2001). Reversing water exchange patterns at the entrance to a semiarid coastal lagoon. *Estuarine, Coastal and Shelf Science*, 53(6):825–838.

Valle-Levinson, A., Stanev, E., and Badewien, T. H. (2018). Tidal and subtidal exchange flows at an inlet of the Wadden Sea. *Estuarine, Coastal and Shelf Science*, 202:270–279.

Van de Kreeke, J. and Robaczewska, K. (1993). Tide-induced residual transport of coarse sediment; Application to the EMS estuary. *Netherlands Journal of Sea Research*, 31(3):209–220.

Van Goor, M. A., Zitman, T. J., Wang, Z. B., and Stive, M. J. F. (2003). Impact of sea-level rise on the morphological equilibrium state of tidal inlets. *Marine Geology*, 202(2003):211–227.

Van Rijn, L. C. (2007a). Unified view of sediment transport by currents and waves. I: Initiation of motion, bed roughness, and bed-load transport. *Journal of Hydraulic Engineering*, 133(6):649–667.

Van Rijn, L. C. (2007b). Unified view of sediment transport by currents and waves. III: Graded beds. *Journal of Hydraulic Engineering*, 133(7):761–775.

Vatvani, D., Zweers, N. C., Van Ormondt, M., Smale, A. J., De Vries, H., and Makin, V. K. (2012). Storm surge and wave simulations in the Gulf of Mexico using a consistent drag relation for atmospheric and storm surge models. *Natural Hazards and Earth System Science*, 12(7):2399–2410.

Walstra, D. J., Hoekstra, R., Tonnon, P. K., and Ruessink, B. G. (2013). Input reduction for long-term morphodynamic simulations in wave-dominated coastal settings. *Coastal Engineering*, 77:57–70.

Wang, Z. B., de Vriend, H., and Jeuken, M. (1999). Tidal asymmetry and residual transport in estuaries - A literature study and applications to the Western Scheldt. *WL | Delft Hydraulics report*.

Wang, Z. B., Elias, E. P. L., Van der Spek, A. J. F., and Lodder, Q. (2018). Sediment budget and morphological development of the Dutch Wadden Sea: impact of accelerated sea-level rise and subsidence until 2100. *Netherlands Journal of Geosciences*, 2018(03):183–214.

Wang, Z. B., Hoekstra, P., Burchard, H., Ridderinkhof, H., De Swart, H. E., and Stive, M. J. (2012). Morphodynamics of the Wadden Sea and its barrier island system. *Ocean and Coastal Management*, 68:39–57.

Zijl, F., Verlaan, M., and Gerritsen, H. (2013). Improved water-level forecasting for the Northwest European Shelf and North Sea through direct modelling of tide, surge and non-linear interaction. *Ocean Dynamics*, 63(7):823–847.

A
Tidal analysis at multiple locations

In Chapter 3, the tidal motion around Ameland Inlet was discussed based on several different analyses. The results from harmonic analysis and CWT analysis were prestented in that chapter for one observation point at the ebb tidal delta (Frame 1: ETD-N) and for one observation point in the tidal inlet's main channel (Frame 3: Inlet). The same analyses were done for two other observation point (i.e. Frame 4: ETD-NW2 and Frame 5: ETD-NW1). Since the results are very similar to the results for Frame 1: ETD-N, they were not presented in Chapter 3. In this appendix, the results are included for all four locations.

Table A.1 lists the characteristics of ten tidal constituents in the tidal water level variation, based on IRLS harmonic analysis. Table A.2 lists the characteristics of the same ten constituents in the depth-averaged velocity signal. One is referred to Figure 3.2 for the definition of the parameters. Figure A.1 shows the results of the CWT analysis by the continuous wavelet power spectra. For each location, the top figure relates to the water level time series and the middle and bottom figures relate to the depth-averaged velocities in east- and northward direction, respectively.

	Frame 1: ETD-N (d = 6.8 m)		
	A [m]	ϕ [°]	E [%]
M_2	0.85 ± 0.01	247 ± 1	79.4
S_2*	0.36 ± 0.01	295 ± 2	13.9
K_2	0.14 ± 0.01	51 ± 6	2.1
MU_2	0.11 ± 0.01	346 ± 7	1.2
N_2	0.10 ± 0.01	225 ± 7	1.1
O_1	0.08 ± 0.01	214 ± 9	0.8
K_1	0.07 ± 0.02	22 ± 9	0.6
M_4	0.07 ± 0.01	343 ± 11	0.5
MS_4	0.06 ± 0.01	56 ± 13	0.4
M_6	0.03 ± 0.01	101 ± 25	0.1

	Frame 3: Inlet (d = 16.3 m)		
	A [m]	ϕ [°]	E [%]
M_2	0.86 ± 0.01	256 ± 1	75.5
S_2*	0.40 ± 0.01	305 ± 2	16.6
K_2	0.19 ± 0.01	74 ± 4	3.6
MU_2	0.12 ± 0.01	352 ± 7	1.5
N_2	0.09 ± 0.01	228 ± 9	0.9
O_1	0.10 ± 0.02	218 ± 10	1.0
K_1	0.05 ± 0.01	47 ± 15	0.3
M_4	0.05 ± 0.01	346 ± 11	0.3
MS_4	0.05 ± 0.01	65 ± 11	0.3
M_6	0.03 ± 0.02	112 ± 22	0.1

	Frame 4: ETD-NW2 (d = 8.7 m)		
	A [m]	ϕ [°]	E [%]
M_2	0.87 ± 0.01	245 ± 1	79.0
S_2*	0.37 ± 0.01	293 ± 2	14.4
K_2	0.13 ± 0.01	53 ± 7	1.9
MU_2	0.11 ± 0.01	342 ± 7	1.3
N_2	0.10 ± 0.01	221 ± 10	1.0
O_1	0.09 ± 0.01	210 ± 8	0.9
K_1	0.06 ± 0.01	26 ± 13	0.4
M_4	0.07 ± 0.01	342 ± 10	0.5
MS_4	0.06 ± 0.01	53 ± 12	0.4
M_6	0.03 ± 0.01	92 ± 26	0.1

	Frame 5: ETD-NW1 (d = 6.8 m)		
	A [m]	ϕ [°]	E [%]
M_2	0.86 ± 0.01	245 ± 1	80.4
S_2*	0.35 ± 0.01	293 ± 2	13.2
K_2	0.13 ± 0.02	45 ± 7	1.7
MU_2	0.11 ± 0.01	343 ± 6	1.3
N_2	0.10 ± 0.01	221 ± 9	1.1
O_1	0.09 ± 0.01	211 ± 9	1.0
K_1	0.06 ± 0.01	23 ± 12	0.4
M_4	0.07 ± 0.02	342 ± 11	0.5
MS_4	0.06 ± 0.01	54 ± 13	0.4
M_6	0.03 ± 0.01	94 ± 25	0.1

Table A.1: Amplitude (A) and phase angle (ϕ) of ten tidal constituents in the time series of the water level at four different locations. Energy (E) is the energy percentage of the tidal constituents in the harmonic signal. The amplitudes and the phase angles are listed together with the 95% confidence interval of results. Phase angles are corrected to Greenwich time (GMT).
* based on the Rayleigh criterion, the results for S_2 are biased by energy of at least the L_2 constituent.

Frame 1: ETD-N (d = 6.8 m)					
	A_1 [m/s]	A_2 [m/s]	θ [°]	ϕ [°]	E [%]
M_2	0.61 ± 0.03	0.05 ± 0.02	150 ± 2	6 ± 3	68.0
S_2*	0.33 ± 0.03	-0.04 ± 0.02	151 ± 3	63 ± 6	20.3
K_2	0.20 ± 0.03	-0.07 ± 0.02	155 ± 9	217 ± 13	7.8
MU_2	0.1 ± 0.03	0.03 ± 0.02	154 ± 11	113 ± 20	2.0
N_2	0.08 ± 0.03	0.00 ± 0.02	147 ± 15	326 ± 25	1.1
M_6	0.05 ± 0.02	0.01 ± 0.01	175 ± 20	290 ± 54	0.4
M_4	0.03 ± 0.01	-0.01 ± 0.01	103 ± 11	65 ± 15	0.2
MS_4	0.02 ± 0.01	0.02 ± 0.01	176 ± 158	196 ± 166	0.1
K_1	0.02 ± 0.02	0.00 ± 0.01	15 ± 36	43 ± 47	0.1
O_1	0.02 ± 0.01	-0.00 ± 0.01	123 ± 36	311 ± 39	0.1

Frame 3: Inlet (d = 16.3 m)					
	A_1 [m/s]	A_2 [m/s]	θ [°]	ϕ [°]	E [%]
M_2	0.98 ± 0.04	0.03 ± 0.01	99 ± 1	12 ± 2	87.0
S_2*	0.27 ± 0.03	-0.03 ± 0.01	94 ± 2	63 ± 7	6.8
MU_2	0.16 ± 0.04	0.01 ± 0.01	101 ± 3	95 ± 12	2.4
N_2	0.15 ± 0.03	-0.00 ± 0.01	107 ± 3	354 ± 14	2.0
K_2	0.10 ± 0.03	-0.00 ± 0.01	122 ± 7	123 ± 21	1.0
M_6	0.08 ± 0.03	0.00 ± 0.00	95 ± 2	259 ± 22	0.5
K_1	0.03 ± 0.01	0.01 ± 0.00	95 ± 8	138 ± 22	0.1
O_1	0.03 ± 0.01	0.01 ± 0.00	105 ± 10	305 ± 23	0.1
MS_4	0.03 ± 0.01	0.00 ± 0.00	115 ± 5	295 ± 31	0.1
M_4	0.03 ± 0.02	-0.00 ± 0.01	124 ± 12	255 ± 38	0.1

Frame 4: ETD-NW2 (d = 8.7 m)					
	A_1 [m/s]	A_2 [m/s]	θ [°]	ϕ [°]	E [%]
M_2	0.50 ± 0.02	0.07 ± 0.01	167 ± 2	8 ± 2	73.2
S_2*	0.21 ± 0.02	-0.08 ± 0.01	179 ± 8	49 ± 12	14.8
K_2	0.14 ± 0.02	-0.05 ± 0.02	42 ± 9	339 ± 9	6.6
MU_2	0.09 ± 0.02	0.02 ± 0.01	172 ± 9	114 ± 16	2.4
N_2	0.07 ± 0.02	0.02 ± 0.02	155 ± 13	357 ± 22	1.6
M_6	0.04 ± 0.02	0.02 ± 0.01	6 ± 43	102 ± 71	0.7
O_1	0.04 ± 0.02	0.01 ± 0.01	165 ± 20	325 ± 22	0.4
K_1	0.02 ± 0.01	0.01 ± 0.01	45 ± 45	104 ± 54	0.2
MS_4	0.01 ± 0.01	-0.00 ± 0.01	157 ± 35	197 ± 29	0.1
M_4	0.01 ± 0.01	-0.00 ± 0.01	70 ± 29	191 ± 35	0.0

Frame 5: ETD-NW1 (d = 6.8 m)					
	A_1 [m/s]	A_2 [m/s]	θ [°]	ϕ [°]	E [%]
M_2	0.55 ± 0.03	0.06 ± 0.04	161 ± 4	7 ± 4	80.0
S_2*	0.19 ± 0.03	-0.04 ± 0.04	165 ± 12	48 ± 11	9.6
MU_2	0.11 ± 0.03	0.04 ± 0.03	172 ± 25	111 ± 29	3.6
K_2	0.11 ± 0.03	0.01 ± 0.03	22 ± 18	335 ± 22	2.8
N_2	0.10 ± 0.03	0.03 ± 0.03	174 ± 58	3 ± 435	2.6
M_6	0.05 ± 0.02	0.01 ± 0.01	175 ± 27	271 ± 48	0.6
O_1	0.04 ± 0.01	-0.00 ± 0.01	141 ± 21	317 ± 15	0.4
K_1	0.02 ± 0.01	0.01 ± 0.01	47 ± 47	61 ± 61	0.1
M_4	0.02 ± 0.01	-0.00 ± 0.01	178 ± 227	56 ± 211	0.1
MS_4	0.01 ± 0.01	0.01 ± 0.01	31 ± 44	29 ± 82	0.1

Table A.2: Amplitudes along the semi-major axis (A_1) and along the semi-minor axis (A_2), orientation angle of the tidal ellipse (θ), and phase angle (ϕ) of ten tidal constituents in the time series of depth-averaged velocities at four different locations. The amplitudes and the phase angle are listed together with the 95% confidence interval of results. Energy (E) is the energy percentage of the tidal constituents in the harmonic signal. Phase angles are corrected to Greenwich time (GMT). Negative amplitudes indicate clockwise rotation along the tidal ellipse.
* based on the Rayleigh criterion, the results for S_2 are biased by energy of at least the L_2 constituent.

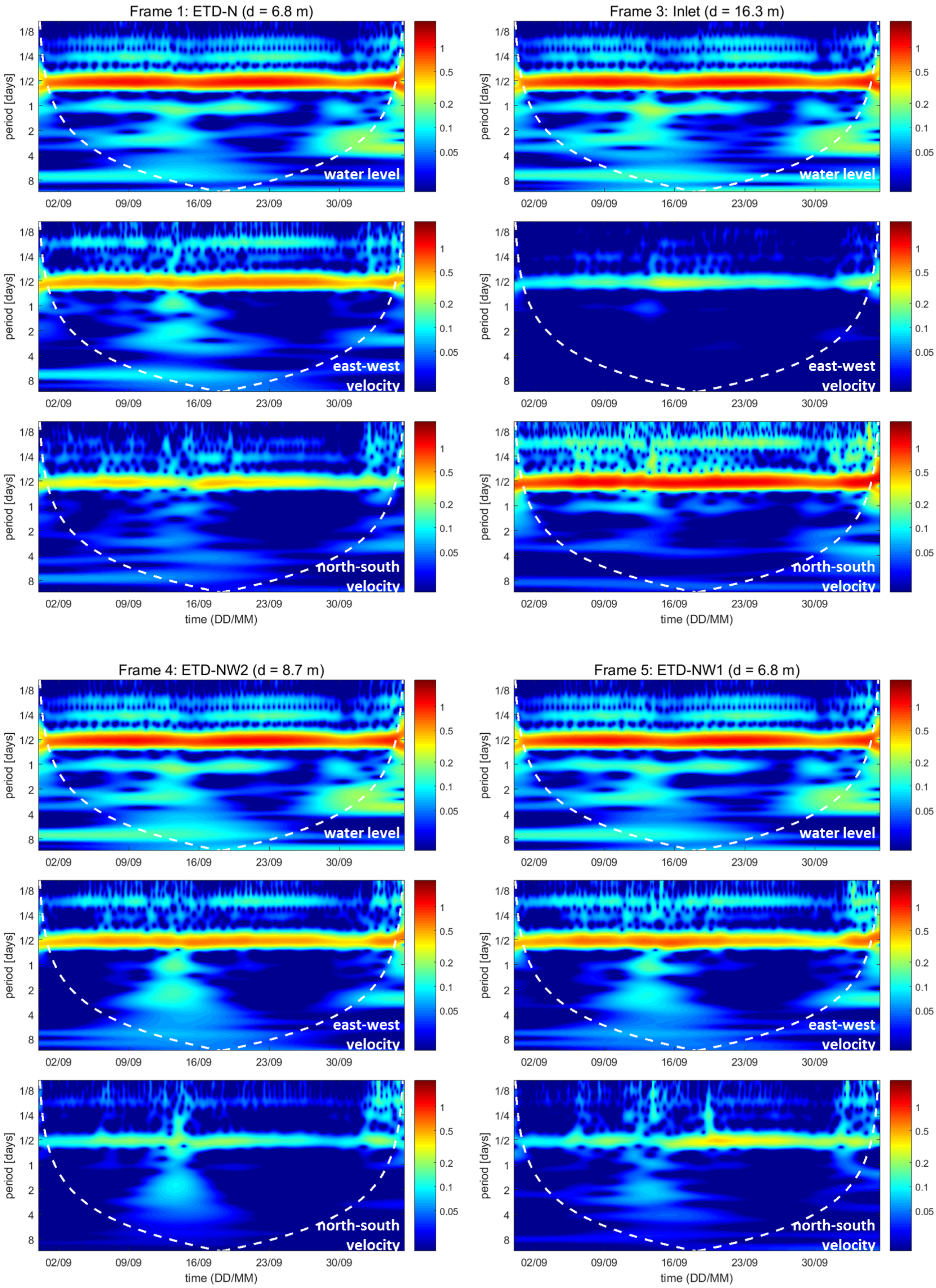

Figure A.1: Continuous wavelet power spectra of time series of the water level (top), depth-averaged east-west velocity (middle) and depth-averaged north-south velocity (bottom) at four different locations. The colour indicates the wavelet power and thereby the energy of oscillations in the record. The cone of influence is indicated by the white dashed line.

B

Sensitivity to model resolution in the inlet

In Chapter 4, the residual discharge per tidal period was discussed at four observation points, based on both field measurements and Delft3D modelling results. For observation point Frame 3: Inlet the modelling results show a residual discharge of different magnitude than observed in the field. Because it is expected that the differences between the modelling results and the field observations are partly caused by the grid resolution of the numerical model, this part elaborates on the spatial variation of residual flows in relation to the grid resolution in the inlet.

Figure B.1 shows the position of observation point Frame 3: Inlet relative to the surrounding grid cells. The observation point is located in the model domain within grid cell (260, 163), and therefore the results at this grid cell were earlier used as the modelling results for observation point Frame 3: Inlet (see Chapter 4). The results regarding the subtidal discharge for the duration of the field campaign are (again) shown in Figure B.2, both according to field observations and modelling results. The bottom depth of grid cell (260, 163) in the model bathymetry (d = 11.8 m) is lower than the bottom depth of observation point Frame 3: Inlet (d = 16.3 m). This is because the resolution of the measured bathymetry is reduced to the resolution of the model grid by taking the average of measured points in a grid cell. The difference in depth between the grid cell in the model and the observation point in the field may (partly) explain the difference in magnitude of residual flows.

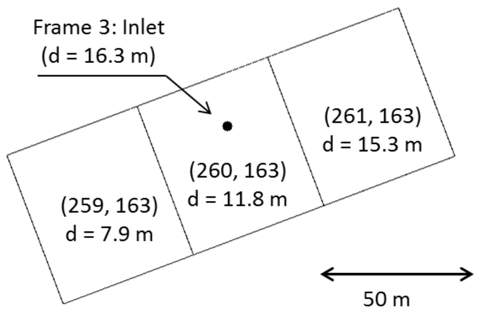

Figure B.1: Position of observation point Frame 3: Inlet relative to the surrounding grid cells in the model domain. The average water depth at the observation point is determined based on field observations, the average depth of grid cells is based on modelling results.

The results are thus evaluated at a slightly different position in the model domain than in the field. In combination with the highly varying bathymetry, this leads to a significant difference in depth and likely to a different pattern of residual flows. It is therefore difficult to judge the performance of the model based on the results presented here.

In addition, it was discussed in Chapter 6 that observation point Frame 3: Inlet was positioned at a spot in the inlet's channel where the direction and magnitude of the residual flow is much varying in space. This implies the residual flow is very different in the next grid cell (see Figure 6.5). Similar plots are therefore included for grid cells (259, 163) and (261, 163) in Figure B.3, which are the grid cells west and east of (260, 163), respectively (see Figure B.1). The difference in depth between these three grid cells indicates the transversal slope of the inlet's channel, causing the western grid cell (259, 163) to be more shallow and the eastern grid cell (261, 163) to be deeper than cell (260, 163). At the two adjacent grid cells the residual flows again show a different behaviour. At the more shallow location the direction of residual flow is more varying in time and the magnitude of residual flow is even smaller than at grid cell (260, 163). At the easternmost of the three grid cells the depth is almost as large as at the observation point in the field, but the magnitude of the residual flow is still smaller.

Although no conclusive evidence is presented here, the modelling results at the three different grid cells leave the impression that the residual discharge for the duration of the field campaign is underestimated in modelling results at this location. This would indicate that the errors in reproducing the instantaneous discharge in this part of the inlet (see Nederhoff et al., 2019) lead to an underestimation of the net residual discharge.

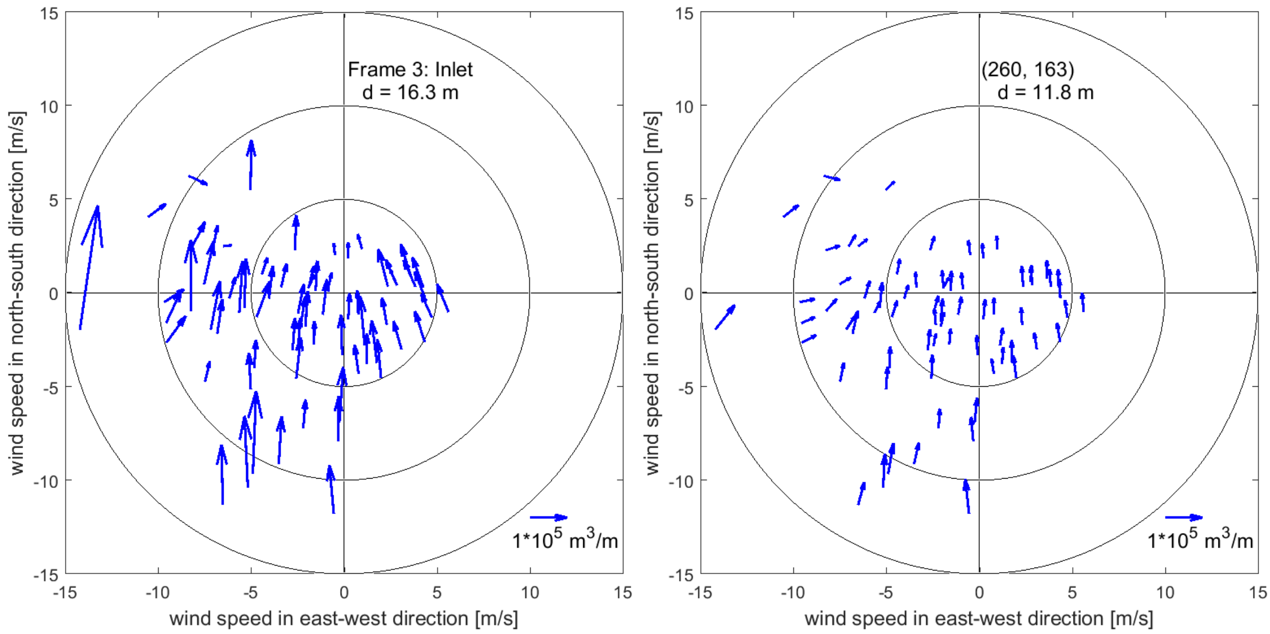

(a) Field data (b) Modelling results

Figure B.2: Residual discharge per tidal cycle during the field campaign in relation to the tide-averaged wind conditions. **(a)** is based on field observations at observation point Frame 3: Inlet and **(b)** is based on modelling results at grid cell (260, 163). See Figure B.1 for the exact positions.

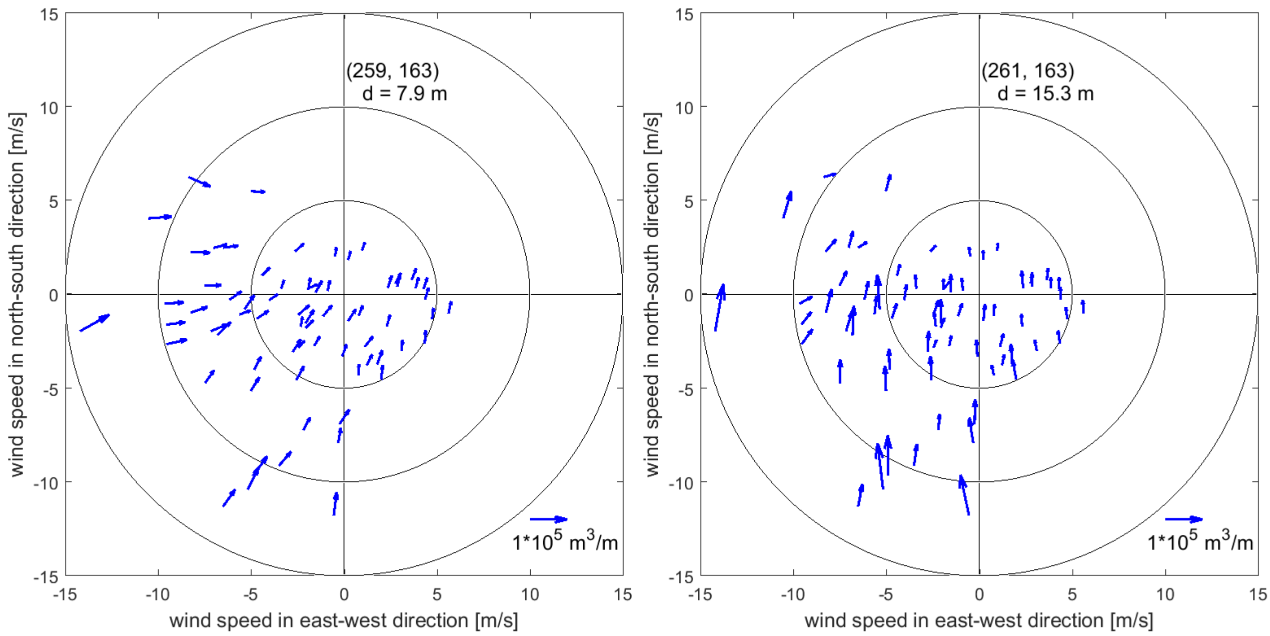

(a) Grid cell to the west (b) Grid cell to the east

Figure B.3: Residual discharge per tidal cycle during the field campaign in relation to the tide-averaged wind conditions. Both plots are based on modelling results. **(a)** is at grid cell (259, 163), which is west of the observation point. **(b)** is at grid cell (261, 163), which is east of the observation point. See Figure B.1 for the exact positions.